I.P.N. - 91406 ORSAY CEDEX

institut de physique nucléaire
CNRS - IN2P3 UNIVERSITÉ PARIS - SUD

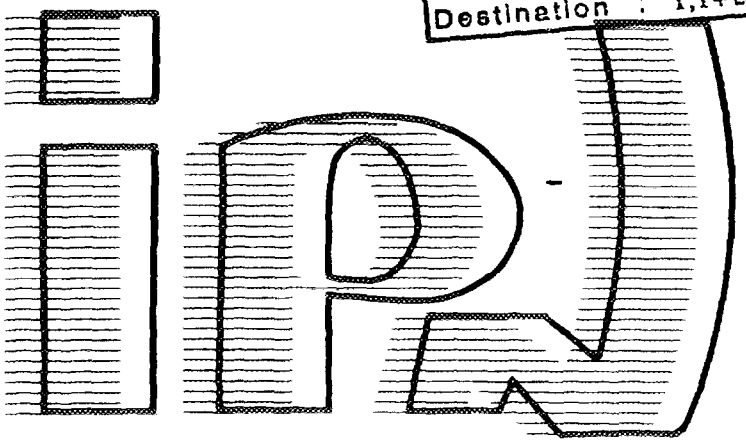

IPNO–DRE 96-08

Monte Carlo studies on Cathode Strip/Pad Chambers for the ALICE Di-Muon Arm

R. Wurzinger, Y. Le Bornec, N. Willis

DRAFT : 23/4/1996

IPNO–DRE 96-08

Monte Carlo studies on Cathode Strip/Pad Chambers for the ALICE Di-Muon Arm

R. Wurzinger, Y. Le Bornec, N. Willis

DRAFT : 23/4/1996

Monte Carlo studies on Cathode Strip/Pad Chambers for the ALICE Di-Muon Arm

R. Wurzinger [1], Y. Le Bornec, N. Willis
Institut de Physique Nucléaire, IN2P3-CNRS, F-91406 Orsay Cedex, France

DRAFT : 23/4/1996

[1]Electronic address: wurzinge@ipnosb.in2p3.fr

Abstract

A general overview about the properties of Cathode Strip and Pad Chambers is given. Position finding methods are discussed and compared within Monte Carlo studies. Noise contributions and their minimization are discussed. Pad chambers allow a two-dimensional readout with spatial resolution of $\sigma < 100\mu$m in direction parallel to the anode wire. The resolution normal to the anode wire depends mainly on the wire spacing. Special attention is paid on the double-hit resolution capability of the pad chamber. An outlook is given on the possible utilisation of Cathode Pad Chambers in the Di-Muon Arm of the ALICE detector at LHC.

Contents

Chapter 1

Introduction

The design and development of Cathode Strip Chambers (CSC) and Cathode Pad Chambers (CPC) made a lot of progress in the last few years. CSC's are usually considered as a low-cost alternative to other gas and wire chambers and can provide a good spatial resolution σ between 40 and 100 μm which is equal or better to comparative detectors. In all experiments at the Large Hadron Collider (LHC) large surface detectors with high resolution are needed. In the ATLAS and CMS [1] experiments the bunch crossing of two proton beams arrives every 25 ns, which demands a rapid response of the detector (CSC). This limits the usage of multiwire drift chambers. An advantage of CSC's is their precise construction by photo-etching, while for drift chambers the variation of drift velocities remains a problem.

The aim of this report is to review the important features of CSC and CPC described in the vast literature. Monte Carlo studies for a CPC lay-out have been performed and results are presented and discussed here in detail. Special attention has been paid if the demanded resolution of about $\sigma = 60$ μm for the Di-Muon Arm of ALICE [2] [1, 2, 3] can be achieved. As particle multiplicities in Pb–Pb collisons at LHC will be much higher as in p–p collisions (ATLAS and CMS experiments) the problem of how to resolve closely neighboured tracks (double-hits) with CPC's is treated with care.

1.1 The Di-Muon Arm in the ALICE experiment at LHC

The ALICE experiment will study in ultrarelativistic nucleus-nucleus collisions at LHC the physics of strongly interacting matter at extreme densities, where the formation of a new phase of matter, the quark-gluon plasma (QGP), is expected [3]. In 1995 it was proposed [2] to add a forward muon detector in order to measure high mass lepton pairs coming from the decays of heavy quarkonia (J/Ψ, Ψ', Υ, Υ', Υ''). The formation of these $q\bar{q}$ states should be suppressed in the presence of a deconfining medium (i.e. the QGP) [5].

The Di-Muon Arm is planned to have an acceptance between 2° and 10.5° in forward direction [3]. More than 10000 charged particles are expected in this small cone for one central Pb–Pb collision. The forward detectors have to be shielded by an absorber ($\sim$ 3.5 m thickness), designed to stop most forward hadrons without degrading the muon resolution too much and avoiding muon background from decays of stopped pions. A mass resolution of better than 1% is needed in the Υ mass region to properly separate the excited states. Muon tracks will be measured with several sets of detectors (we consider here CPC's) in a distance between 4.5 and 12 m from the collision point. The actual design consists of 8 chamber planes, grouped in sets of two planes. The latter have a distance of about 6 cm to measure the angle of the track [4]. This is necessary to speed up the fitting process in the track analysis, to minimize ambiguities and the number of *ghost tracks*. Remaining background particles (light hadrons), also coming from the beam pipe, will be stopped in a second absorber. It will be followed by 2 detector planes which serve as muon identifier. A schematic sketch of the detector is shown in fig. 1.1. A dipole or toroidal magnet will be used to measure muon momenta. More details can

[1] Compact Muon Solenoid
[2] A Large Ion Collider Experiment
[3] For a review see the article of H.R. Schmidt and J. Schukraft [4].
[4] A spatial resolution on each plane of $\sigma = 60\mu$m will give a precision of the angle between the two impact points of about 1.4 mrad.

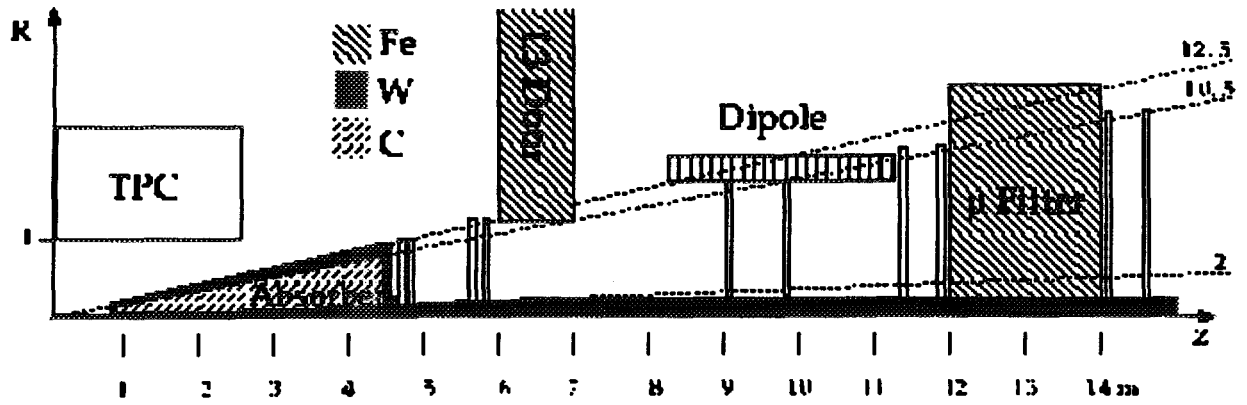

Figure 1.1: *Schematic sketch of the Di-Muon Arm of ALICE [3].*

be found in the ALICE Technical Proposal [3].

1.2 Cathode Strip and Pad Chambers

Table 1.1 gives a list of experimental results from the literature for the spatial resolution σ_x in direction along the anode wire. In the last 5 years there have repeatedly been reported resolutions well below 100 μm. However, most of these results are from detector tests under optimum conditions and usually with small chambers ($\leq 0.5\text{m}^2$).

Cathode strip/pad chambers are in fact ordinary multiwire gas chambers with segmented cathodes. The impact position is obtained by interpolating the induced charge on the cathodes over several neighbouring strips or pads. In the first design [6] the cathode consisted just of several wires which were electronically coupled. Shortly after, strips of thin copper or gold layers were applicated on thin mylar supports by photo-etching methods. Like for electronic circuits photo etching can nowadays be done industrially with high accuracy even for surfaces of several m^2 [7, 8]. Segmentation is possible in one dimension with strips or in two dimensions with pads. The latter design allows to work with high particle multiplicities and eventually (depending on the size) a position determination using the pad information also in direction normal to the anode wires. Fig. 1.2 shows two sketches of a CPC with its basic parameters. A charged particle with angle α ionizes the chamber gas along its trace. In the high voltage electric field electrons drift towards the anode wires [5]. When the electrons come closer to the anode wire, they will gain more kinetic energy due to the larger electric field. As soon as their kinetic energy is larger than the ionization energy of the gas molecules, the electrons can knock out further electrons and thus create an avalanche close to the wire. Neglecting the angular effect all the charges will in most cases be collected by one wire. Therefore the track position in direction normal to the wires (Y) is given by the wire position. The resolution in Y-direction is thus

$$\sigma_y = \frac{s}{\sqrt{12}}\,, \tag{1.1}$$

with s being the anode–anode gap.

For Monte Carlo simulations a realistic knowledge of the induced charge on the strips is of importance. There exist a number of formula and models of how to describe the charge distribution induced on the cathode which differ mainly in the tails of the distribution. Some formulae are compared in chapter 2. In the Monte Carlo simulation we will use the Gatti description [9] in its one-parameter form as given by Mathieson [10, 11]. The authors claim it to be the closest form compared with an exact calculation [9, 12, 13].

The track position is determined by interpolating

[5] Note that the positive ions of the chamber gas will drift to the cathodes but are about a factor 1000 slower than the electrons.

Table 1.1: CSC prototypes with spatial resolution $\sigma \approx 100$ μm or better. Some authors give several results from different test runs. The spatial resolution parallel to the anode wires quoted is usually the σ_x of a fit with one Gaussian to the residuals in comparison to a microstrip calibration detector, ignoring a broad *background* contribution ($\leq 10\%$) due to δ electron production, ADC overflows or double-hits. Only few *real* CPC's have been constructed. w_x is the cathode pad/strip width (readout pitch) and d is the anode-cathode spacing.

σ_x (μm)	σ_x/w_x (%)	w_x/d (mm/mm)	reference (*et al.*)	year	remarks
$\approx$60			G. Charpak [17]	1979	wire cathode
$\approx$65			F. Piuz [13]	1982	
$\approx$45		2/4=0.5	L.S. Barabash [18]	1985	
100	1.7		A.L.S. Angelis [19]	1989	CPC
<100	1.0, 2.5		R. Debbe [20, 21]	1989, 1990	CPC
64			H.v.d.Graaf [22]	1991	
80 (65)			N. Khovansky [7]	1994	
100	2.2	4.5/2=2.3	M. Benayoun [23]	1994	CPC, $w_y = 12$ mm
40–80			H. Fenker [15, 16]	1994, 1995	full size chamber
45–53			K. Lau [8]	1995	
40	0.8	5/2.5=2	G. Bencze [24]	1995	
$\approx$60			J. Guillot [25]	1995	IPN Orsay

the induced charge on neighboured strips or pads. The different interpolation algorithms are described and compared in chapter 3 and the appendix. It turns out that the algorithms used in the literature have a different sensitivity on electronic or other noise contributions. One can choose therefore an optimum method for a given chamber design.

Electronic noise, mainly of the preamplifier, is in fact the resolution determing factor. To achieve resolutions of *e.g.* 50 μm the noise amplitude variation in each pixel must not exceed 0.5% of the total cluster charge. This demands special low-noise electronics. The degradation with noise is discussed and shown in chapter 4.

The high multiplicity of events expected in the Di-Muon Arm of the ALICE detector will result in a non-negligible contribution of very close tracks with overlapping charge distributions in the chamber. Usually CSC and CPC are believed to have a very poor separation of double-tracks. The question is a stepchild of the literature. Only Fenker *et al.* [15, 16] and B. Yu [14] treat the problem to some extend. In chapter 5 methods are discussed to separate double-tracks and the resulting resolution degradation.

Finally in chapter 6 the discussed methods will be applicated on the impact distribution in a real-size pad chamber in the ALICE Di-Muon Arm. The hit distribution was generated with GEANT [6] for Pb–Pb collisions at LHC energies. As the particle density is high for small angles and low for large angles the detector does not need the same granularity over the whole surface. An outlook on the optimization of the chamber design is given.

1.3 *Standard* chamber design choosen in this model

Inspired by the good spatial resolution of $\sigma_x = 40\mu$m achieved in the test by Bencze *et al.* [24] we decided to start our simulation studies with a similar chamber design. The parameters are :

- $w_x = 5$ mm pad size in X-direction (= readout pitch)
- $w_y = 7.5$ mm pad size in Y-direction (= readout pitch)
- $d = 2.5$ mm anode-cathode gap
- $h = 5$ mm total chamber gap between 2 cathodes ($h = 2d$)
- $s = 2.5$ mm anode-anode gap

[6] The detector description and simulation tool from the CERN Program Library.

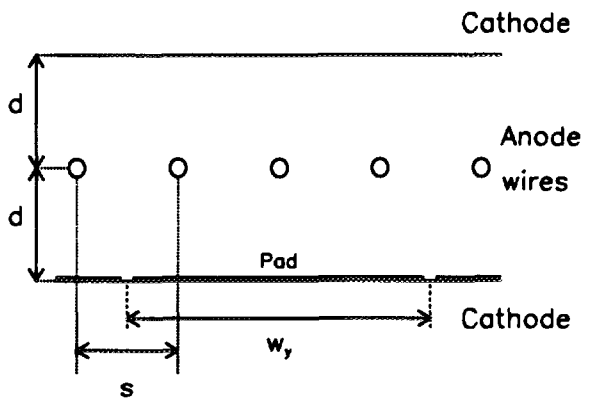

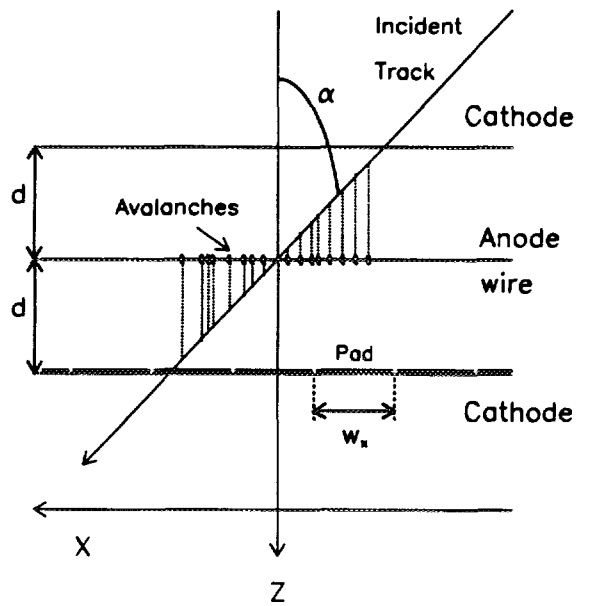

Figure 1.2: *Schematic sketch of a pad chamber. (Figures are inspired by ref. [8] and [24].) (a) Anode–cathode spacing $d = 2.5$ mm, anode wire pitch $s = 2.5$ mm, pad size in direction rectangular to the anode wires $w_y = 7.5$ mm. Only one cathode plane is segmented. (b) Chamber turned by 90° in the x-y plane. A charged particle ionizes the chamber gas along its track. Electrons will be attracted by the closest anode wire(s). Avalanches are created near the wire.*

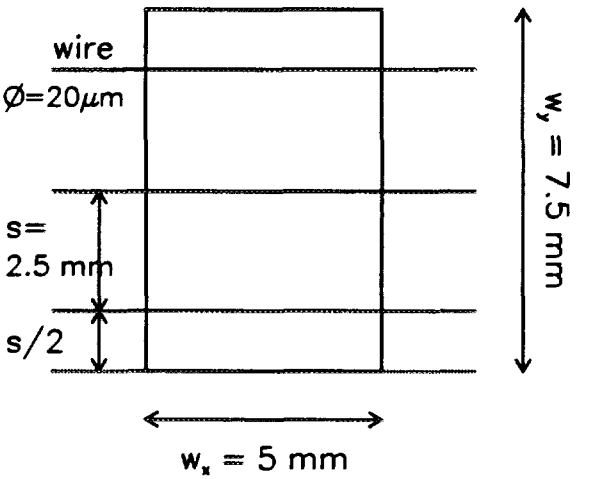

Figure 1.3: *Standard pad lay-out and definition of parameters used in the Monte Carlo simulations in this report.*

Figure 1.3 shows a sketch of the lay-out. It seems advantagous to have the wires shifted by $s/2$ from the pad edge. Like that the events attributed to each wire will have the impact on a specific pad (neglecting the angular effect). We will later refer to this lay-out as *standard design.*

Chapter 2

Charge distribution

In order to study the spatial resolution properties by means of a Monte Carlo code, it is necessary to reproduce the induced charge distribution on the cathode as precisely as possible compared to the *real* distribution. There exists a number of propositions in the literature of how to parametrize the induced charge distribution on the cathode [9, 10, 11, 26, 27, 28, 29, 30]. It has been shown that the charge distribution should be described by a formula with somewhat larger tails than a Gaussian [10, 13, 28, 30].

In the Monte Carlo simulations discussed below the induced charge on the cathode pads is calculated with the one-parameter formula given by Mathieson and Gordon [10, 11, 12] [1]. The authors claim [10] that their empirical formula is very close to the shape resulting from an exact model calculation by the same authors [12]. Their formula is now widely used in the literature (*e.g.* [13, 14, 15, 16, 31] and others) and easy to handle [2]. The Mathieson formula allows to calculate the charge distribution both in direction normal and parallel to the anode wires. Piuz *et al.* [13] found the best description of their experimental data with the Gatti/Mathieson formula. See fig. 2.1.

In the Mathieson representation the shape of the charge distribution is determined by one parameter K_3 which depends only on geometrical factors, like the anode–cathode separation, the anode wire pitch and the anode wire diameter. Values for this parameter K_3 can be found in refs. [10, 11] for a wide range of chamber geometries. K_3 is of course (weakly) dependent on geometric accuracies of the chamber con-

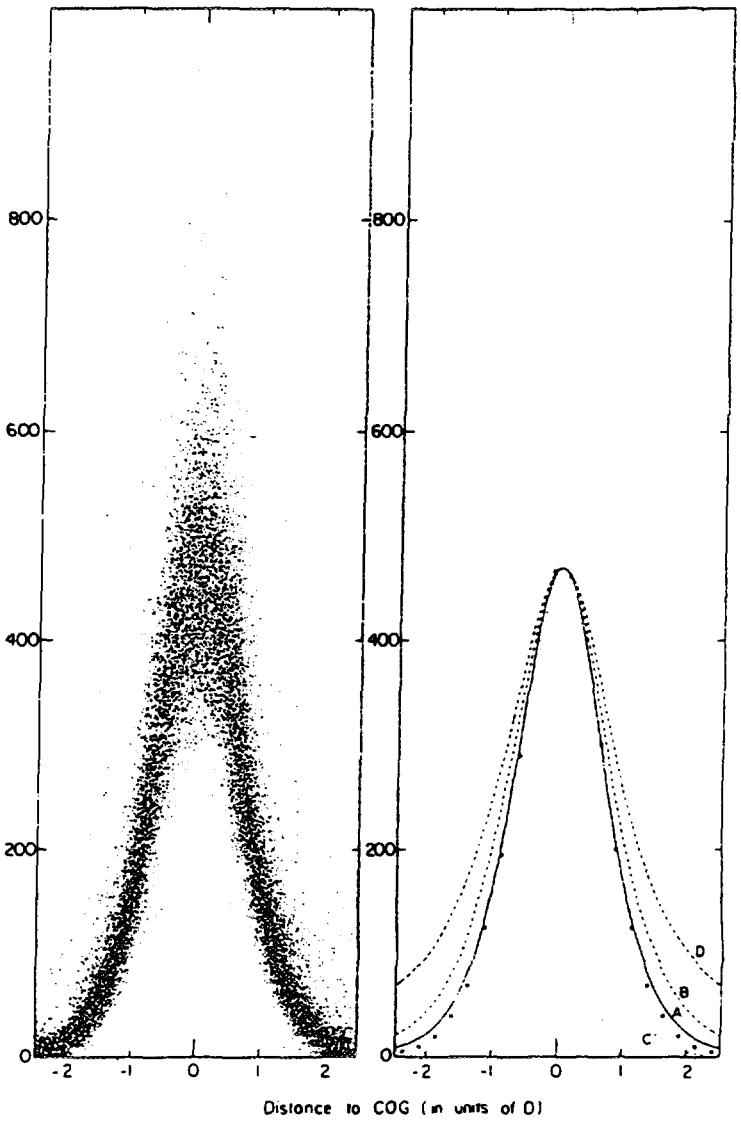

Figure 2.1: *Experimental data for the induced charge distribution compared to several formulae. (Figure from Piuz* et al. *[13].) The Mathieson charge profile (curve A) is the closest description of the experimental data. Curve B: hyperbolic secant, C: Gauss, D: Lorentz.*

[1] The formula had been derived before by Gatti *et al.* [9] and was simplified [10].

[2] Note that recently Benayoun *et al.* [29] developped a charge distribution for CPC's in both dimensions, based on the formula given by Endo *et al.* [28]. We prefer the representation of Mathieson because of its simpler form and most probably closer description of the real distribution.

struction (see section 4.1.5). Once real data are taken, K_3 can be fixed with a fit to the data to minimize systematic errors [3].

Following ref. [11] the charge distribution $\rho(\lambda)$ induced on the cathode, where $\lambda = x/d$ with x being the position either parallel or normal to the anode and d the anode–cathode separation [4] and q_a is the net anode charge, can be written

$$\frac{\rho(\lambda)}{q_a} = K_1 \frac{1 - \tanh^2(K_2\lambda)}{1 + K_3 \tanh^2(K_2\lambda)}, \qquad (2.1)$$

where

$$K_2 = \frac{\pi}{2}\left(1 - \frac{\sqrt{K_3}}{2}\right) \qquad (2.2)$$

and

$$K_1 = \frac{K_2\sqrt{K_3}}{4 \arctan\sqrt{K_3}}. \qquad (2.3)$$

Otherwise one can also write, with $1 - \tanh^2 = 1/\cosh^2$ and $\cosh^2 = 1 + \sinh^2$,

$$\frac{\rho(\lambda)}{q_a} = K_1 \frac{1}{1 + (K_3 + 1)\sinh^2(K_2\lambda)}. \qquad (2.4)$$

Values for K_3 for the charge distributions parallel and normal to the anode wire are plotted as a function of d/s and r_a in a range from 0.2 to 1.4 in ref. [11] (shown in figure 2.3) and from 1.4 to 6.0 in ref. [10]. s is the anode wire pitch and r_a the anode wire radius. All simulations in this report were done with $d/s = 1.0$ which is close to the optimum resolution (see below).

Fig. 2.2a shows the charge distributions with a Gaussian [27], Mathieson [11], hyperbolic secant squared (SECHS) [30] and Lorentzian [26] shape. The single parameter formula gives a shape between Gaussian and Lorentzian. The Lorentzian curve has very long tails and is therefore not useful. The SECHS curve is a very close approximation to the Mathieson formula. Nonsquared hyperbolic functions as used by Endo *et al.* [28] and Benayoun *et al.* [29] lie between Mathieson and Lorentzian shape. We like to stress the importance of the knowledge of the correct charge distribution, especially in its tails. As the position reconstruction algorithms work with ratios of the charges of the central to the neighbouring pads or strips, the signal-to-noise ratio of the neighbouring

[3] This was also proposed in refs. [15, 16].

[4] Note that Mathieson used the letter h for the anode–cathode gap.

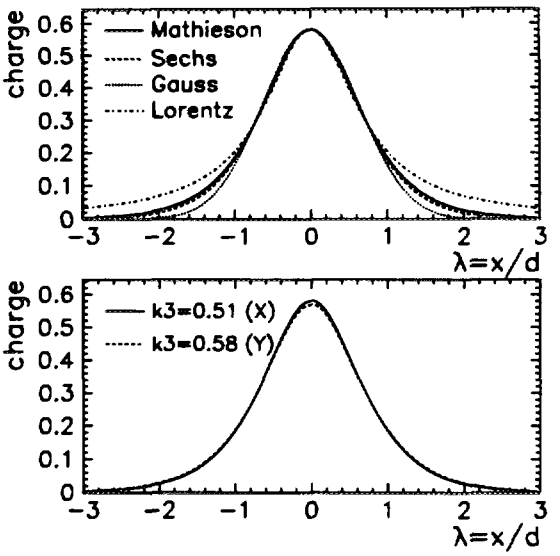

Figure 2.2: *(a) Different representations for the induced charge distribution. The curve are aligned to have the same amplitude and width. (b) Mathieson charge distribution for different values of K_3 (see text). Both figures show the charge in arbitrary units as a function of the position normalized by the anode–cathode separation.*

pads is the limiting factor. This must be correctly evaluated in the simulations. If not, the *optimized* design of the pad chamber might not be the true optimum design.

For practical reasons we note the FWHM [11] of the charge distribution in equation 2.1,

$$FWHM = \frac{4 \operatorname{arctanh}(1/\sqrt{2 + K_3})}{\pi(1 - 0.5\sqrt{K_3})}\, d. \qquad (2.5)$$

The width of the induced charge depends on the anode–cathode separation d. For the parameters chosen in this report the FWHM rests between $1.5-1.6\,d$. It is important to note that by varying d also K_3 is affected, therefore the FWHM is not only a linear function of d.

In fig. 2.2b the small K_3 dependence for charge distributions parallel or normal to the anode is shown for the chosen parameters $d/s = 1.0$ (both 2.5 mm) and $r_a = 20$ μm giving $r_a/s = 2.4 \times 10^{-3}$. The wire radius has an influence on the width of the induced charge distribution. The larger the wire radius the wider the distribution becomes (see also fig. 2.3).

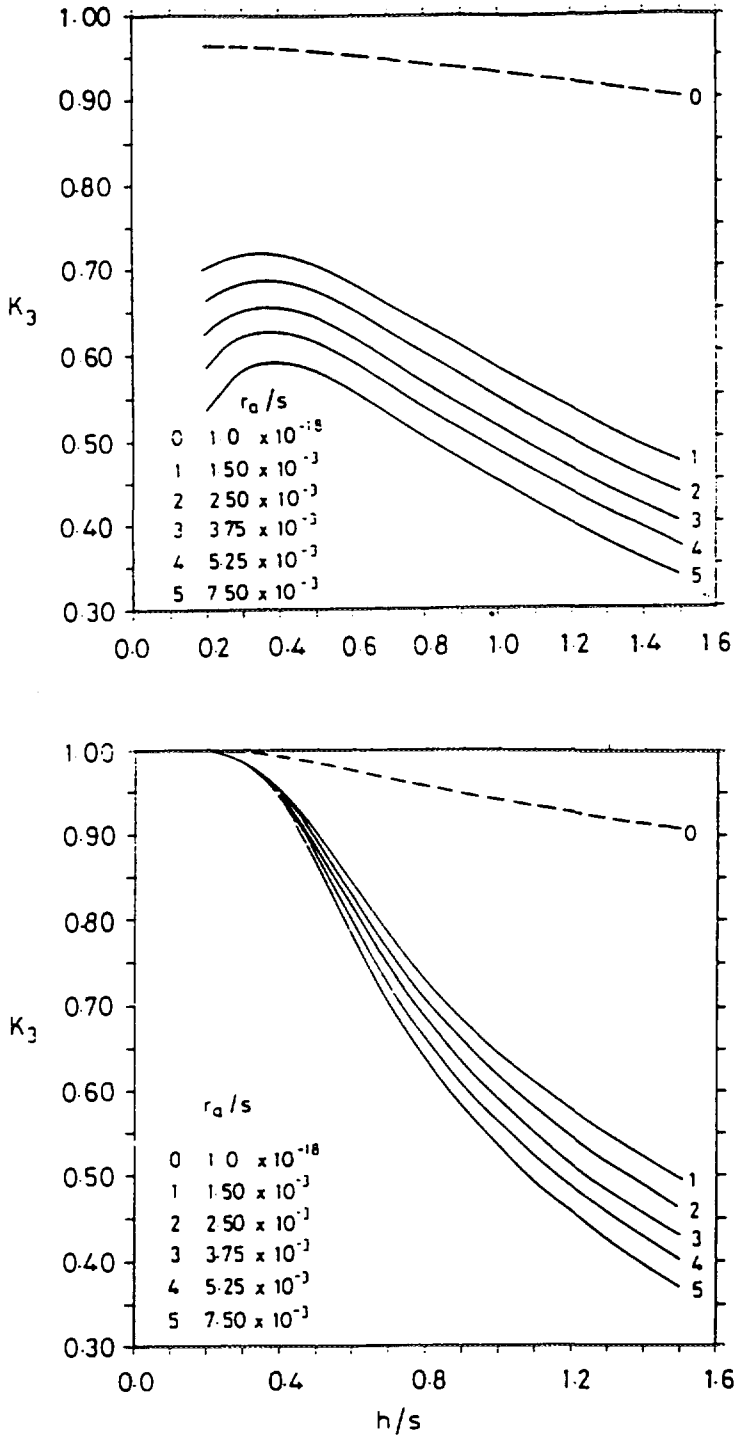

Figure 2.3: *Empirical dependence of parameter K_3 from geometrical factors as given by Mathieson [11]. h is the anode-cathode gap, s the anode-anode gap and r_a the anode wire radius. Top: Charge distribution parallel to anode wire direction (X). Bottom: Charge distribution normal to anode wire direction (Y).*

In practice we have of course to integrate the charge distribution of equation 2.1 over the strip (1–dim) or pad (2–dim) size. The 1–dimensional integral from $\lambda_1 = x_1/d$ to $\lambda_2 = x_2/d$ can be written as

$$\int_{\lambda_1}^{\lambda_2} \frac{\rho(\lambda)}{q_a} d\lambda = K_1 \int_{\lambda_1}^{\lambda_2} \frac{1 - \tanh^2(K_2\lambda)}{1 + K_3 \tanh^2(K_2\lambda)} d\lambda \ . \tag{2.6}$$

Using $z = K_2\lambda$ and substituting

$$u = \sqrt{K_3} \tanh z \ , \tag{2.7}$$

following

$$dz = \frac{du}{K_2\sqrt{K_3}(1 - \tanh^2 z)} \ , \tag{2.8}$$

one finds

$$\int_{\lambda_1}^{\lambda_2} \frac{\rho(\lambda)}{q_a} d\lambda = \frac{K_1}{K_2\sqrt{K_3}} \int_{\sqrt{K_3}\tanh(K_2\lambda_1)}^{\sqrt{K_3}\tanh(K_2\lambda_2)} \frac{du}{1+u^2} \ . \tag{2.9}$$

Defining $K_4 = K_1/(K_2\sqrt{K_3}) = 1/(4 \arctan\sqrt{K_3})$ (see eqn. 2.3) one gets finally

$$\int_{\lambda_1}^{\lambda_2} \frac{\rho(\lambda)}{q_a} d\lambda = K_4 \Big[\arctan u\Big]_{\sqrt{K_3}\tanh(K_2\lambda_1)}^{\sqrt{K_3}\tanh(K_2\lambda_2)} \ , \tag{2.10}$$

in agreement with [14].

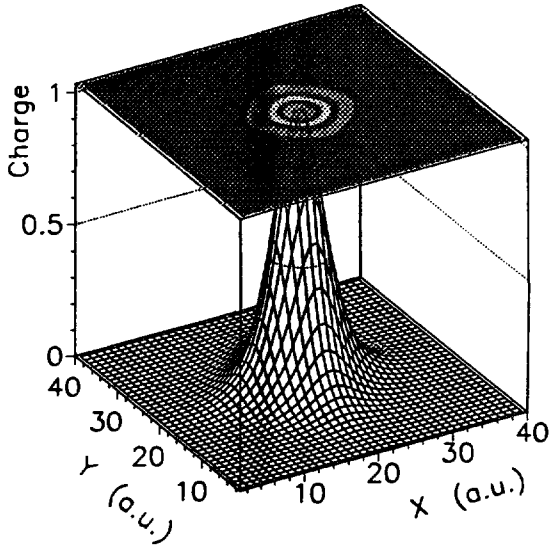

Figure 2.4: *Integral over the Mathieson charge distribution calculated with eqn. 2.10 and 2.11. In X-direction 10 arbitrary units correspond to the pad size of 5 mm and 15 units in Y-direction to 7.5 mm. The charge scale is arbitrary.*

For pads the charge distribution must also be integrated in direction normal to the anode wires. The

total integral may be written as the product of the two integrals parallel and normal to the anode wire direction:

$$\int(total) = 4 \int(\parallel) \int(\perp) \,, \qquad (2.11)$$

with 4 being the normalisation factor to unity. Only K_3 and the boundaries λ_1 and λ_2 have to be changed accordingly. Note that this simple integration is only valid for rectangular pads. The integral is plotted in fig. 2.4.

Chapter 3

Position finding methods

In this section a few commonly used position finding algorithms are discussed. They all calculate a relation between the measured charges on a few strips or pads around the impact point. For all methods systematic corrections are necessary due to the fact that the charge distribution is not linear [1]. The size of the systematic corrections is clearly depending on the chosen geometric parameters, *i.e.* the ratio of the width of the charge distribution [2] to the read-out pitch [3]. However, the reconstruction is very precise in the absense of noise, if the systematic correction is carefully treated.

There have been a number of attempts to decrease the non-linearity to improve the resolution. There are three methods:

- resistive coupling of two or more strips/pads between the read-out pitch [14, 31]
- capacitive coupling of two or more strips/pads between the read-out pitch [24]
- geometric compensation of the non-linearity *e.g.* by chevron shaped pads, zig-zag shaped strips [14, 31, 32] or other forms [33]

Finally, we point out that in general the methods using 3 pads (*i.e.* readout nodes) are the best [30, 31], because this limits the noise effects. For small ratios of pad size to anode–cathode gap one might be tended to include more pads because a considerable amount of charge is found on the side pads, but with each additional pad the noise error is increased. If the charge is spread on more pads than necessary this means that the signal-to-noise ratio is not optimized. It is therefore not adviseable to choose a chamber design where the charge is spread over more than 3 pads. This holds at least true as long as one is dealing with single hits. If the pad occupancy is high, narrower pads could have advantages in special cases.

[1] Therefore the ratio of charge induced on one pad to the total charge is not varying linearily with the impact position on the pad. Note that in the linear case the charge distribution would have a triangular shape.

[2] which depends mainly on the anode-cathode gap

[3] The read-out pitch must of course be somewhat larger than the pad size.

3.1 Some remarks about the Monte Carlo program

The Monte Carlo code provides at the state of the art a rather simplified simulation of CPC's and CSC's. So, for example, we made no attempt to simulate the electron creation in the gas and the collection at the anode, which could be done *e.g.* with the Garfield drift-chamber simulation code [4]. The pad size is at the moment identic with the readout-pitch which is of course in practice impossible. But Rybicki [34] remarks that in fact no charge can be induced on the isolator between the pads and therefore all the induced charge is shared by the pads themselves. So in the simulations the integration should be done over the readout pitch and not only over the pad width. Similar conclusions were drawn by Yu [14] to explain discrepancies of experimental data with model calculations where this effect was not taken into account. But for the basic understanding of CPC's this is not very important. Resolution comparisons with different position finding methods, the general lay-out and the double-hit problem could be studied with a simple program that has a low CPU time consumption (10000 events can be simulated in a few minutes). All calculations are done in double precision mode.

[4] Garfield by R. Veenhof, CERN Program Library W5050.

The simulations described in this section are all done without noise contribution. This allows to understand easily the systematic corrections which are necessary due to the non-linearity of the charge distribution. The quality of fits to correct for the systematic deviations can be checked instantly. The resolution degrading under the influence of noise is studied in the next chapter.

The simulation is done in the following order

- The impact position of an event is generated randomly on a selected pixel (pad) in X and Y-direction (parallel and normal to the anode wire). This can of course be easily extended to a large matrix representing a real-size chamber. The position distribution on the selected pixel is uniform. This can as well easily be replaced by a *realistic* event distribution or generated by a direct GEANT output. The latter is shown in section 6.
- There are program versions for single hits and for close double-hits. For the double-hits one can select a defined pixel distance, but each event is chosen randomly on the pixel.
- The amplitude of the total charge can be chosen to come from a Landau distribution.
- The charge integral is calculated with the Mathieson formula for each pixel in a cluster of at least (5×5) pixel size, which includes more than 99.99% of the induced charge in the standard lay-out.
- A noise signal is added randomly chosen from a Gaussian distribution. Its σ is given in the input and was usually fixed at 0.5% of the mean total charge of a standard event (see section 4.1.1).

These are the initial conditions in an experiment. Identification and position calculation is separated and has as unique information the charge measured on each pixel.

- A simple cluster (maximum) finding algorithm [5] was applied scanning through the defined chamber array.
- In experimental conditions each cluster is checked whether it can be identified as single hit or may be deconvoluted as a double-hit. (The problem of the identification and separation of double-hits is discussed in chapter 5).
- For single hits the ratio algorithm (see below) is used to calculate X and Y position of the impact. Systematic corrections are applied and the residual between calculated and real impact position are stored in a histogram.
- The position of the impact is calculated in X and Y by the center-of-gravity algorithms using between 2 and 5 pads.
- Further algoritms are tested to check the resolution which can be achieved with other methods.
- For double-hits a fit routine is applied to find the impact position of both hits in X and Y direction.

The above described routine is of course do-looped as much as is necessary to understand sytematic effects with the desired precision ($10^3 - 10^5$ events).

Once the test phase of the program is finished, a more stringent and optimized version of the program must be created to apply on to events generated with GEANT. Of course the only one (the best) position finding algorithm will be used and most spectra generated for understanding will not be necessary any longer.

3.2 Center-of-gravity algorithm

The center-of-gravity (c.o.g.) algorithm calculates a simple charge relation of 3 or more neighbouring pads or strips:

$$X_{cogr} = \frac{\sum_{i=1}^{3,4,5} X_i Q_i}{\sum_{i=1}^{3,4,5} Q_i}, \qquad (3.1)$$

where X_i is the center position of the i-th pad and Q_i the induced charge on the pad. X_{cogr} is defined in relative coordinates on the pad and can have values between $[-w_x/2, w_x/2]$. $-w_x/2$ corresponds to the left edge, 0 to the center and $+w_x/2$ to the right edge of the pad. In absolute coordinates the posistion is

$$X_{cog} = w_x X_{cogr} + X_c \qquad (3.2)$$

[5] not optimized

with X_c the center position of the hit pad.

Alternatively, Endo *et al.* [28] gave an equivalent notation to equation 3.1 which is slightly shorter to compute :

$$X_{3cogr} = \frac{-Q_l + Q_r}{Q_l + Q_c + Q_r} , \qquad (3.3)$$

with Q_{l-c-r} being the charge on the left, center or right pad. Similar notations exist using 4 and 5 pads [28].

Figure 3.1a shows the resolution achieved using the 3-c.o.g. algorithm with the standard chamber geometry. The large σ of 184 μm is not expected for a noise-free signal treatment. In 3.1b one sees the resolution as a function of the reconstructed relative position on the pad. Systematic deviations with an amplitude of 240 μm appear.

The curve of fig. 3.1b can be fitted with an odd polynom (see also [23, 29]):

$$X - X_{cog} = c_1 X_{cogr} + c_3 X_{cogr}^3 + c_3 X_{cogr}^5 + c_4 X_{cogr}^7 + \cdots , \qquad (3.4)$$

where $c_1 - c_4$ are constants found by the fit [6] and X_{cogr} is the result from eq. 3.3.

Using eqn. 3.4 to correct X_{cog} by

$$X_{cog}^{corr} = X_{cog} - (c_1 X_{cogr} + c_3 X_{cogr}^3 + c_3 X_{cogr}^5 + c_4 X_{cogr}^7) \qquad (3.5)$$

yields a much narrower distribution of the residuals $X - X_{cog}^{corr}$ shown in fig. 3.1c. Remaining systematic deviations shown in 3.1d are now negligible and could only be taken into account by correcting with a higher order polynom. Compared with the resolution degradation by noise influence the systematic effects are now very small. Taking only the first 3 terms of eq. 3.5 for the correction, like in ref. [29], would not enlarge the resolution if it is of the order of $\geq 50\mu$m.

Otherwise [8, 30] the systematic deviation can be corrected by a fourrier series

$$X - X_{cog} = \sum_m a_m \sin(\frac{2m\pi}{w_x} X) . \qquad (3.6)$$

Usually 4 to 6 terms are needed untill systematic effects are smaller than the noise contribution.

[6] As no 2-dimensional histogram-fit can be done with PAW (from Cernlib), we write X_{cogr} and $(X - X_{cog})$ into a file which can be read as two vectors by PAW. The fit can then be done in 2-dimensions with the *vector/fit* command.

For the standard lay-out with small pad length also in Y-direction the c.o.g. algorithm can also be used to reconstruct the vertical position. Taking similar to eq. 3.3 the charges of 3 consecutive strips in Y-direction (Q_{up}, Q_c and Q_{down}) one gets the Y-position as shown in fig. 3.2a. The calculated positions at 0° are of course discrete due to the fact that the induced charge origins from the wires. Taking into account systematic deviations (fig. 3.2b) similar to eq. 3.4 for the 7.5 mm pad size one gets the expected resolution σ_Y=0.72 mm (fig. 3.2c). In d and e one sees that the wire position is precisely reconstructed.

3.2.1 Using more than 3 pads

The c.o.g. method can easily be extended to include more pads. Nevertheless, this is only useful if the charge distribution is large compared to the pad size [7]. In the above given geometric example the integrated charge on 3 neighbouring strips is always > 98.5% and in most cases > 99.5%. If the mean noise amplitude variation on each pad is 0.5% of the total cluster charge, then the signal/noise ratio would be in the best case of the order of 1 on the outer strips but much worse in most of the cases. So only noise is added. Lau *et al.* [8] give an approximate relation between the number of strips used and the spatial resolution

$$\sigma = K \frac{\sigma_q}{q_{tot}} w , \qquad (3.7)$$

where σ_q is the rms error of the charge measurement per strip, q_{tot} is the total charge and w is the strip pitch. The constant K is given by $\sqrt{n-1}$ with n being the number of strips used in the c.o.g. algorithm.

3.3 Charge-Ratio algorithm

The charge-ratio or ratio algorithm was introduced by Chiba *et al.* [35] and further developped by v.d.Graaf *et al.* [22]. The ratio algorithm uses the charges of 3 adjacent strips or pads.

The ratio algorithm makes the following ansatz [22]

[7] But then one would of course enlarge the pad size because there would be no advantage for the resolution. See chapter 4.4 and refs. [14, 30].

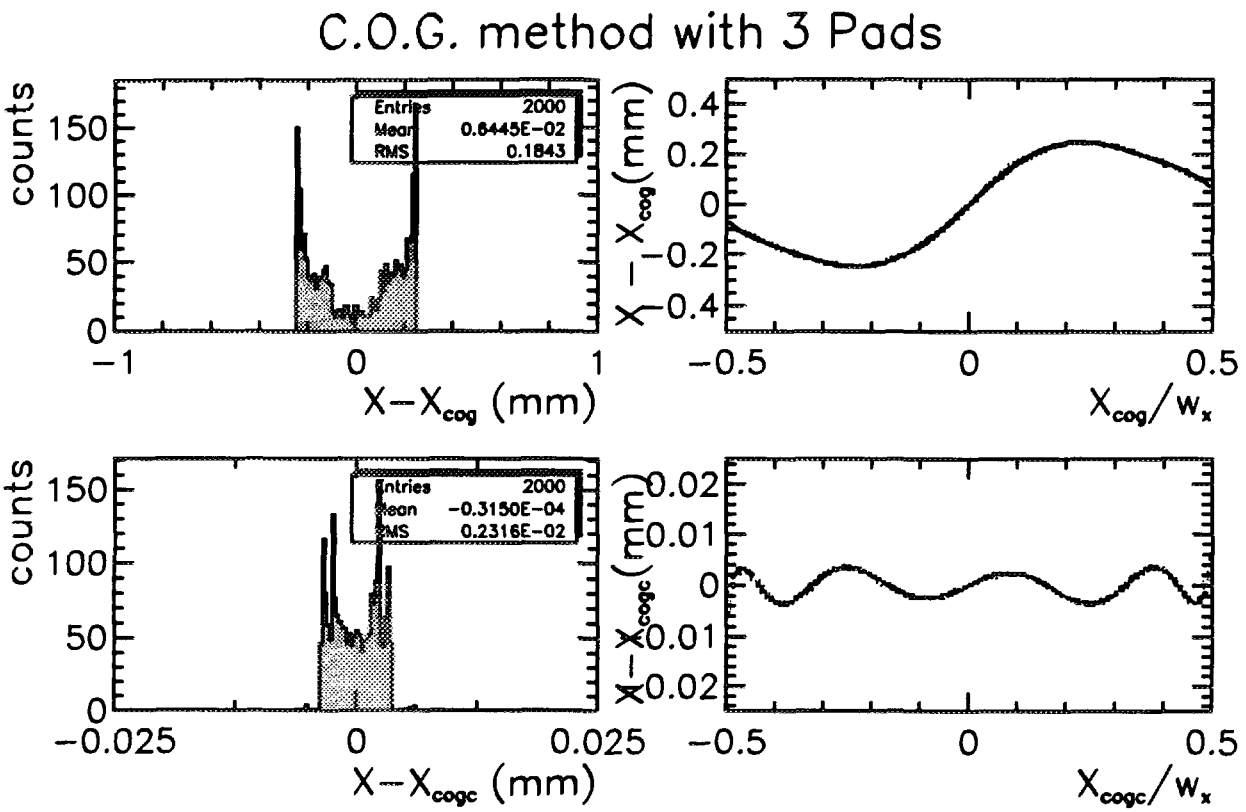

Figure 3.1: *Center of gravity method (without noise) using 3 consecutive pads. (a) gives the resolution using eq. 3.3. The σ_x for all events is about 185 μm. (b) shows the systematic deviations which attain about 240 μm near 1/4 and 3/4 of the pad. (c) After correction with the fit-polynom of 7th degree in fig. (b) the standard deviation of the residuals $\sigma_x = 2.3$ μm. (d) shows the remaining sytematic deviations.*

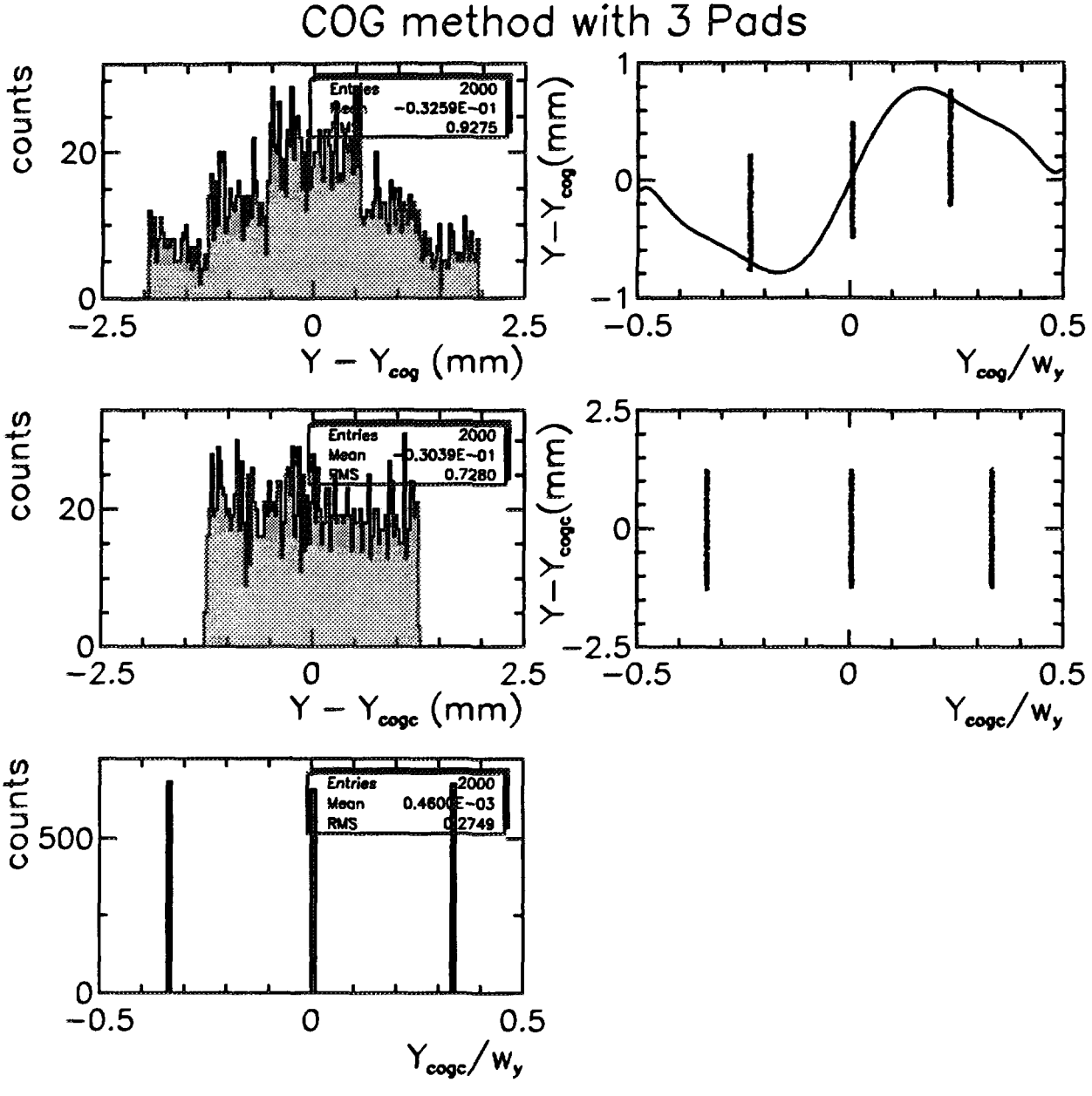

Figure 3.2: *Center of gravity method in Y-direction (without noise) for 0° using 3 consecutive pads. In (a) one sees the resolution using eq. 3.3. (b) shows the systematic deviations and its fit. (c) gives the resolution after the correction* $\sigma_y = 0.73$ *mm. (d) shows that there are no visible systematic deviations. And (e) shows the reconstructed (wire) positions.*

:

$$\alpha = \arctan\left(\frac{Q_c - Q_r}{Q_c - Q_l}\right)/\pi - 0.25\ , \qquad (3.8)$$

where Q_c is the measured charge on the center strip or pad (the charge maximum). Q_r and Q_l are the charges on the right and left pad of the center pad. The relation has a unique dependence from the position on the center pad and is plotted in fig. 3.3a from our Monte Carlo simulation data. Remark that the width of the curve comes from the bin size (100 channels). The relation is exact in the absence of noise. Van der Graaf *et al.* [22] fit the relation with $X_{rel} = c_1 \arctan(c_2\alpha))$ to reconstruct the relative position X_{rel} on the pad from the observed charges. c_1 and c_2 are constants found from the fit. They depend on the given geometric parameters [8]. We found better results by adding a linear term

$$X_{rel} = c_1 \arctan(c_2\alpha) + c_3\alpha\ . \qquad (3.9)$$

In fig. 3.3b one can see that the residuals with the true track position have a σ_X of 5.4 μm. This is due to remaining non-linearities shown in 3.3c which were not completely corrected by the fit with eq. 3.9. They could be taken into account by fitting with an odd polynom of 9th degree and the resolution would be even less than 1 μm with small remaining non-linearities (fig. 3.3d and e). But this procedure remains academic as long as noise and other effects limit the resolution to 40 or 50 μm.

For the standard chamber design the ratio algorithm can be used as well in Y-direction [9]. The results are shown in fig. 3.4. For incident tracks at 0° the induced charge origins from one of the wires meaning the the position is discrete. The curve overlayed in 3.4a was produced similar as for the data in X-direction with a pad size of 7.5 mm. It is used to calculate the position with 3.9 and the residuals are shown in fig. 3.4b. The resolution is equal to what is expected from the wire spacing $s/\sqrt{12} = 0.72$ mm. There remain no visible systematic deviations and the wire position is clearly reproduced (3.4c and d).

[8] The pad size and the width of the charge distribution.

[9] $w_y \approx 2\ FWHM$ of the charge distribution is small enough, so that in all cases at least on one of the side pads in Y-direction some charge is induced.

3.4 2-pad algorithms

The c.o.g. or ratio methods using only 2 pads might have advantages in certain cases or can be used if one of the 3 pads is absent [15, 23, 29]. We consider first the case where a side pad is missing or can not be used in the algorithm for some reason. The case where the center pad has an overflow or is absent is described below. The position is calculated as the ratio of the left or right side pad with the center pad. The error will of course be relative large if the charge on the corresponding side pad is relatively small, meaning that the impact point is more on the opposite side of the side pad. Nevertheless the error is comparative to the ratio algorithm as long as the impact is on the relative half to the side pad.

3.4.1 2-pad c.o.g. like algorithm

In this algorithm first the ratios

$$R_l = \frac{Q_l}{Q_c} \quad \text{and} \quad R_r = \frac{Q_r}{Q_c} \qquad (3.10)$$

are calculated. They are shown in fig. 3.5a as a function of the relative position of the impact on the center pad. These relations are fitted with

$$R_{l(r)} = c_1 e^{c_2 X_{rel}} + c3\ , \qquad (3.11)$$

where c_{1-3} are constants found from the fit. Note that the sign of c_2 is negative for R_l and positive for R_r. The results of the fit is superimposed. The position can now be calculated with the charge ratios using the fit. $X_{l(r)}$ is then

$$X_{l(r)} = (\ln \frac{R_{l(r)} - c_3}{c_1})/c_2\ . \qquad (3.12)$$

The resolution are shown in fig. 3.5b and remaining systematic deviations in fig. 3.5c, which are only important on the opposite side of the side pad . They can be corrected by a polynom of 3^{rd} degree but as one sees later these deviations are negligible compared with noise contributions.

The results in Y-direction are shown in fig. 3.6. The charge ratios Q_b/Q_c and Q_t/Q_c are plotted as a function of the relative impact position on the center pad in (a) and (b). The solid lines show the behaviour as if the charge was induced from continous points as

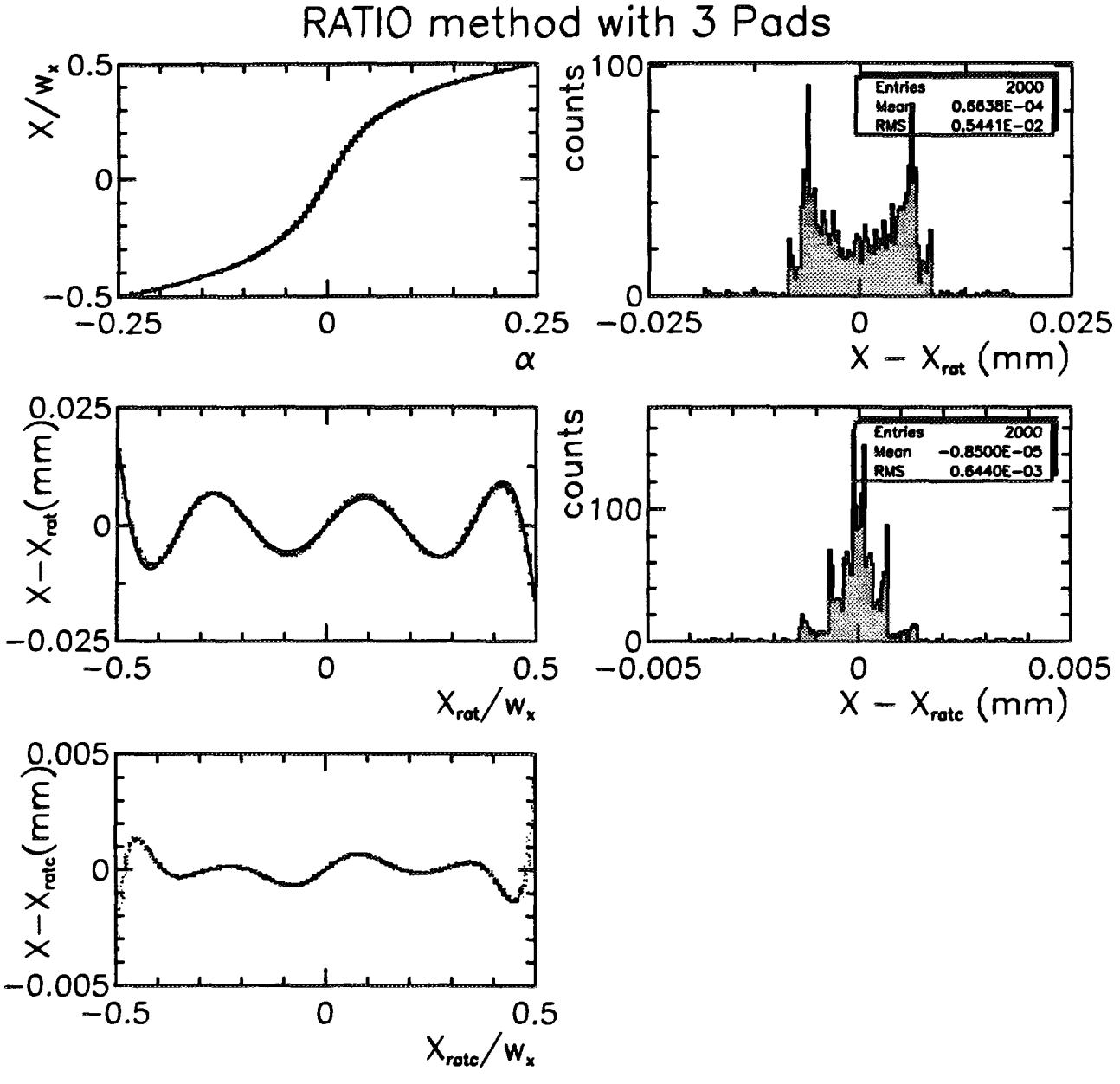

Figure 3.3: *Charge ratio method (without noise) using 3 consecutive pads. In (a) one sees the relation between the normalized position and α from eq. 3.8. The width of the curve is governed by the bin size of 100 channels. The fit drom eq. 3.8 is superimposed but there is no visible difference to the simulated data. (b) gives the resolution using the fit of eq. 3.9. The σ_x for all events is only about 5 μm. (c) shows the systematic deviations which are larger at the limits of the pad. In (d) one sees the resolution after correction with the fit polynom of 9th degree in fig. (c). (e) shows the remaining systematic deviations. In practice one is already satisfied with the result shown in (b).*

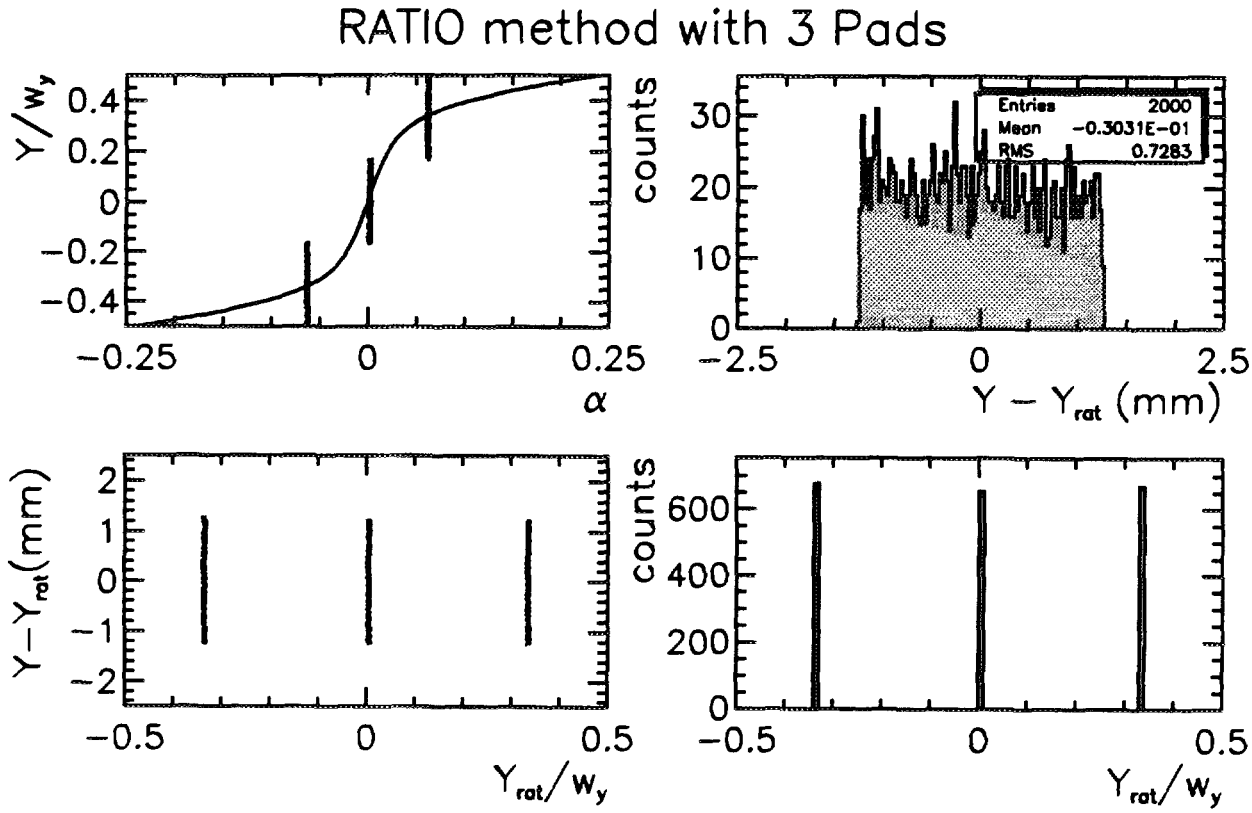

Figure 3.4: *Charge ratio method in Y-direction (without noise) for 0° using 3 consecutive pads. In (a) one sees the relation between the normalized position and α from eq. 3.8. The 3 vertical strips are the data from the 3 discrete wires. The curve shows a fit used to calculate the position. It is generated like for continuous events. (b) gives the resolution which is as expected about 0.72 mm. (c) shows the that there are no visible systematic deviations. And (d) shows the reconstructed (wire) positions.*

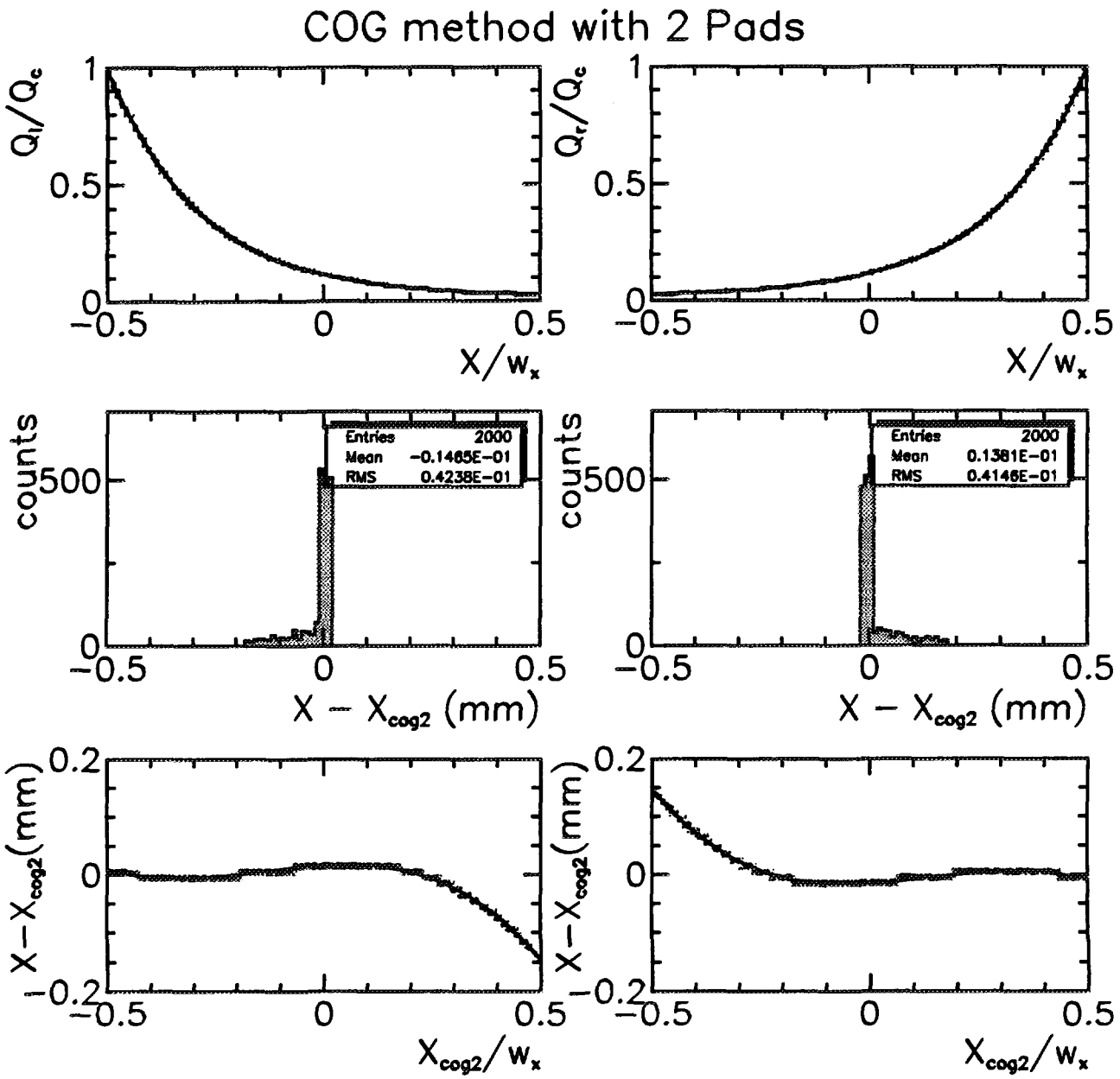

Figure 3.5: *2-pad c.o.g. algorithm without noise. (a) and (b) show the ratio of charges left (right) to the center pad as a function of the relative position on the pad. The relation is fitted to calculate X_{cog} from the charges (see text). Note that the width of the curve is dominated by the bin-size (100 channels). (c) and (d) show the residuals of the calculated position with the real position. (e) and (f) show the remaining systematic deviations and their fit (see text).*

in X-direction. But the wires cause a clear quantization (at least for 0°). For the wire on the opposite side of the pad, used to calculate the ratio, there is almost no charge induced on that pad and the ratio is close to 0. Nevertheless the position Y_{cog2} is calculated using the fit curve, as it was before done for the X-position. In the absense of noise this gives immediately a good position resolution of about $\sigma_y = 0.8$ mm (3.6c and d) which is not far from the value expected from the wire spacing of 0.72 mm. Small systematic deviations exist ((3.6e and f) and might be corrected (3.6g and h).

3.4.2 2-pad ratio-like algorithm

The 2-pad ratio-like algorithm gives very similar results to the 2-pad c.o.g. like algorithm. For completeness the formula and results are shown as well. The arctan of the charge ratios left/center and right/center (see eq. 3.10) is calculated:

$$\alpha_{l(r)} = (\arctan R_{l(r)})/\pi \; . \qquad (3.13)$$

The relative position on the pad is shown as a function of α in fig. 3.7a. They are fitted by

$$X_{l(r)} = c_1 \arctan(c_2\alpha) + c_3\alpha^2 + c_4\alpha + c_5 \; . \qquad (3.14)$$

The resolution and remaining systematic deviations are shown in fig. 3.7b. They are corrected by an odd polynom of 7^{th} degree. The result is shown in fig. 3.7c.

Results for the 2-pad ratio like algorithm in Y-direction are shown in fig. 3.8. Again one can recognize clearly the wire positions though the charge ratio for the wire opposite to the used side pad is almost 0 ((a) and (b)). With the curve shown, fitted for continous events, the position is calculated. The standard deviation of the residuals has immediately the expected size of $\sigma_y = 0.73$ mm ((c) and (d)). Systematic deviations are negligible ((e) and (f)).

3.4.3 2-pad algorithm if the center pad has an overflow

There will always be some events which induce a very large charge due to the long tail of the Landau energy loss distribution or due to the creation of δ electrons. Benayoun *et al.* [29, 23] proposed in this case just to use the ratio of charges on the side pads to determine the position on the center pad. We study to what extend this might be advantageous as compared to a normal usage of the ratio algorithm. This depends of course on the resolution which can be obtained by this left-right algorithm compared to the resolution degradation of the ratio algorithm when the overflow is not abundant. One might imagine that if the number of events which create overflows is rather small (a few %), then the usage of a special method is not helpful. This depends finally on electronics noise and the necessary amplification gain.

3.5 Remark on other methods

There exist a number of other algorithms listed by Endo *et al.* [28], Khovansky *et al.* [7] and Lau and Pyrlik *et al.* [8, 30] which mainly try to follow the shapes of the charge distribution. In the appendix formulae for

- Gaussian
- hyperbolic secant squared (SECHS)
- Mathieson
- Lorentzian

shapes are given and we show explicitly how to derrive the algorithm from the function.

It must be kept in mind that the error on the spatial resolution depends finally on the accuracy of the charge measurement. While the one or the other algorithm might be more or less sensible on the noise the resolution will still be of the same order or worse as the c.o.g. algorithm. In general the best results can be found from an algorithm which best follows the real induced charge distribution in order to limit the non-linearities. The is in agreement with the findings in the literature [7, 28, 30]. We checked the algorithms with our geometry and simulation program and the results are shown in section 4.3.

Recently Lau and Pyrlik *et al.* [8, 30] claimed to have found a new algorithm giving a better resolution. Their socalled WCOG algorithm [8] calculates

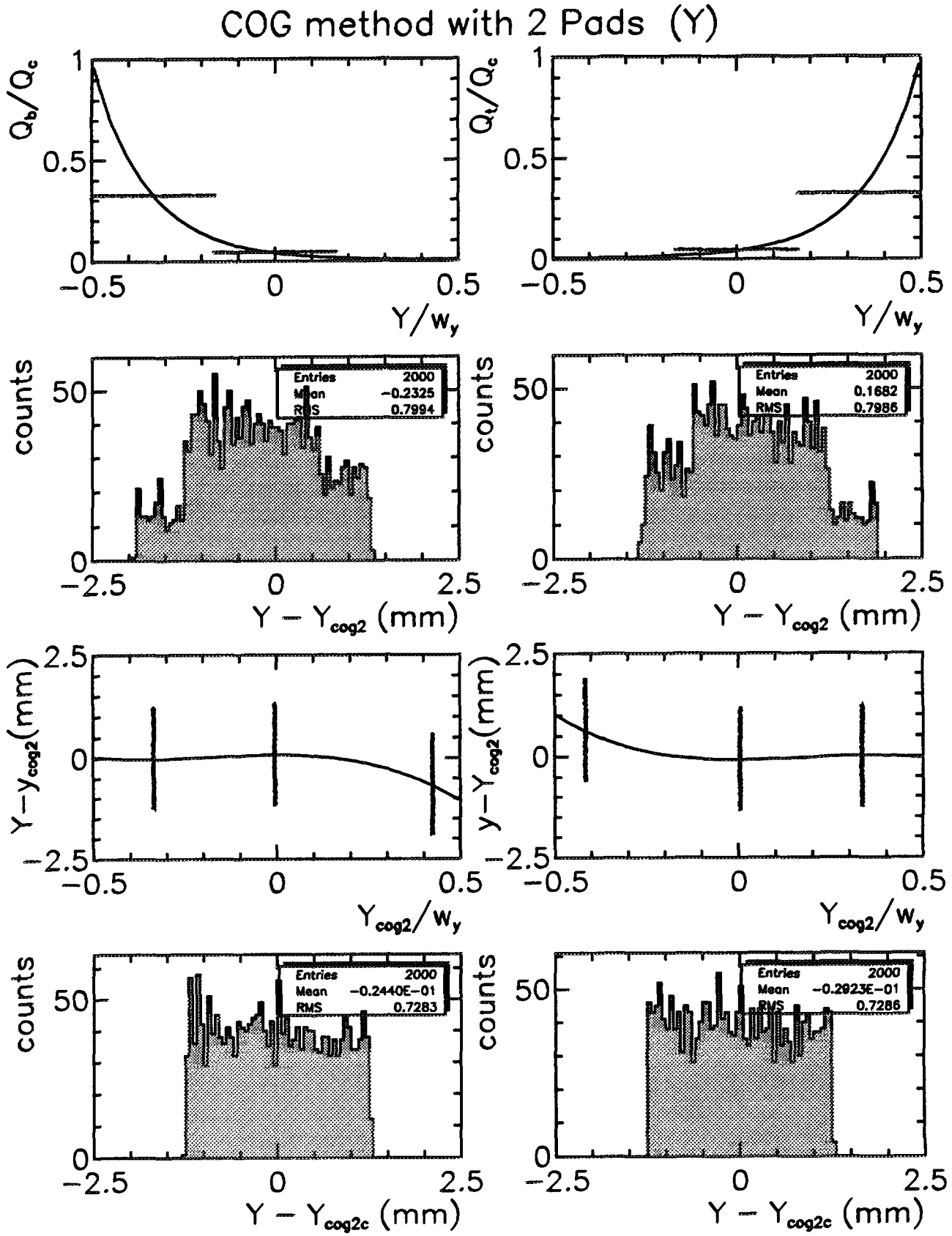

Figure 3.6: *2-pad c.o.g. algorithm in Y-direction without noise. (a) and (b) show the ratio of charges bottom (top) to the center pad as a function of the relative position on the pad. Two wires are clearly seen while the 2-pad charge ratio for the 3rd is almost 0. The curves shown were generated for continuous spectra like for the X-coordinate. The position reconstruction gives a standard deviation (in (c) and (d)) already close to the expected value ($\sigma_y = 0.72$ mm). And after correcting for systematic deviations ((e) and (f)) the reconstruction is good ((g) and (h)).*

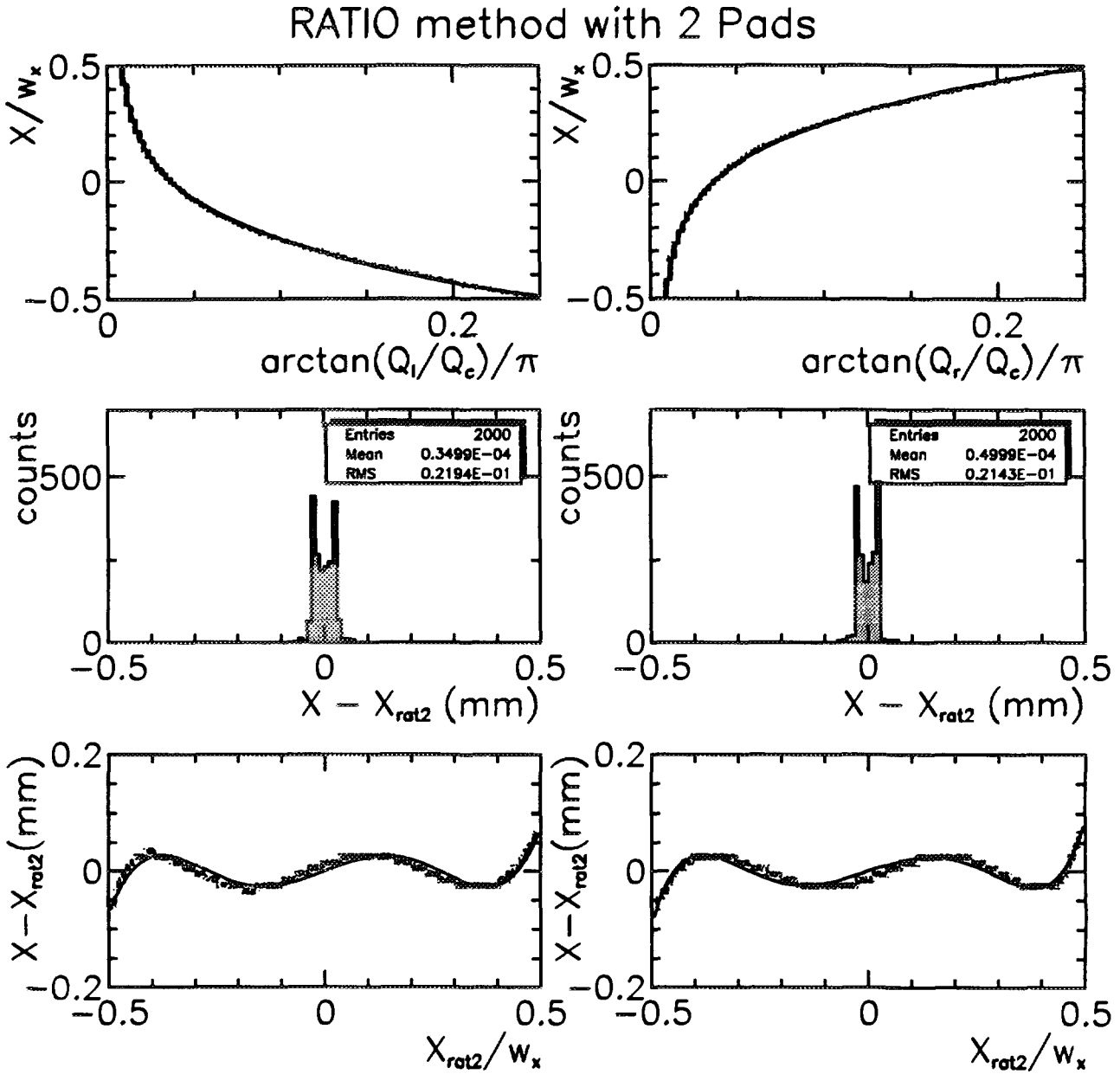

Figure 3.7: *2-pad ratio algorithm without noise. (a) and (b) show the relative position on the pad as a function of the artan of the charge ratio left (right) to the center pad. The relation is fitted to calculate X_{rat} from the charges (see text). Note that the width of the curve is dominated by the bin-size (100 channels). (c) and (d) show the residuals of the calculated position with the real position. (e) and (f) show the remaining systematic deviations and their fit (see text).*

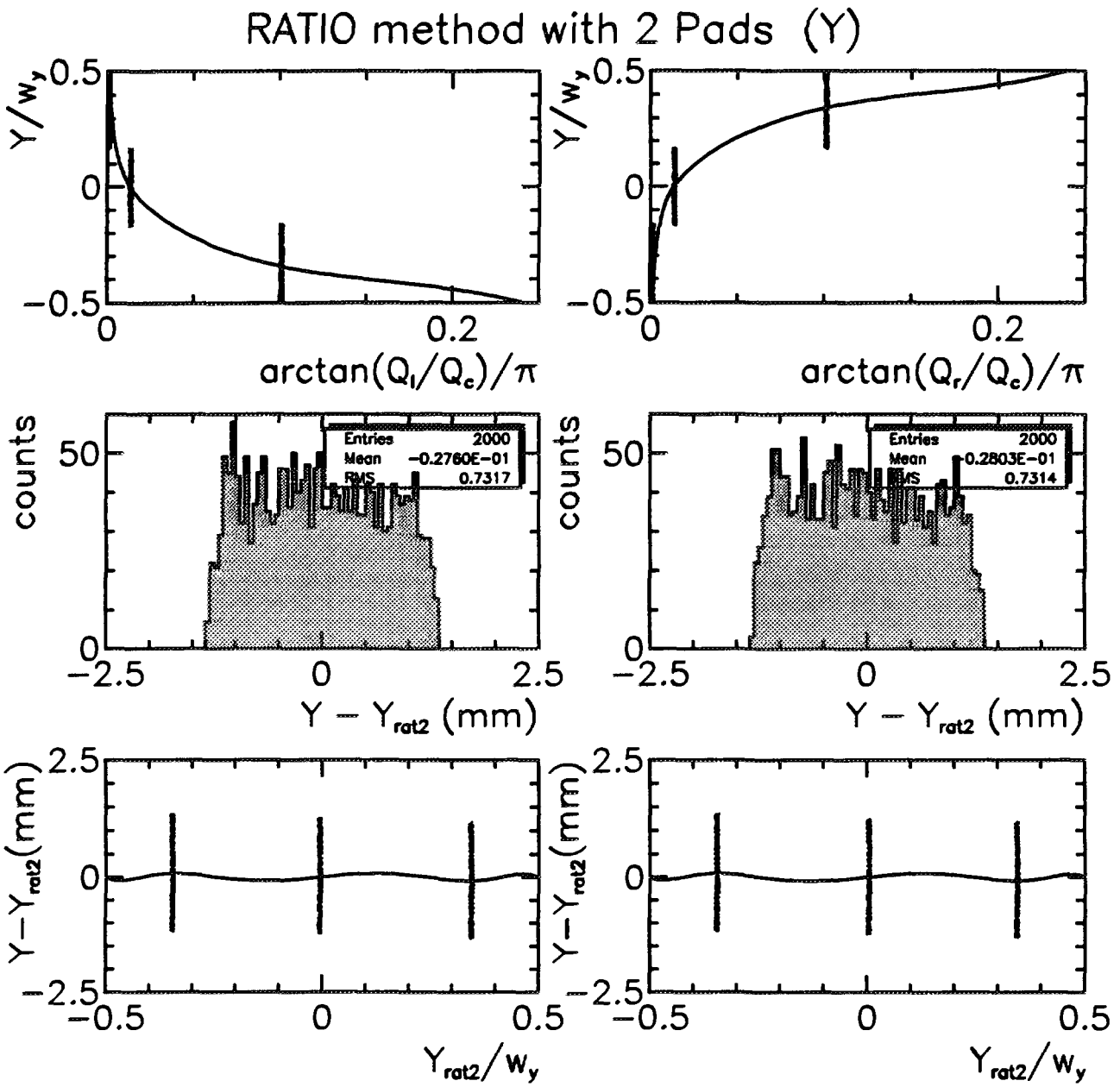

Figure 3.8: *2-pad ratio algorithm in Y-direction without noise. (a) and (b) show the relative position on the pad as a function of the* arctan *of the charge ratio bottom (top) to the center pad. Two wires are clearly seen while the 2-pad charge ratio for the 3rd is almost 0. The curves shown were generated for continuous spectra like for the X-coordinate. The position reconstruction gives immediately a standard deviation ((c) and (d)) very close to the expected value (σ_y = 0.72 mm). Correction for systematic deviations ((e) and (f)) is not necessary at this point ((g) and (h)).*

a weighted mean of the c.o.g. algorithms using 3 and 4 strips, thus prefering the region of each of the two algorithms where the non-linearities are small. But the non-linearities depend strongly on the geometry of the chamber design. The non-linearities displayed in ref. [30] correspond to a relative large value of d/w_x (similar to ref. [28]) and are very different from the behaviour in our standard design, where the non-linearities of the c.o.g. algorithms using 3 and 4 strips have a similar shape. Therefore the proposed method is not of advantage for our chamber design.

Another way of finding the impact position is the usage of a fit. This could be a simple Gauss-fit to the measured charges on 3 strips, or more refined a procedure minimizing the integrated Mathieson function over 3 strips. Unfortunately such a procedure is relative CPU time consuming. For single-hits the Gaussian can be expected to be a little worse than the ratio and c.o.g. algorithm. The 2nd procedure should provide a very similar resolution to the best algorithms. So one would conclude to use the faster algorithms. Nevertheless fits might help significantly to deconvolute nearby double-tracks. This is discussed in section 5.3.

Chapter 4

Resolution degrading contributions

4.1 Sources of resolution degradation

There are at least 8 main sources contributing to degrade the spatial resolution :

- white noise coming mainly from the preamplifier
- cross talk between neighbouring readout channels
- calibration uncertainties (offset and nonlinear gain)
- ADC digitization error of $\frac{1}{\sqrt{12}}$ channel
- mechanical tolerances in the chamber construction
- inclined tracks
- influence of strong magnetic fields (Lorentz angle)
- delta electron production

4.1.1 Electronic noise

Electronic noise can be described as white noise from the amplification system. The main contribution comes from the preamplifier. The electronic noise is usually the major resolution limiting factor and special effort has to be done to keep it on the lowest possible level. It was lately proposed to use so-called AMPLEX preamplifiers [23, 24, 36]. But new developments with on-board technique have been done *e.g.* by [33]. Some information on other electronics used can be found in the papers [7, 8, 15].

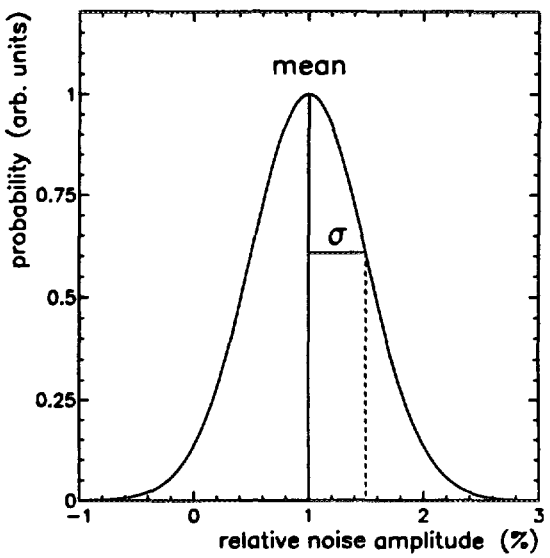

Figure 4.1: *Schematic electronic noise (Gauss) distribution. The mean noise amplitude is 1% of the mean total charge of one track. While the mean noise can be fairly well measured and subtracted from each pixel charge, the statistical fluctuation can not be accounted for. Therefore the size of σ_{noise} determines the resolution degradation and not the mean amplitude.*

We point out that for the electronic noise not the amplitude itself is important [1] but the amplitude variation. The amplitude can be measured during the calibration procedure and be subtracted by software. But there is no way to correct for statistical noise fluctuation, which is can be described by a Gaussian distribution. It is the width of this Gaussian which limits the resolution.

In the Monte Carlo simulations including noise shown in this chapter the error contribution was simulated by a Gaussian white noise. Other effects were for the time being neglected. The σ was assumed

[1] though it should still be as low as possible

to be 0.5% (see fig. 4.1) of the mean total cluster charge [2] and from this distribution noise was added on each pad. The 0.5% value is guided by the literature [16], where a *total* noise contribution from electronic noise and interchannel gain variation of this order was demanded to reach a resolution of the order of 50 μm.

4.1.2 Cross talk

The problem of cross-talk between neighbouring readout channels (pads) was discussed by several authors [13, 35]. Chiba *et al.* [35] make the following simplified ansatz. They assume a fixed percentage c of cross talk between neighbouring channels

$$Q_i' = Q_i + c(Q_{i-1} + Q_{i+1}) \,, \qquad (4.1)$$

where Q_i is the charge induced on the ith cathode strip and Q_i' the charge actually recorded by the ADC. They observed cross talk of about 3% on neighbouring strips and claim some influence on further separated strips. The cross talk is of course geometry dependent and might be minimized to some extend by leaving some space between neighbouring strips. [24] reduced to 1.5% by refining the lay-out in that manner.

It has been found that on the one hand the socalled zig-zag strip and chevron pads might be used to decrease the nonlinearity, but on the other hand by having longer borders cross talk is increased. Therefore the spatial resolution is not better as with rectangular pads and strips.

4.1.3 Calibration uncertainties

Calibration of neighbouring channels to better than 1% is necessary to achieve a resolution of the order of 50 μm [24]. Standard calibration procedures to find the electronic noise level and variations in the amplification gain are described *e.g.* by [15, 24, 35] and others and we will not repeat them here. One has in fact to check the linearity and pedestal of the complete amplification chain by a standard pulser signal. This is usually put on the preamplifier.

[2] The mean total cluster charge corresponds to the *mean* value of the Landau energy loss distribution and not to the most probable value which is much lower.

4.1.4 ADC digitization error

The digitization error of the analog-to-digital converter (ADC) is $1/\sqrt{12}$ channel. The number of channels (bits) necessary to achieve the demanded resolution has to be evaluated very carefully because it might be an important cost factor. Unfortunately the long Landau tails of the energy loss distribution makes it unavoidable to work in a large range of amplitudes if one wants not too many overflows. One has to find an optimum compromise between amplification gain (signal to noise ratio) and the losses by overflows.

In the literature the usage of 8-bit [23] and 12-bit [8, 37, 39] ADC's is reported. The latter assures a relaxed situation but is expensive. The 8-bit solution of Benayoun *et al.* [23] was optimized to have a digitization error just a little smaller than the error coming from the noise (0.85% in their case). However, a large number of overflows were registrated. But they showed that overflow events could also be treated with a comparable resolution to normal events (see section 3.4.3). The spatial resolution of single-hits in experimental tests was around 100 μm. To achieve a better resolution (provided a lower noise level) a 9-bit ADC might be sufficient.

Lately Gustafsson [33] communicated that the usage of nonlinear ADCs might reduce the number of necessary bits. Such an ADC works almost linear in the low gain range and will then have a quadratic gain dependence. Indeed, for the error on the signal the relative error Δ(signal)/signal is important and not the absolute digitization error. Therefore the situation is relaxed for large signal heights.

4.1.5 Detector mechanical tolerances

The influence of mechanical tolerances were discussed by Khovansky *et al.* [7] and by Lau *et al.* [8]. In [7] simulations for misplacements of *e.g.* anode wires were performed. This error will change the width of the charge distribution and results in a change of the systematical nonlinearities. Khovansky *et al.* conclude that a misplacement of 0.5 mm will contribute in a 35 μm resolution worsening, which means the contribution of the misplacement to the resolution is

suppressed by at least a factor of 10. These numbers are of course very geometry and algorithm dependent [30] and simulations have to be done with the chosen lay-out to define mechanical tolerances for the fabrication process.

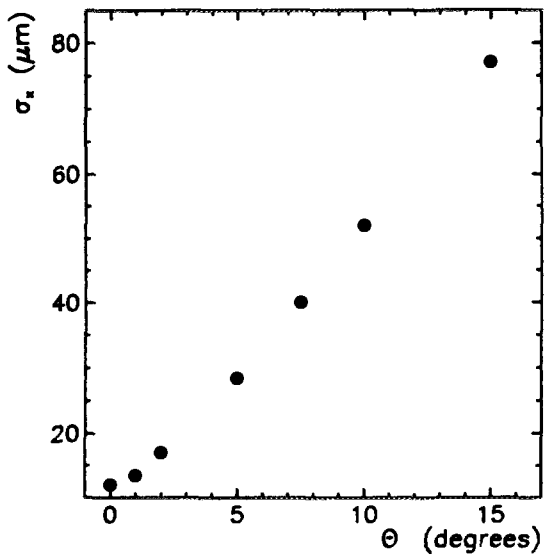

Figure 4.2: *Resolution changements by inclined tracks simulated by Brooks [39]. Dependence from θ (angle in the X–Z plane, along the wire direction). Fluctuations of the ionizations along the particle track in the gas affect the symmetry of the induced charge distribution and therefore degrade the resolution. The simulations were done without noise contribution.*

Lau *et al.* [8] find from measurements with a microscope that modern photo-etching techniques provide very precise cathode strip plane production. The expected precision of this technique is of the order of the thickness of the plated material (*e.g.* copper or gold), in their case $\sigma = 12$ μm. Similar observations were communicated by Gustafsson [33]. Vertical placements of anode wires [8] were precise to ± 0.1 mm and the wire–cathode distance error was estimated to be ± 0.2 mm. Their simulations [8, 30] showed that these uncertainties lead to a negligible spatial resolution error.

Recently Lau and Pyrlik [30] showed with Monte Carlo simulations that mechanical tolerances have different influence on the systematic nonlinearities of the position reconstruction algorithms. For vertical anode wire displacements of ± 0.5 mm they found that the ratio algorithm exhibited a large dependence, while for the SECHS and WCOG algorithms it was negligible [30]. Nevertheless the conclusions of this paper are limited to the specific chamber geometry and have to be verified for other geometries.

4.1.6 Inclined tracks

Inclined tracks will affect the chamber resolution even for small angles ($< 10°$). But there is a big difference with which plane, X–Z (θ) or Y–Z (ϕ) (see fig. ??), the angle appears. Of course one has in general a combination of both.

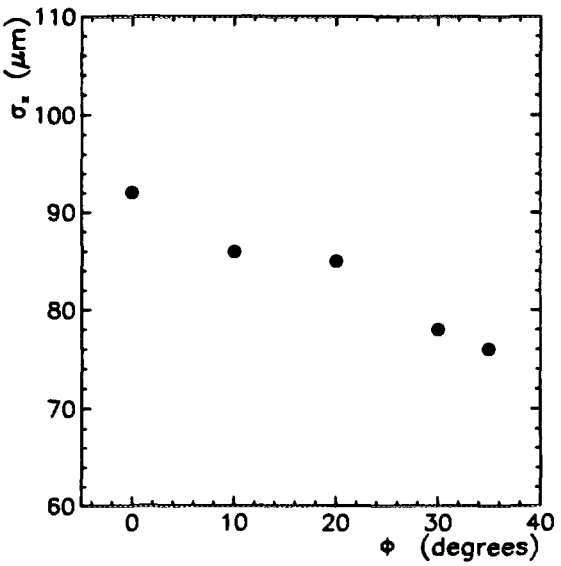

Figure 4.3: *Resolution changements by inclined tracks simulated by Brooks [39]. Dependence from ϕ (angle in the Y–Z plane). The longer trace in the gas leads to an improved signal-to-noise ratio which improves the resolution. At $\phi = 0°$ the resolution due to noise is 92 μm.*

For an angle θ of the particle track with the anode wire direction (X–Z plane) one finds a resolution degradation due to fluctuations in the inonization of the chamber gas along the track. The fluctuations will affect the symmetry of the induced charge distribution. This does not accur for 0°. Results of Monte Carlo simulations by Brooks [3] are shown in figs. 4.2 and 4.3. Remark that the figure for the θ–dependence was done without noise contribution. The fact that for 0° the resolution is already about 12 μm might be due to some uncorrected non-linearities.

[3] Note that in that reference the meanings of θ and ϕ are inversed to ours.

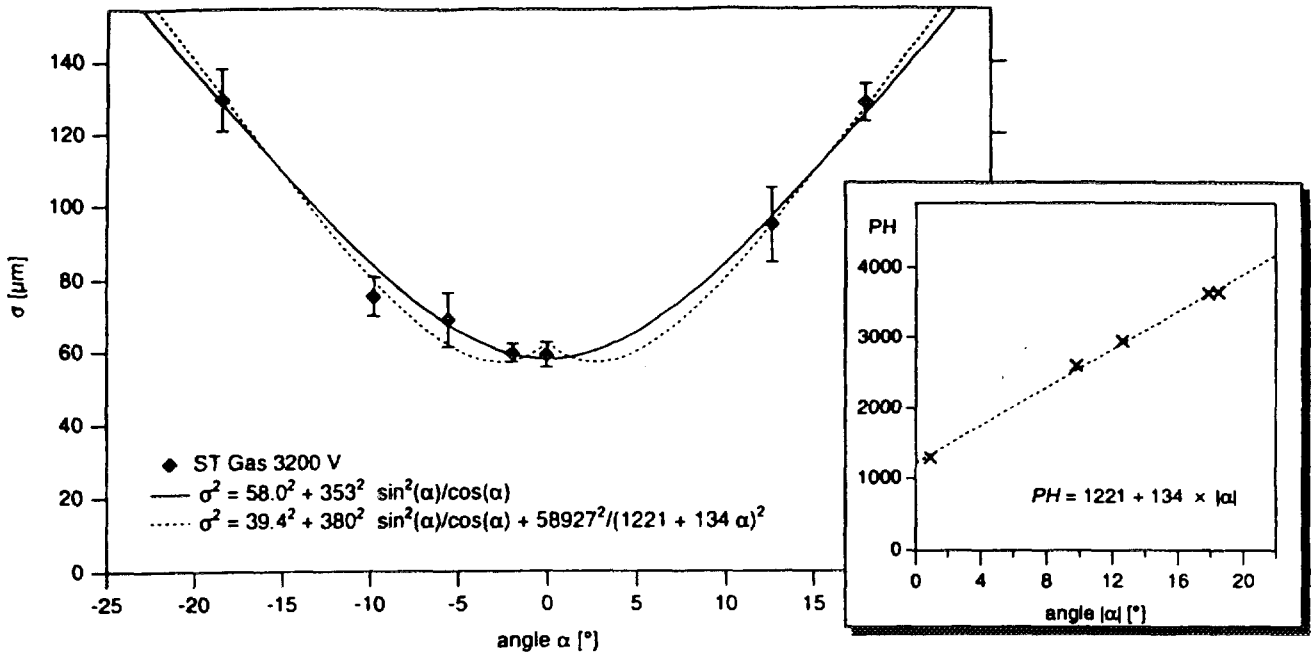

Figure 4.4: *Resolution degradation with angle measured by Lau* et al. *[8]. The solid line displays the relation of eq. 4.3. The dashed line takes in addition into account the effect that due to the angle the track in the chamber gas is longer and therefore the signal to noise ratio becomes better. The latter dependence is shown in the inset.*

The resolution degradation has to be added quadratically to the resclution with noise.

The more simple case is the angle in the Y–Z plane (ϕ). The longer trace in the chamber gas gives a larger amount of charge collected by the anode wire(s). The signal-to-noise ratio will be larger and this gives a better resolution (fig. ??). In addition, the ionization charges might be collected by 2 (or even more) wires. With a total chamber gap of $h = 5$ mm this is already a non-negligible effect compared to the wire–wire distance $s = 2.5$ mm, even for track inclinations of only $\phi = 10°$:

$$\frac{h \sin 10°}{s} = 0.35 \,. \qquad (4.2)$$

This means at 10° about 1/3 of the tracks will split their charges between 2 wires. This effect was used by Breskin *et al.* [38] in a chamber with strips in X- and in Y-direction to achieve a better resolution in Y-direction [4].

The worsening of the resolution of tracks inclined relative to the chamber plane was experimentally studied by several groups [7, 8, 17, 18, 22, 24, 30]. Lau *et al.* [8] fit their data with

$$\sigma_{tot} = \sqrt{\sigma_0^2 + \sigma_\alpha^2} \,, \qquad (4.3)$$

where σ_0 is the resolution for perpendicular tracks, α the inclination angle and σ_α is given by

$$\sigma_\alpha = b \frac{\sin \alpha}{\sqrt{\cos \alpha}} \,, \qquad (4.4)$$

with b determined by a fit. They found with $\sigma_0 = 58\mu$m $b = 353\mu$m, with the remark that b might be somewhat geometry dependent. The relation and experimental data are plotted in fig. 4.4). Their value for $\alpha \pm 10°$ is about 85 μm, which corresponds to a worsening of 27 μm which is 47%. Khovansky *et al.* [7] give a b value very close to this with the same chamber geometry, but older references [17, 18, 22] found b 2–3 times higher.

Following the argument that this resolution degradation comes from the fluctuations in the ionization process, one can assume that the b value depends strongly on the total gap of the chamber, which was in the case of references [8, 7] $h = 9$mm. For our chamber we take $h = 5$mm which should limit the effect. In addition Lau *et al.* [8] claim that the worsening of the resolution will be compensated to some extend for small angles ($< 10°$) by the larger pulse height due to a longer track in the chamber gas (dotted line in fig. 4.4). Unfortunately their data were not precise enough to proove this compensation [8]. We assume that the resolution worsening for our chamber design will be not more than 25% at 10°. This would

[4] The improvement was about 30% from what was expected by the wire spacing.

give $b = 214\mu$m with $\sigma_0 = 50\mu$m.

Recently Lau and Pyrlik [30] showed with Monte Carlo simulations that the angular effect has a different influence on the systematic nonlinearities of the position reconstruction algorithms. The angular dependent error was approximated by

$$\sigma_\Theta = \frac{h \tan\Theta}{\sqrt{12N}}\sigma_0 \,, \qquad (4.5)$$

where h is the total chamber gap, Θ the angle with the chamber plane parallel to the anode wires, σ_0 the resolution for 0° and N the number of primary clusters or *cells* which were touched. Among the algorithms giving a good resolution, especially the ratio algorithm exhibited a larger angular dependence than SECHS and WCOG algorithms [30]. But for angles $< 5°$ the effect is almost negligible.

4.1.7 Influence of magnetic fields

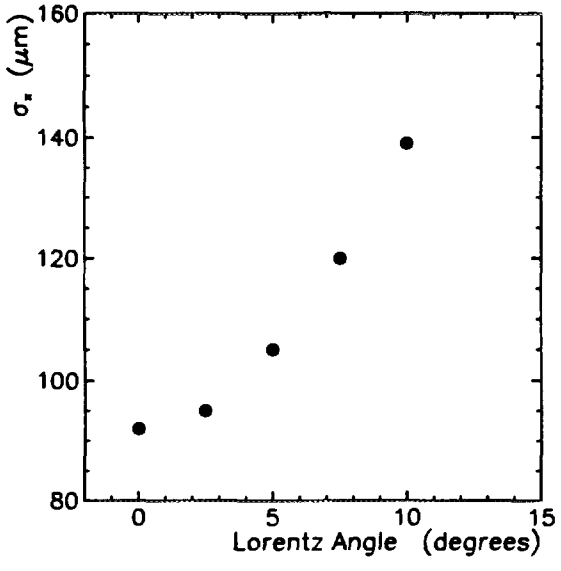

Figure 4.5: *Resolution degradation with Lorentz angle simulated by Brooks [39]. The chamber resolution is 92 μm including noise. Radial fields of 0.3 T let expect a Lorentz angle of about 3°.*

Strong magnetic fields can degrade the spatial resolution of a MWPC due to effect on the electrons created in the chamber gas. In the field the electrons will follow a curved path on their way to the anode. Results of simulations by Brooks [39] for the PHENIX CSC's are shown in fig. 4.5. For a radial field the electrons are deflected in the X–Z plane. The Lorentz angle in their case is about 3° for 0.3 T and 8° for 0.8 T. Having a resolution of 92 μm at 0° one can see that the resolution degradation for small Lorentz angles ($< 5°$) is almost negligible (less than 10%).

4.1.8 Delta electrons

The effects of δ-electron production and the influence on the spatial resolution is rarely treated in the literature and remains a problem. It is clear that in order to minimize the problem one has to put as less material as possible in the way of the charged particle. CSC's can be manufactured on a thin mylar or kapton support and are therefore a relative good solution.

As already mentioned above, experimental resolutions given in the literature for CSC's are usually derived from a Gaussian fit to the residuals between the measured position and a reference, like a micro-strip detector with a known resolution of the same order or better than the CSC. These fits always neglect a number of events far outside 3σ of the Gaussian. As the source of the large error is not clear these events are usually attributed to δ electron production. This *background* is also not always on the same level [5]. For example, in [8, 15] a rather high *background* was found, while in [7, 16] it appeared to be relatively low.

4.2 Setting of thresholds to reduce noise effects

The setting of thresholds to reduce noise contributions or effects is a very delicate problem. First of all we repeat that it is impossible to eliminate the noise contribution. Nevertheless to some extend the resolution error due to noise might be minimized by subtracting from the measured charges on each pad exactly the *average* noise on this pad. The variation in the average noise amplitude itself can of course not be subtracted, because it is a statistical effect which is usually treated as white noise with a Gaussian distribution. We discuss in this section only electronic noise neglecting cross-talk effects. We will show in

[5] This effect might come from different sources, like double-hits etc.

the following the influence of a noise *correction.*

4.3 Resolution with noise contribution

In this section the spatial resolution of different algorithms is compared. First we show in detail how one obtains results or the charge ratio and c.o.g. algorithm. Their resolutions will be compared with other algorithms which describe a shape of a function (*e.g. Gauss or hyperbolic*). Then the limits of the usage of 2-pad algorithms is demonstrated. But as we will see later they will have a role to resolve double-hits. Finally some specific features important for the resolution optimization will be discussed.

4.3.1 Charge ratio and c.o.g. algorithm using 3 pads

The results with noise for the ratio algorithm in Y-direction are shown in fig. 4.7. The resolution is not much worse as it was without noise due to the already large effect of the wire spacing. The wire position can still be reconstructed perfectly though some widening is obvious especially for the middle wire. This will be discussed below.

The charge ratio and c.o.g. methods were explained in detail in chapter 3. All simulations were done with 0.5% noise in reference to the mean total charge. The latter were chosen from a Landau energy loss distribution.

In fig. 4.6 are shown the results for the ratio algorithm for 3 consecutive pads in X-direction. α is obtained by eq. 3.8 and the position calculated with eq. 3.9. The resolution is about 48 μm. Taking into account further corrections of systematic deviations does not improve the resolution. The noise is dominating. Nevertheless it should be mentioned that these systematic deviations were only remarked by doing the simulation without noise. When looking at experimental data such a correction can not be derived.

For the c.o.g. method with 3 pads we show results in fig. 4.8. The resolution without systematic corrections is only 10 μm worse than it was without noise (fig. 3.1). But the amplitude of the systematic deviations is now larger with noise. This can be seen in fig. 4.8b by comparing with the fit which is now clearly visible. The resolution after systematic correction is 59 μm (4.8c), which is 10 μm (20%) larger than the charge ratio method.

In Y-direction the result for the c.o.g. is the same as for the charge ratio algorithm. While without systematic correction σ_y is about 936 μm (fig. 4.9), it decreases to 737 μm after corrections.

In figs. 4.10 and ?? the obtained resolution with different position finding algorithms are compared. All the resolutions σ_x are now determined by a fit to the residuals with 2 Gaussians. The mean resolution is given by the weighted mean of the σ's of the Gaussians. This method obtains more precise and reliable values than a single Gaussian fit. This is necessary because the data samples have intrinsic changes of the resolution. This will be shown in the next section. The fit with 2 or 3 Gaussians is more explained in the appendix A.5.

The resolution with the charge ratio algorithm is shown In fig. 4.10a . The weighted mean gives 43 μm which is somewhat smaller than the rms value calculated by PAW. This is due to a few events which are far outside 3σ and which increase the rms value. Below, in the same figure are the resolutions for the c.o.g. algorithms with 3, 4 and 5 pads. For 3 pads we find $\sigma_x = 56$ μm, being 13 μm or 30% larger than for the charge ratio method. Using more strips increases the signal-to-noise ratio and the resolution suffers correspondingly. Note that for the unsymmetric c.o.g.'s with 4 pads the resolution curve is also unsymmetric.

For the Gaussian *algorithm* we find $\sigma_x = 64$ μm (fig. ??) which is already 20 μm worse than the charge ratio method. In ??b and c the results of a Gaussian *fit* is shown. The first is a free fit only giving a lower limit for σ_g [6]. The second plot is the Gauss-fit result after fixing σ and the gain from the first fit and keeping only the position as parameter. The improvement is unfortunately small. The result is 10 μm above the charge ratio algorithm. The last

[6] It is interesting to note that by giving a convenient lower limit for σ_g systematic deviation could be minimized.

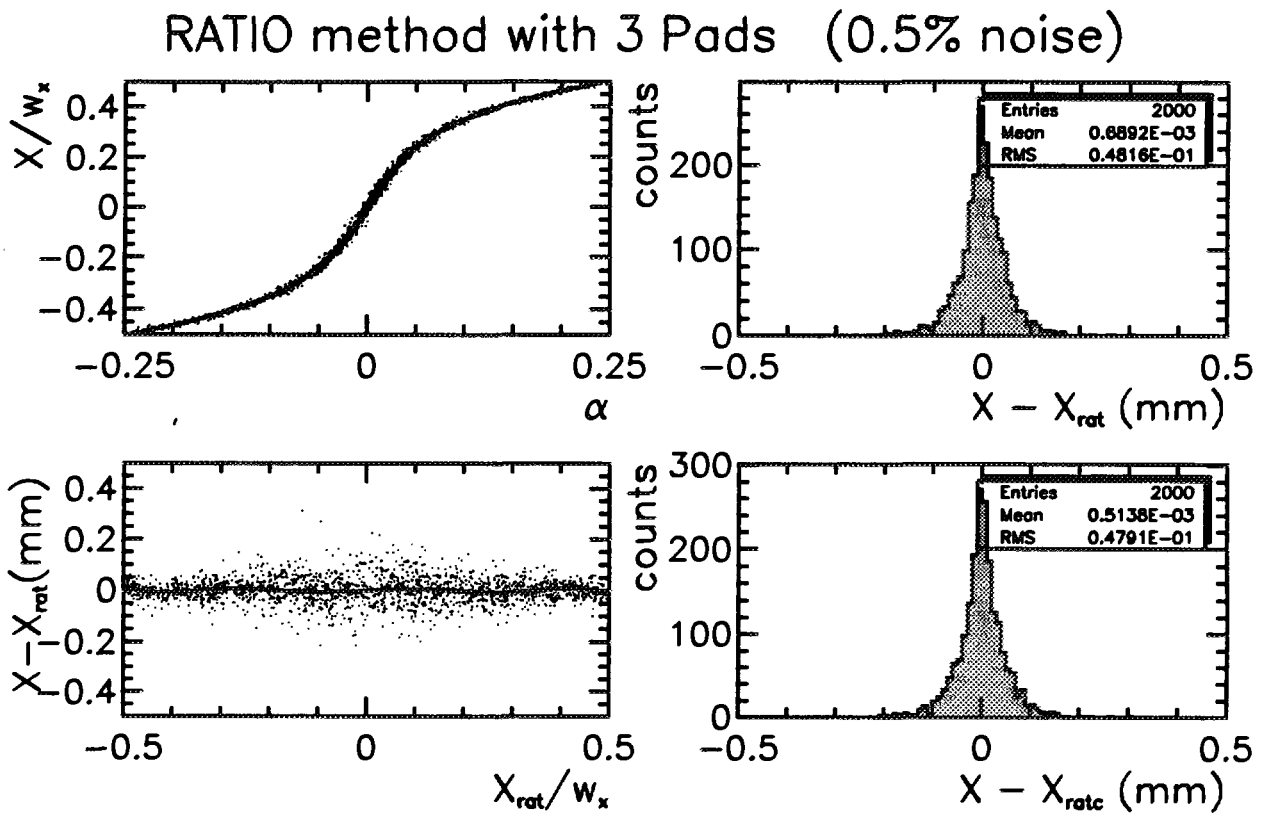

Figure 4.6: *Charge ratio method (with 0.5% noise) using 3 consecutive pads. In (a) one sees the relation between the normalized position and α from eq. 3.8. The width of the curve is governed by the bin size of 100 channels but noise becomes visible in the center of the curve. The fit from eq. 3.8 is also shown. (b) gives the resolution using the fit of eq. 3.9. The σ_x for all events is about 48 μm. (c) and (d) show that there are no systematic deviations visible and therefore further corrections (as for data without noise) does not improve the result of (b).*

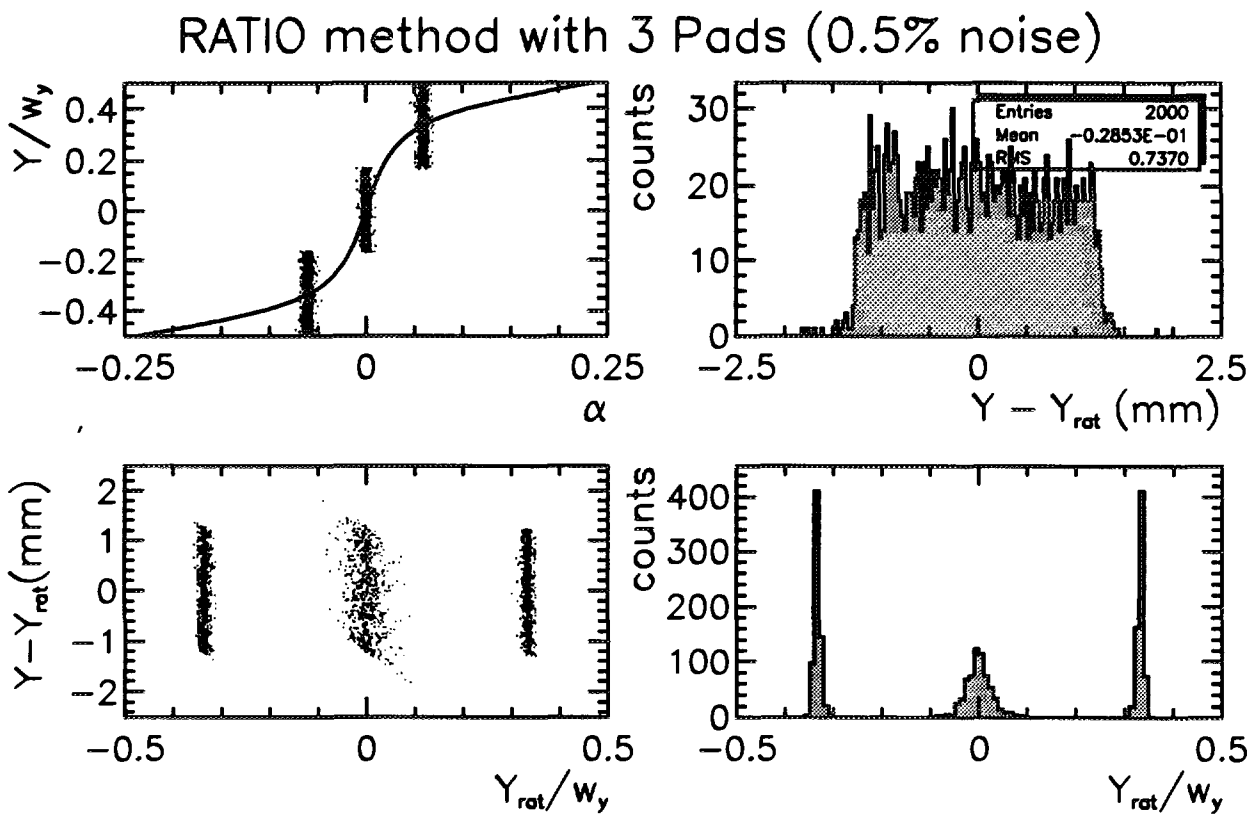

Figure 4.7: *Charge ratio method in Y-direction (with 0.5% noise) for 0° using 3 consecutive pads. In (a) one sees the relation between the normalized position and α from eq. 3.8. The 3 vertical strips are the data from the 3 discrete wires. The curve shows a fit used to calculate the position. It is generated like for continuous events. (b) The resolution is 737 μm. (c) shows the that there are only small systematic deviations. And (d) shows that the wire number can be properly reconstructed.*

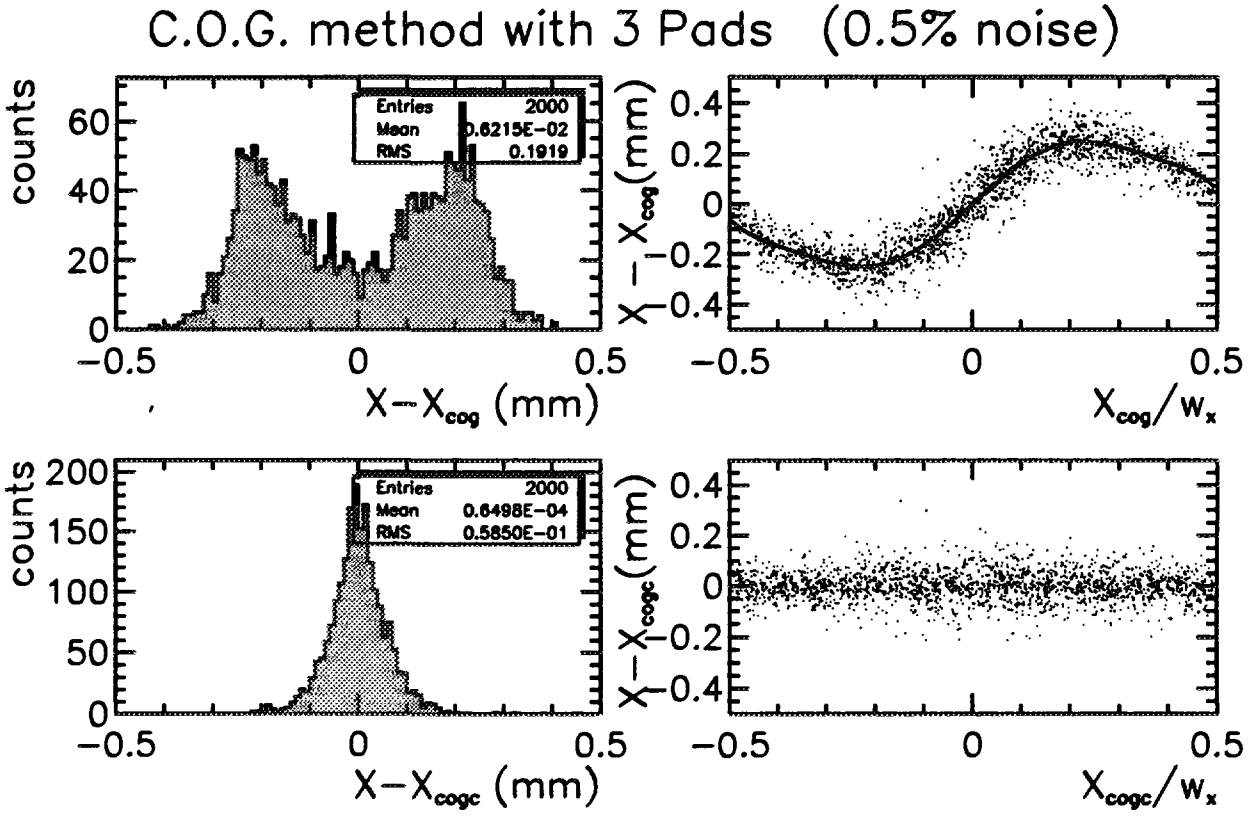

Figure 4.8: *Center of gravity method (with 0.5% noise) using 3 consecutive pads. (a) gives the resolution using eq. 3.3. The σ_x for all events is about 192 μm. (b) shows the systematic deviations which attain a mean amplitude of about 240 μm near 1/4 and 3/4 of the pad. In (c) one sees the resolution after correction with the fit-polynom of 7th degree in fig. (b). (d) There are no remaining sytematic deviations visible.*

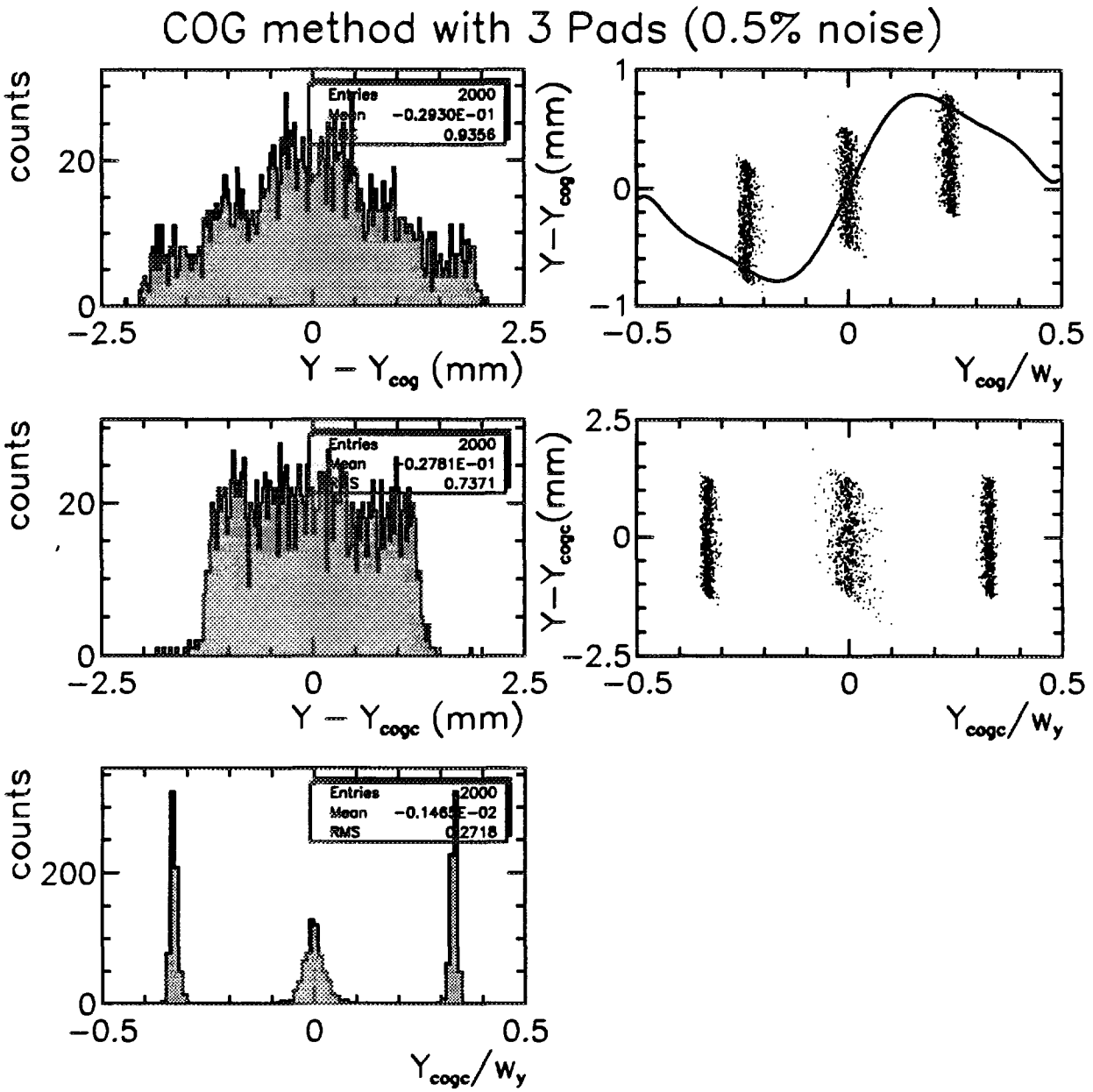

Figure 4.9: *Center of gravity method in Y-direction (with 0.5% noise) for 0° using 3 consecutive pads. In (a) one sees that the resolution using eq. 3.3 is already better than 1 mm. (b) shows systematic deviations and the fit. (c) gives the resolution after the correction ($\sigma_y \approx 737\mu m$). (d) shows that there remain only small systematic deviations. In (e) the wire positions are properly reconstructed.*

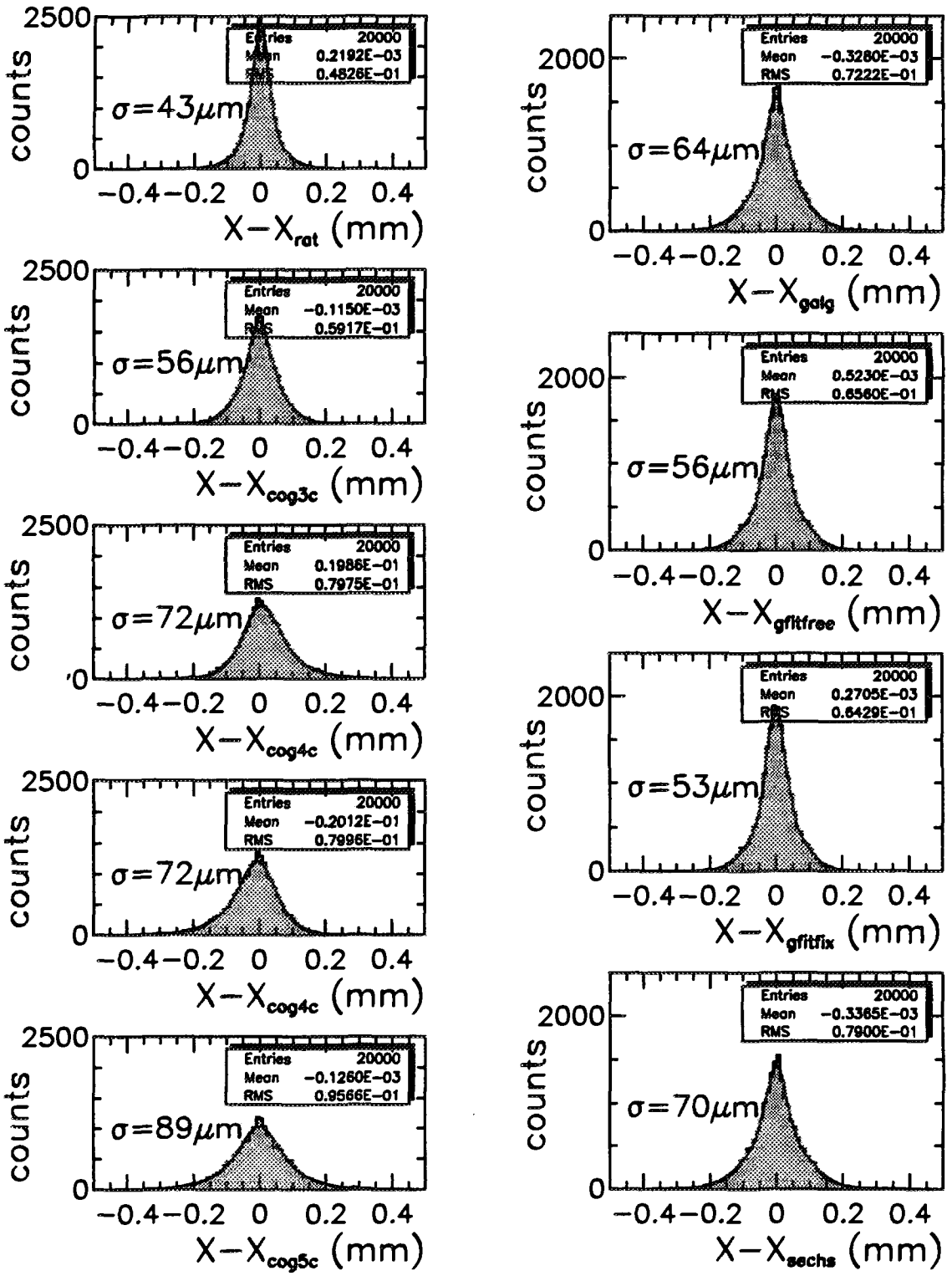

Figure 4.10: *Resolution for different position reconstruction algorithms. The ratio algorithm (a) shows the best resolution. (b)-(e) show the degradation of the resolution with the number of pads used in the c.o.g. algorithm (3, 4(left), 4(right) and 5). (f) Gaussian algorithm; (g) Gaussian fit with 3 parameters; (h) Gaussian fit with amplitude and σ fixed; (i) SECHS algorithm. All simulations were done with 0.5% noise contribution and with* $w_x = 5mm$, $w_y = 7.5mm$, $d = 2.5mm$ *and at 0°. The σ displayed is the weighted σ from a fit with 2 Gaussians which is also shown in the spectra.*

plot in fig. ?? shows finally the resolution achieved with the SECHS algorithm (see appendix A.2). The resolution is poor, only 70 μm, in disagreement to ref. [30]. This is quite surprising as the description with this function is rather close to the Mathieson charge distribution (see fig. 2.2).

4.3.2 2-pad algorithms

The 2-pad c.o.g. like and 2-pad ratio like algorithms working with the charge ratios of the left/center and right/center pads were described in section 3.4. The situation with noise is much different from without noise, because the signal-to-noise ratio becomes very small when there is only few charge on the corresponding side pad. Figs. 4.11 and 4.13 show the results in X-direction with 0.5% noise contribution.

For the c.o.g. algorithm one can see on fig. 4.11 that correction of systematic deviations will not improve the width of the peak. The resolution increases enormously as soon as the impact is on the non neighbouring half of the center pad to the corresponding side pad. Nevertheless the resolution is good or even very good on the neighbouring half (see also the following section).

In Y-direction one finds a bad resolution for the wire which is opposite to the used side-pad (fig. 4.12). Nevertheless the overall resolution is less than 1 mm which ist acceptable for ALICE Di-Muon Arm purposes. Systematic corrections have only a small effect.

The resolution for the 2-pad ratio like algorithm is almost the same, but there one step of systematic correction has to be made (see fig. 4.13). In Y-direction one finds again a resolution of less than 1 mm (fig. 4.14).

4.3.3 Resolution dependence from the impact position on the pad

Khovansky *et al.* [7] and others [24] have shown that the resolution is not uniform over the strip or pad but worsening around the pad center. This can be qualitatively understood that near the edge of the pad the charge is mainly shared by two pads, while for a center hit the induced charge on the side pads is rather small and thus the signal to noise ratio is small. This results in larger errors for the position determination near the center of the pad. By the way in [7] there was found not much difference between ratio and c.o.g. algorithm.

Our simulations show on the contrary important differences between ratio and c.o.g. algorithm. The resolution in dependence of the impact position on the pad is shown on fig. 4.15a. The data were binned in ten equidistant sets along the relative position on the pad. The solid circles are for the charge ratio algorithm, while the solid boxes are for the c.o.g. algorithm using 3 pads. In the pad center the resolution is the same for both algorithms, but near the borders the ratio algorithm is 20 μm better. The effect of decreasing resolution near the center of the pad is connected with the nonlinearity of the algorithm and will be more discussed in the next section. A perfect linear algorithm would not show differences in the resolution between the sides and the center of the pad.

The hatched lines with open symbols in fig. 4.15a show the results for the 2-pad algorithms. One can see that the resolution dependence follows closely the behaviour of the ratio algorithm. On the outer thirds of the pads its resolution is even slighly better than the ratio algorithm [7]. However, near the center of the pad the resolution with the 2-pad algorithms is already 100 μm. One would then switch from the left/center to the right/center ratio, but then the complete charge ratio method can immediately be used. Fig. 4.15b shows with different vertical scale the resolutions of both 2-pad algorithms. The resolution is for both methods within statistics the same. Unfortunately it increases when the impact is near the opposite side to about 700 μm which is far too bad for most purposes.

4.3.4 Resolution dependence on the electronic noise

In fig. 4.16 the resolution achieved with the c.o.g. for 3 pads and the ratio algorithm is plotted as a function of the electronic noise σ_{noise} with the stan-

[7] This might come from the fact that no low signal-to-noise charge from the opposite side-pad is added.

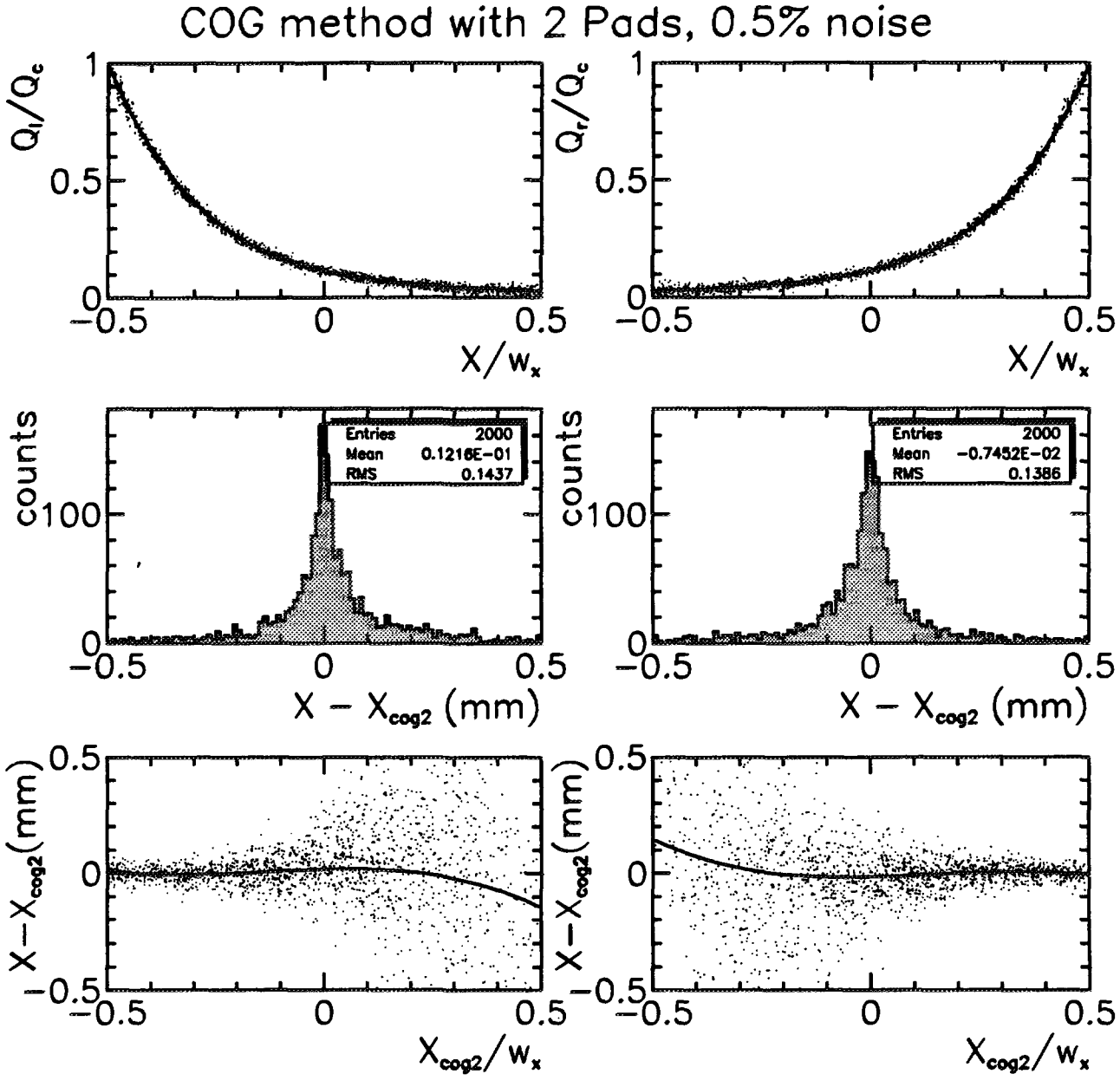

Figure 4.11: *2-pad c.o.g. algorithm with noise. (a) and (b) show the ratio of charges left (right) to the center pad as a function of the relative position on the pad. The relation is fitted to calculate X_{cog} from the charges (see text). Note that the width of the curve is dominated by the bin-size (100 channels). (c) and (d) show the residuals of the calculated position with the real position. (e) and (f) show the resolution as a function of the relative impact position on the pad. This shows clearly that the 2-pad algorithm has a good resolution if the impact is on the part of the pad that is closer to the used side pad.*

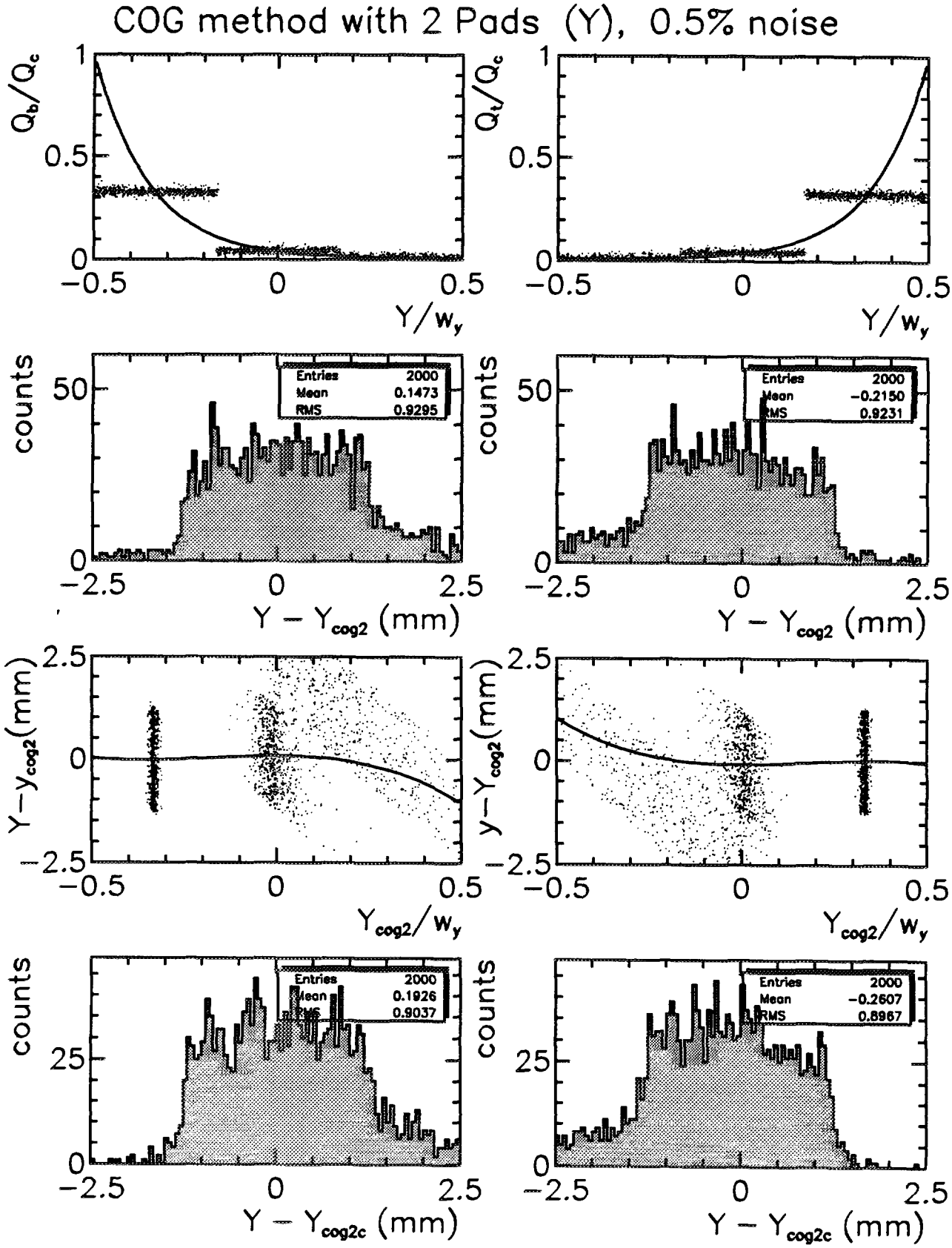

Figure 4.12: *2-pad c.o.g. algorithm in Y-direction at 0° with noise. (a) and (b) show the ratio of charges bottom (top) to the center pad as a function of the relative position on the pad. Two wires are clearly seen while the 2-pad charge ratio for the 3rd is almost 0. The curves shown were generated for continuous spectra like for the X-coordinate. The position reconstruction gives a standard deviation for the residuals ((c) and (d)) below 1 mm. And after correcting for systematic deviations ((e) and (f)) the reconstruction is even slightly improved ((g) and (h)).*

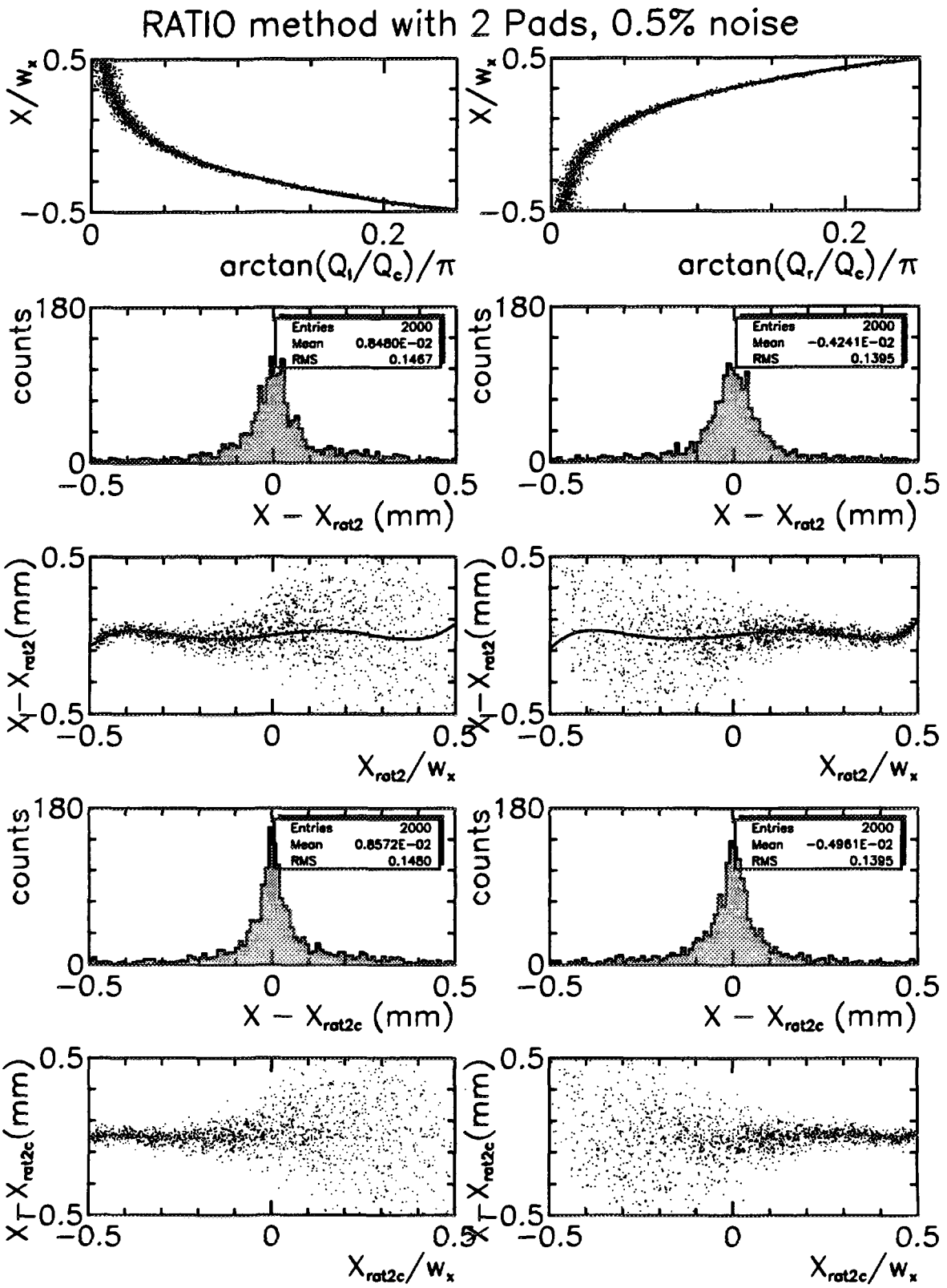

Figure 4.13: *2-pad ratio algorithm with noise. (a) and (b) show the relative position on the pad as a function of the* arctan *of the charge ratio left (right) to the center pad. The relation is fitted to calculate* X_{rat} *from the charges (see text). Note that the width of the curve is dominated by the bin-size (100 channels) but noise effects are visible for small values of the* arctan. *(c) and (d) show the residuals of the calculated position with the real position. (e) and (f) show the remaining systematic deviations and their fit (see text). (g) and (h) show the resolution after systematic correction which is now the same as from the 2-pad c.o.g. (i) and (j) show the resolution as a function of the relative impact position on the pad.*

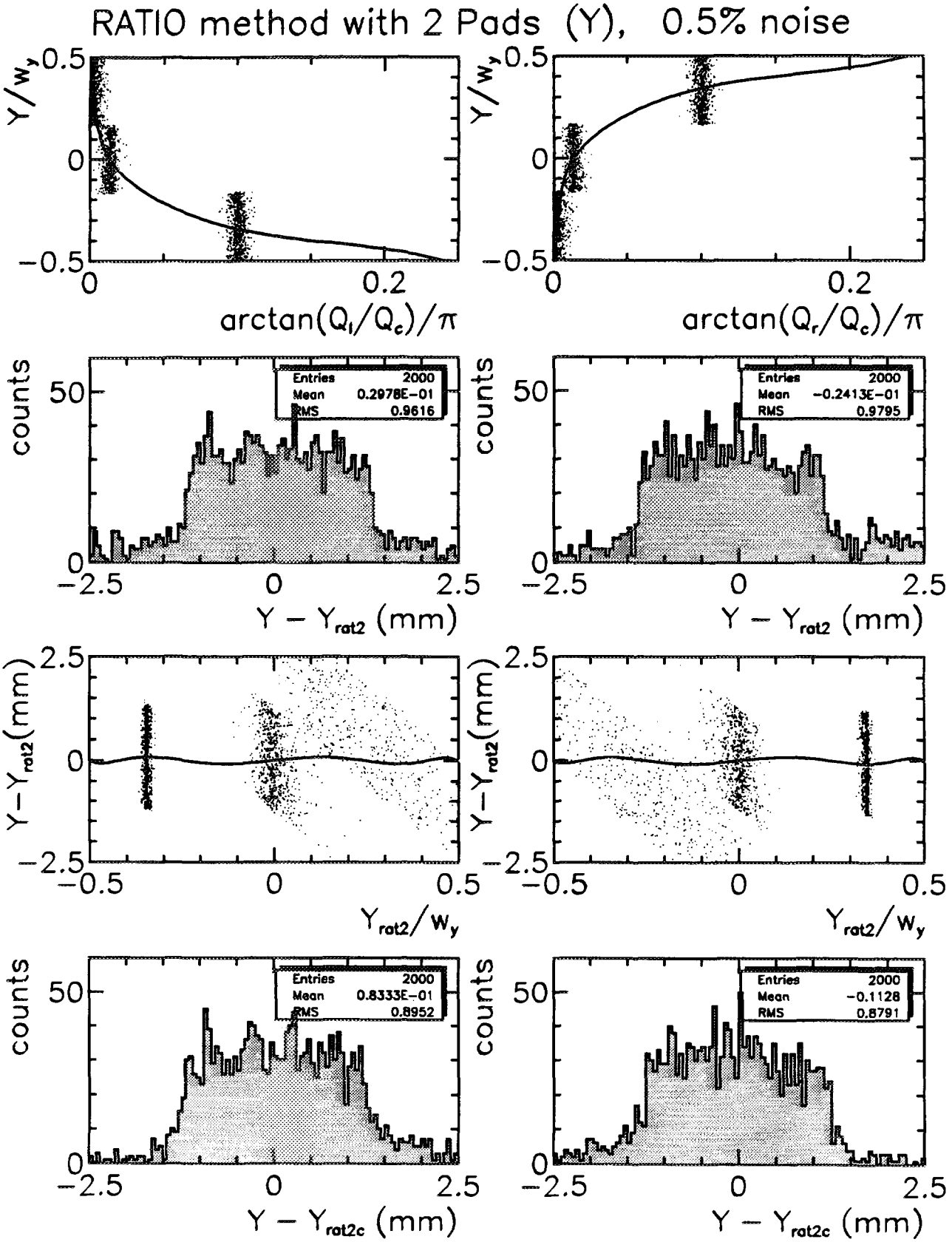

Figure 4.14: *2-pad ratio algorithm in Y-direction at 0° with noise. (a) and (b) show the relative position on the pad as a function of the* arctan *of the charge ratio bottom (top) to the center pad. Two wires are clearly seen while the 2-pad charge ratio for the 3rd is almost 0. The curves shown were generated for continuous spectra like for the X-coordinate. The position reconstruction gives immediately a standard deviation for the residual below 1 mm ((c) and (d)). Correction for systematic deviations ((e) and (f)) leads to slight improvements ((g) and (h)).*

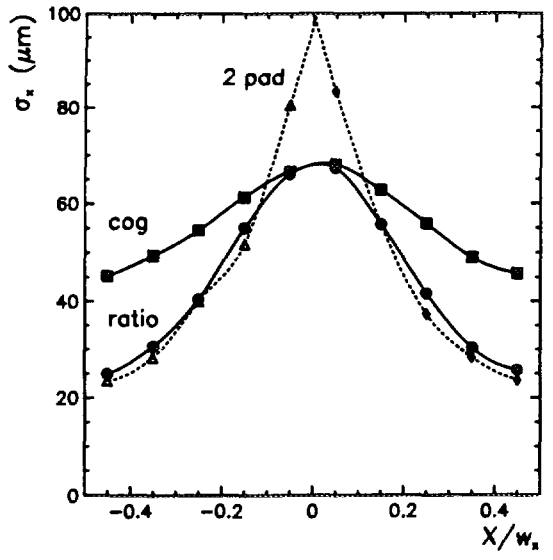

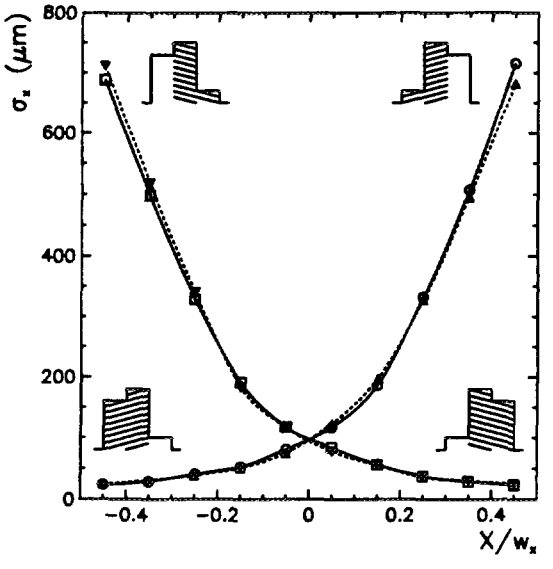

Figure 4.15: *Resolution as a function of the impact position (X/w_x) for 2- and 3-pad algorithms. (a) Circles: ratio algorithm, squares: c.o.g. algorithm. Open symbols and hatched lines: c.o.g.-like 2-pad algorithm. For the latter there are two possibilities using Q_l/Q_c or Q_r/Q_c. Note that the 2-pad algorithm is even slightly better than the ratio algorithm on each outer 3/8 part of the pad. Near the center of the pad the signal-to-noise ratio becomes too bad. (b) Full symbols: ratio-like 2-pad algorithm, open symbols: c.o.g-like 2-pad algorithm. There is almost no difference between the two methods. When the impact is near the opposite side of the used side pad the signal on this pad is of the order of the noise and therefore the resolution is very poor in this region. This is illustrated with the upper charge distribution spectra. The hatched area is used in the 2-pad algorithm. The blanc area is not used and lost for the resolution performance.*

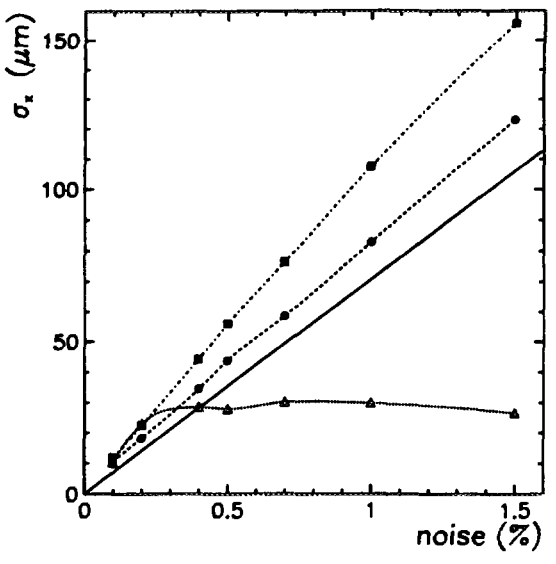

Figure 4.16: *Resolution as a function of the electronic noise level for the ratio and c.o.g. algorithms with 3 pads in the CPC standard lay-out. Solid line: approximative relation from eq. 3.7 noted by Lau et al., dash-dotted line and solid squares: resolution with c.o.g. algorithm, dashed line and solid circles: resolution with ratio algorithm, dotted line and open triangles: difference in % between c.o.g. and ratio algorithm.*

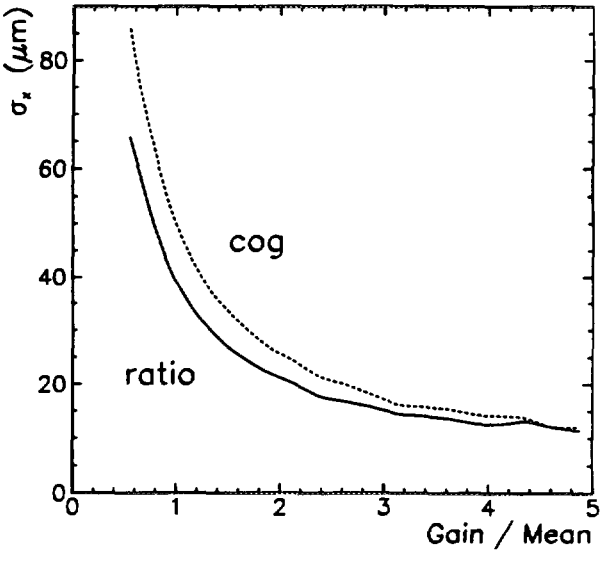

Figure 4.17: *Resolution as a function of the total induced charge normalized by its mean value in the standard CPC lay-out. Solid line: charge ratio algorithm, hatched line: c.o.g. algorithms with 3 pads. The curves are for a mean noise amplitude of 0.5% (see fig. 4.1). Note that most events are in the range of 0.5 to 1.5 around the mean value. The mean resolutions for both algorithms are the same as in fig. 4.10.*

dard CPC lay-out. The ratio algorithm (hatched line) gives throughout better results as the c.o.g. method (dash-dotted line). The difference in percent between the two methods is shown as a dotted line. Above 0.3% noise level the ratio algorithm gives resolutions that are about 30% better. The full line gives a prediction of the resolution with the simple formula of Lau *et al.* [8] given in eq. 3.7. The prediction underestimates the observed values. This might come from a different definition of the noise level. We put the level on the mean of the total charge generated by the Landau distribution.

Leaving the noise contribution constant (0.5%) and plotting the resolution as a function of the normalized height of the total induced charge on the cathode pads gives a similar picture. The graph in fig. 4.17 shows that ratio and c.o.g. method will differ in the spatial resolution for signal height up to at least 4 times of the mean value. Most of the statistics is of course found near the mean value where the ratio algorithm is about 25% better.

4.4 Comparison of different chamber lay-outs and their optimization

In a some publications [6, 7, 9, 16, 35] the optimum ratio of strip width w_x (readout pitch) and cathode–anode spacing d was calculated, measured or simulated, however surprisingly not always with the same result. While [6, 9, 16] agree to an optimum width w_x of about 1.0 d, others find a higher ratio of $w \approx 1.4 - 1.6\ d$ [7] and even $w \approx 1.5 - 2.0\ d$ [35] . With the observations made in the preceeding chapter we think we can say that there might be a more complicated relation, which is supported by the calculations of Chiba *et al.* [35] that there is a much stronger resolution dependence if one varies d and leaves w_x constant. In fact one has to variate both parameters w_x and d. Keeping one parameter constant, *e.g.* d, the best resolution may be found for some w_x, but there might exist better $w_x - d$ couples. The reason is the nonlinearity of the system. The optimum would be reached for the linear case [8]. This is what we try to show in he following.

[8] which is perhaps in practice not exactly reachable

Furthermore Bencze *et al.* [24] have recently shown, based on results of Yu *et al.* [40] and other work, that nonlinearities might be minimized with capicative coupling of intermediate strips inbetween the readout pitch. There exists an optimum width ratio w_f of these intermediate strips for a given capacitive coupling.

We then choose a standard noise level with $\sigma = 0.5\%$ and compare the relation for α as a function of the relative impact position on the pad and the resolution variation on the pad. On fig. 4.18 we show the two figures for $w_x = 5$ mm and $w_x = 7.5$ mm. An important feature can be seen by comparing the 2 different pad dimensions. The resolution on the pad depends strongly on the rise of the $\alpha - X_{rel}$ relation, which reflects the nonlinearity of the system. The nonlinearity increases with the pad size [9] and thus degenerates the resolution. In fact the resolution would be best over the whole pad if $\alpha - X_{rel}$ were linearily related. This observation will help us in the following to optimize the chamber lay-out for a demanded resolution. Once the noise and error contributing sources are known or measured a chamber can within some limits be designed to achieve a distinct performance.

4.5 Conclusions on the resolution degrading parameters

In this chapter the main sources which influence the spatial resolution of a pad or strip chamber have been listed and discussed. They can be classed in 3 groups with respect to their origin:

- mechanical tolerances
- electronic tolerances (noise, cross-talk, ADC)
- effects coming from the ionizing particle itself: inclined tracks, delta electrons

Simulations and verification of mechanical tolerances have shown that the specifications can be reached with modern production techniques. Accurate work is demanded which is time consuming but can be reached in laboratories with good equipment.

[9] leaving d constant

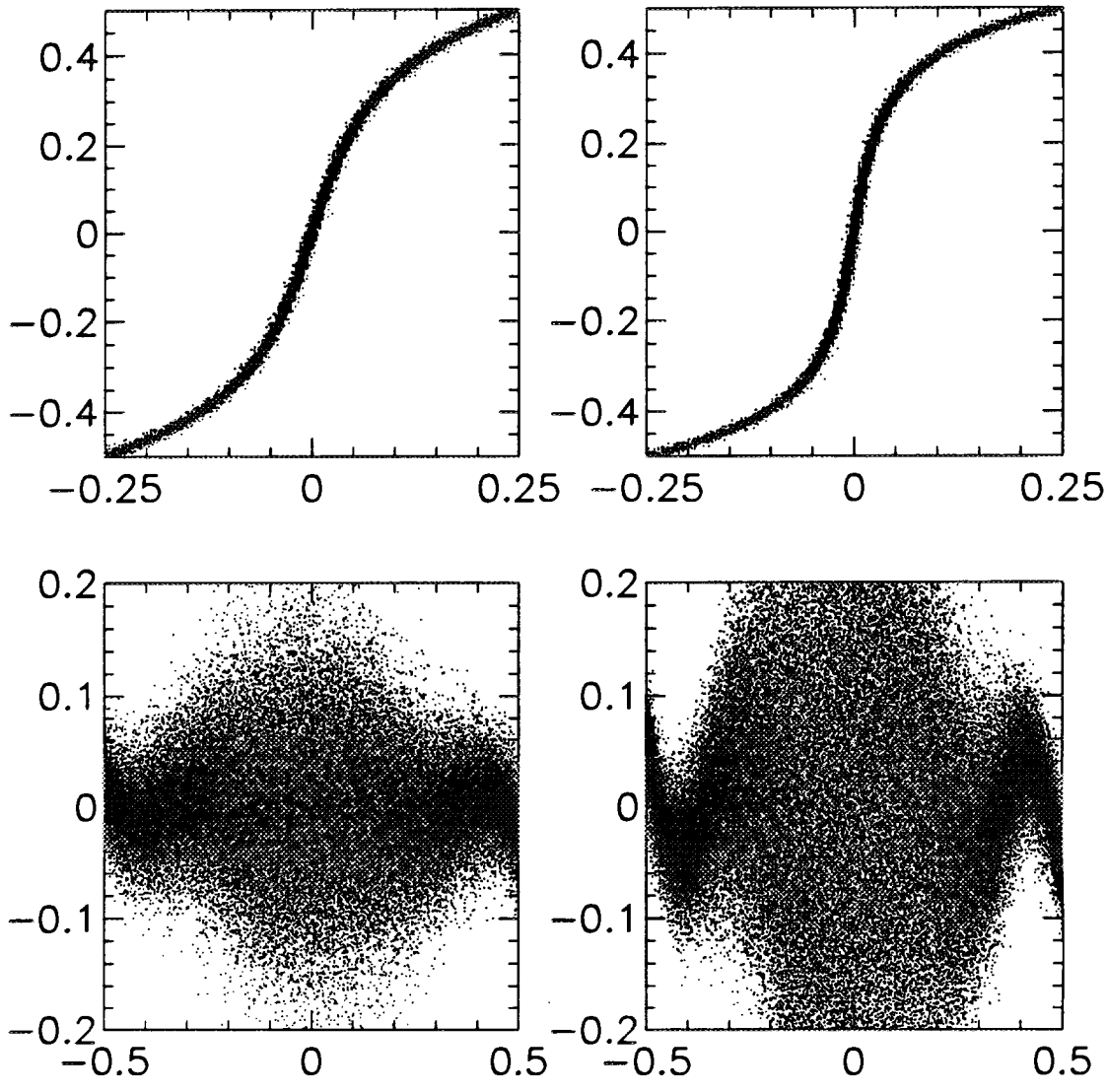

Figure 4.18: *Charge-ratio algorithm for different pixel sizes. Above line: relative position inside the pad as a function of α for $w_x = 5$ mm and $w_x = 7.5$ mm. Bottom: residuals as a function of the relative position.*

The handling of electronic noise, cross-talk etc. seems to be far more difficult as it is usually the limiting factor of the spatial resolution which is achieved with CSC's. Therefore special efforts are demanded on the engeneering and cost side. Considerable progress has been made in the last years and it seems that the electronic noise contributions will soon approach the low level of other error sources. Nevertheless it is very important to reduce costs per readout channel, so that not the costs are the resolution limiting factor. However, it is very important to optimize the chamber design itself, so that a minimum number of readout channels is necessary. But low noise electronics would aim in the same direction: one can increase the readout pitch if the intrinsic noise contribution is already very low.

Effects connected with the particle itself will depend of course mainly on the experiment. Perhaps chamber planes can be oriented to face the direction from where most particles come from. But usually one would align the detectors with the beam axis. For the Di-Muon Arm in the ALICE detector the problem is not important because the angular range is limited to 10° and most particles are expected at 2° or 3°. For the production of delta electrons it is of course advantagous to have as less material as possible in the way of the particle track.

Chapter 5

Double-hit separation and resolution

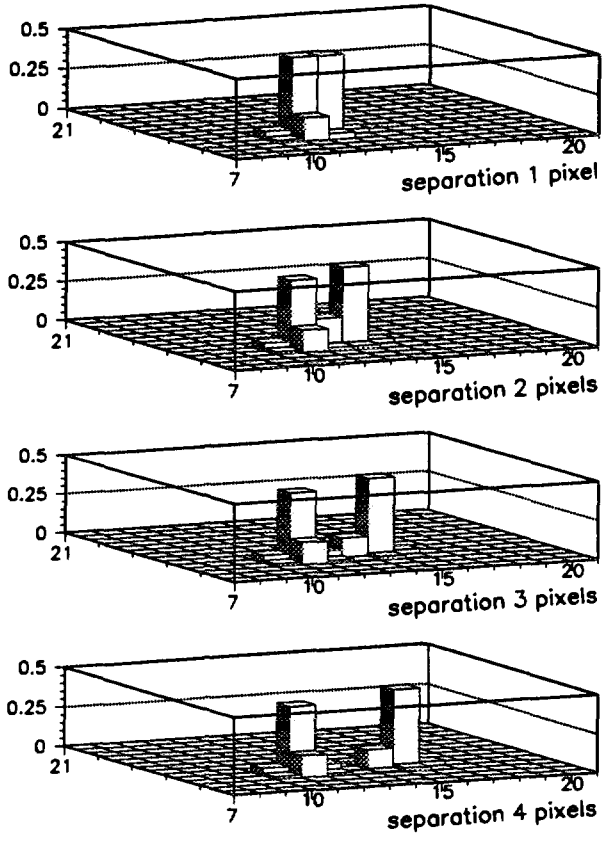

Figure 5.1: *Different types of double-hits shown here with the same signal height. If the separation is 3 pads, the two hits can be treated as singles without resolution degradation.*

The resolution of double-hits is a central problem for the usage of CPC's in the ALICE experiment due to the high particle multiplicity in heavy-ion collisions. CSC's were in the past criticized for not being capable to separate nearby tracks. The question is rarely treated in the literature. We only found the problem treated to some extend by Fenker, Thomas *et al.* [15, 16], Gratchev *et al.* [42] and by Yu [14]. The problem has been treated by the first two groups using a standard fit routine from the HBOOK [1] package. Unfortunately this procedure is CPU time consuming but can be performed in offline analysis. Yu has stated that looking at the charge ratios Q_l/Q_c as a function of Q_r/Q_c exposes some caracteristic features which can help to distinguish between single- and double-hits.

Nevertheless for both methods a big problem is that the induced signal heights for two nearby hits may be very different due to the long Landau tails. So one has at least 3 unknown quantities, the 2 impacts positions [2], where in case of the pad chamber this is a two-dimensional problem (X–Y), and the pulse height ratio of the two signals. It is clear that the resolution becomes worse when the two impacts are at a distance of less than one pad size, or when the signal heights are very different. In the latter case the *small* event stands in the *shadow* of the big one and can not be seen.

We will first show in detail how by a combination of several algorithms double-hit treatment can be performed. The efficiency and spatial resolution is studied. The results will then be compared with double-hit deconvolution by fits.

5.1 Cluster identification

Clusters from impacts have been identified with a simple *maximum finding* routine which makes a scan over the whole chamber array [3]. The threshold for pixels to be accepted in this analysis was chosen to

[1] from the CERN Program Library

[2] It is eqivalent to say the distance of the impact and the mean position of the two hits are unknown.

[3] This might be accelerated if one knows the pixels who gave a signal above a certain threshold.

be about $4 - 5 * \sigma_{noise}$ above the mean noise level to avoid identification of noise as particles. The threshold depends of course on the electronics performance, the chamber design and the available gain without creating too many overflows in the ADC's. Nevertheless all clusters with a distance of 3 or more pads (with the standard geometry) do not overlap and can be treated as two single-hits.

5.2 Identification of double-hits using algorithms

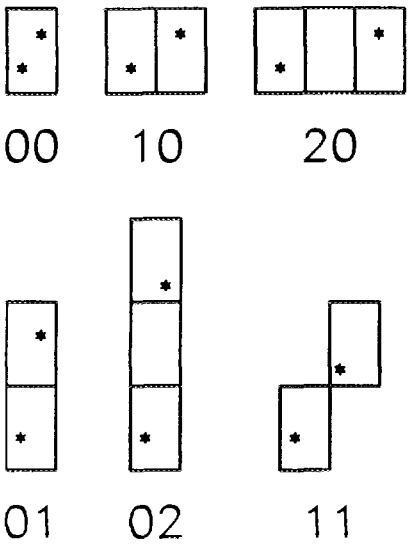

Figure 5.2: *Notation (XY) for double-hit patterns. The stars are impacts on the pads. The number pairs give the pad distance in X- and Y-direction.*

The first question is of course how to identify a double-hit, what is the difference to a single one. This is not trivial if the impacts points of the two hits are less separated than the FWHM of the charge distribution, or more practically if the distance is less than one readout pitch. In principle each hit is subject of a double-hit check, because for 2 nearby tracks the signature is almost the same as for single-hits. A classification scheme for double-hits is shown in fig. 5.2. The notation indicates the separation of pads in X- and Y-direction. So 00 stands for two impacts on the same pad, 10 for impacts on pads neighboured in a X-row, 01 for impacts on pads neighboured in a Y-column, etc. If one wants to work with algorithms to find the impact positions the knowledge of the pads where the impacts took place is important. For overlapping induced charges the hit-pattern of identified maxima is unfortunately not necessarily identic with the pad numbers where the charge maxima are observed.

Nearby double-tracks may not be separated by the measurement of the total charge in the cluster, because the pulse height can be very different even for the same particle type due to the long Landau tails in the energy loss distribution. The only clear information can come from the width of the observed charge measurement. But the width can only be determined with some uncertainty due to noise and the low number of involved pads in each cluster.

We first applied a simple maximum finding loop to the chamber matrix. This method can already identify double-hits which still show clearly separated maxima. They can be treated as single hits if they are separated by at least 2 pads (20, 02, 12, 21, etc.). All other maxima a subject of a test if they are not a close double-hit.

We propose 3 methods using algorithms to test a maximum on whether it is a double- or a single-hit:

- The cluster size is checked by calculating the ratio of the charge sum in a cluster of 3×3 pads (Q_{33}) around the central pad with a cluster of 5×5 pads (Q_{55}). With our standard geometry one finds always more than 98% of the total charge Q_{33} for a single hit. This will of course be influenced by the noise contribution.
- The width (σ) of the maximum is checked in both dimensions X and Y with the Gaussian algorithm (σ_{gx} and σ_{gy}).
- The charge ratio of the right/center pad plotted as a function of the left/center pad as well as top/center in combination with bottom/center gives valuable information about double-hits [14].

It is clear that some double-hits can not be differenciated from single hits, in the case they are very close (< 2 mm in both directions) or the energy loss is very different, so that the smaller signal disappears in the tail of a large peak. Nevertheless there

might come additional information from other chamber planes connected by the tracking routine.

Peak width calculated with Gaussian algorithm

The efficiency of each proposed method is depending in a different way on the distance of the two impacts. The combination of all 3 methods yields in the best result valid for all distances. Figs. 5.3–5.10 will illustrate advantages and disadvantages. The first figure (5.3) shows the normalized σ_g's, σ_{gy}/w_y as a function of σ_{gx}/w_x, calculated with the Gaussians algorithm (see appendix A.1). The upper left plot shows the result for 50000 single hits. The majority of events is concentrated in the black spot. The slight enhancement near $\sigma_{gy}/w_y = 0.2$ is due the discrete structure given by the anode wires in Y-direction. This peak corresponds to the middle wire (see fig. 1.3) in the case where almost no charge is induced on the top and bottom pad. In that case the width calculation comes only from the charge on the center pad and gives a too small value. The dashed line shows gates that can be put on the single data. Unfortunately there are rather broad tails next to the prominent peak due to noise. If they would not exist one could set the gates much closer to the peak with important advantages for the recognition of double-hits. In the experiment the majority of identified clusters are single-hits, so these should not be confused with double-hits. The gates shown let only pass about 0.8 % of single-hits. The 3 other graphs in fig. 5.3 show $\sigma_{gy} - \sigma_{gx}$ pairs for double-hits selected [4] for different pattern situations: 00, 10 and 01. One can see in the figure that the method is more or less successful depending on the hit pattern. The localized structures in Y-direction always reflect the wire structure.

The dependence of σ_{gx} from the distance in X-direction is displayed in fig. 5.4. For double-hits on the same pad an almost clean relation between σ_{gx} and the distance exhibits. Unfortunately as we will see below is is not trivial to separate these events from events on neighbouring pads (see fig. 5.4) were the relation is much less clear. The dashed line marks again the gate which was set for single hits. For hits neighboured in Y-direction (01) no surprise occurs, but for the situation 20 two strange structures appear for large distances (> 6 mm) and low σ_{gx}. This is an inconvenience of the algorithm working only with consecutive 3 pads. The charge is now spread over 4 or even 5 pads, though still appearing with a single maximum. This situation can in most cases be recognized, because one can find a considerable amount of charge above noise on the side pads that are further away from the center pad. We have realized that it is also in the 10 situation the case for a large number of hits when the separation is more than 6 mm. The 6 mm is a rather clean border. It is not clear why does not coincide with the pad width of 5 mm. However most of the far separated events can be identified.

The dependence of σ_{gy} from the distance in vertical direction is shown in fig. 5.5. As already mentioned the localized structures come from the discrete wire structure. For example for double-hits on the same pad the two structures above the dashed gate line come from events with one hit on the top and one hit on the bottom wire. Therefore the σ_{gy} is large. The large structure in the middle is from events with one hit on the top or bottom wire and the other on the middle wire, or both hits on the middle wire. Finally the small low structure is created when both hits one on the top or bottom wire.

Estimation of the cluster size

The cluster size can be estimated by comparing a simple charge addition around the pad with the maximum charge. In the standard chamber lay-out more than 98.5% of the induced charge is always on the 9 pads (3×3) in the neighbourhood of the impact (see fig. 5.6). Comparing the summed charge on these 9 pads with the charge on the 25 pads (5×5) around the pad with the charge maximum, will give in some cases information if a second hit is present. The noise on each pad, which is summed up as well, will of course limit the reach of this procedure. In fig. 5.7 one can see the efficiency of the method. The ratio of the 9 pad to the 25 pads (9/25) is plotted as a function of the normalized Gaussian σ_{gx}, that was already shown in fig. 5.3. The dashed lines indicate again the gates

[4] The selection is made when the events are generated. In truth one has a combination of all these cases. We generate 50000 double-hits with uniform distance distribution. The first hit is generated randomly on one pad. The distance $r = \sqrt{x^2 + y^2}$ to the second hit is then randomly drawn between 0 and 25 cm. The orientation ϕ is then randomly drawn between 0° and 180°.

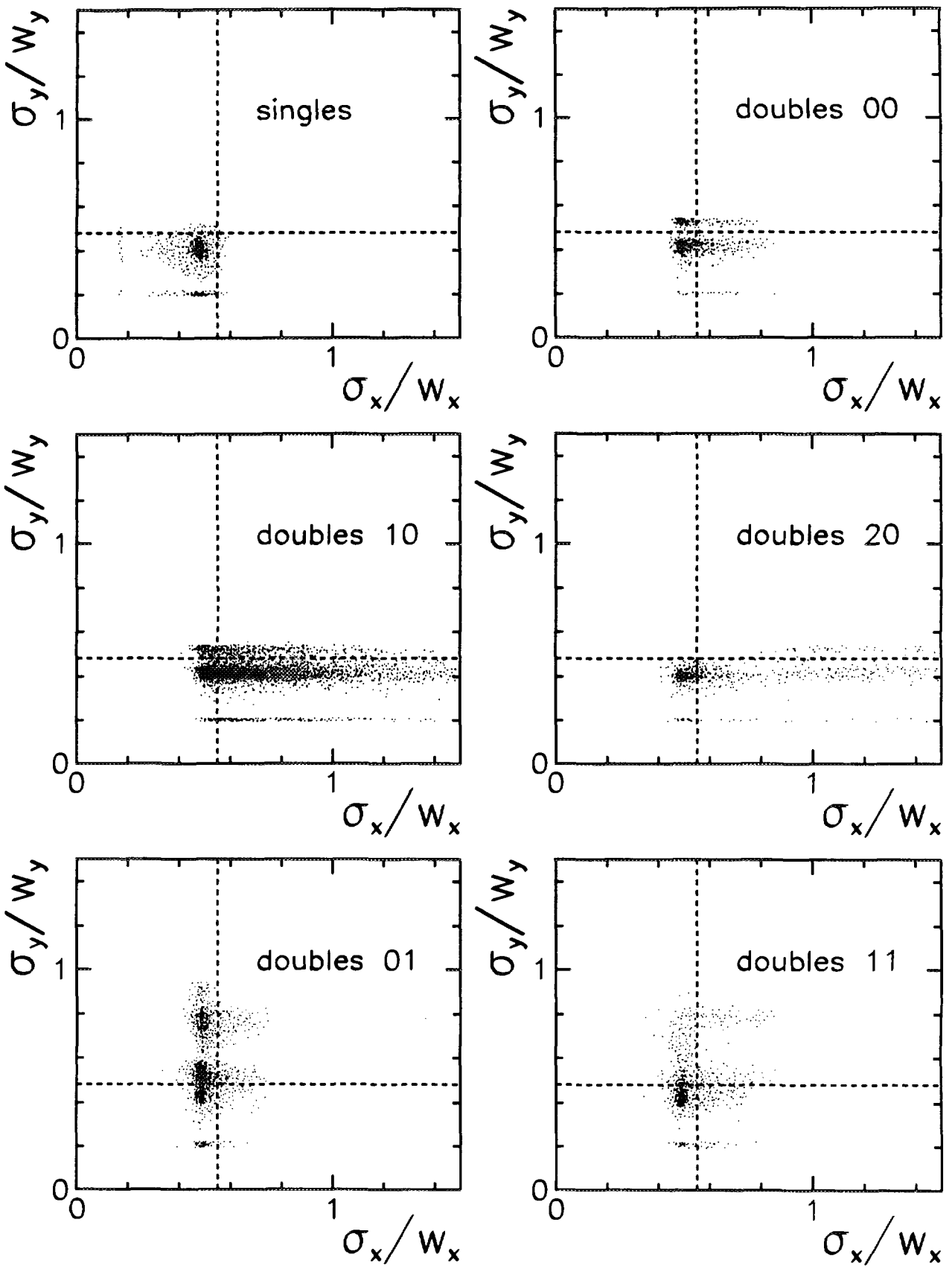

Figure 5.3: *Normalized standard deviations σ_g in X- and Y-direction calculated with the Gaussians algorithm for single- and double-hits. The dashed lines mark the gates set on the single-hits. There are 50000 events in the single-hit plot, only 0.8% are above the gates.*

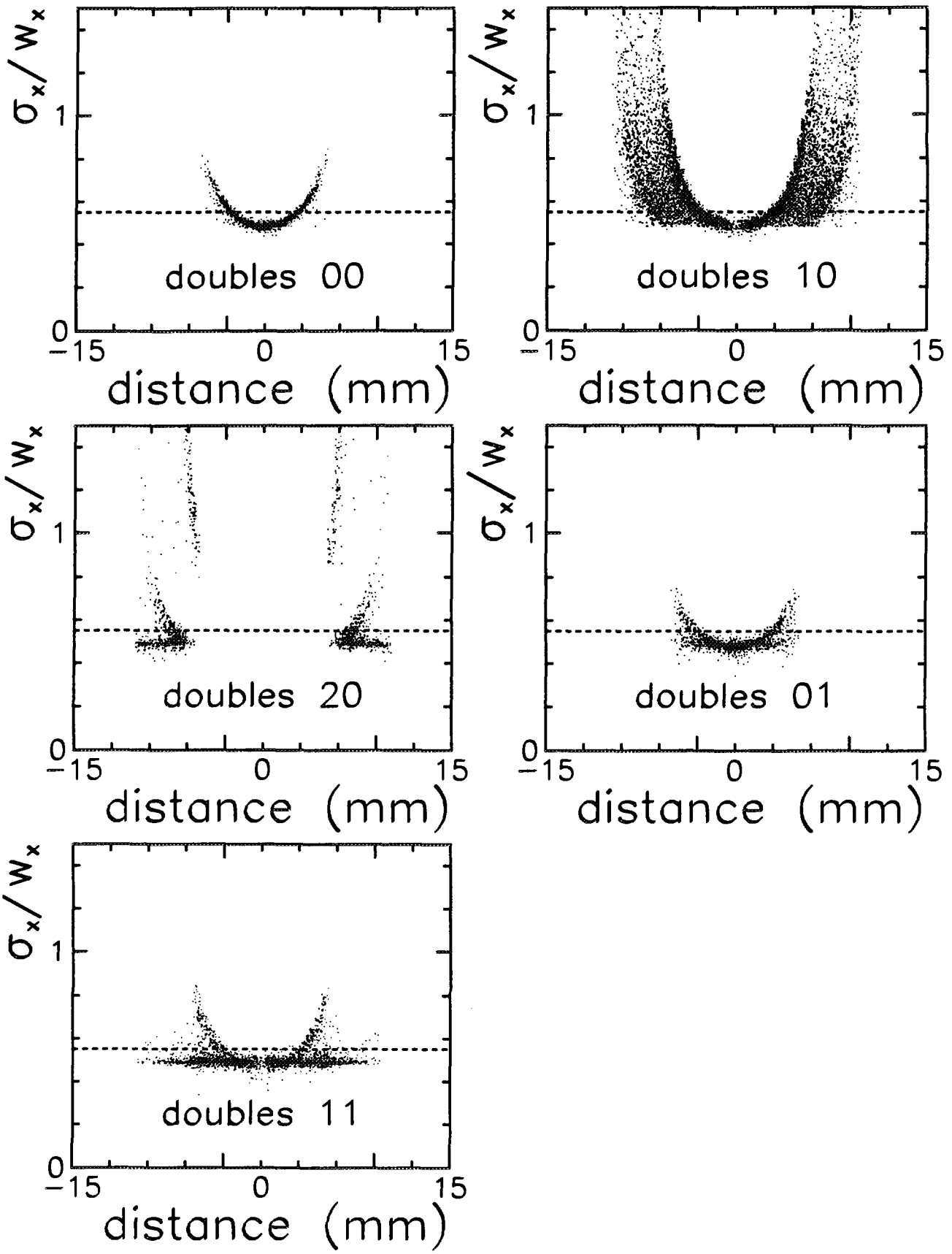

Figure 5.4: *Normalized standard deviations σ_x from the Gaussian algorithm as a function of the impact distance of double-hits in X-direction. The dashed line marks the gate that was set on single hits. Note the clean functional behaviour for double-hits on the same pad. Double-hits can be separated by this method from about 3 mm distance on with good efficiency. Note that the gate seems even too high. For larger pad distances (20) the caculation of σ does not work properly. The correction is explained in the text.*

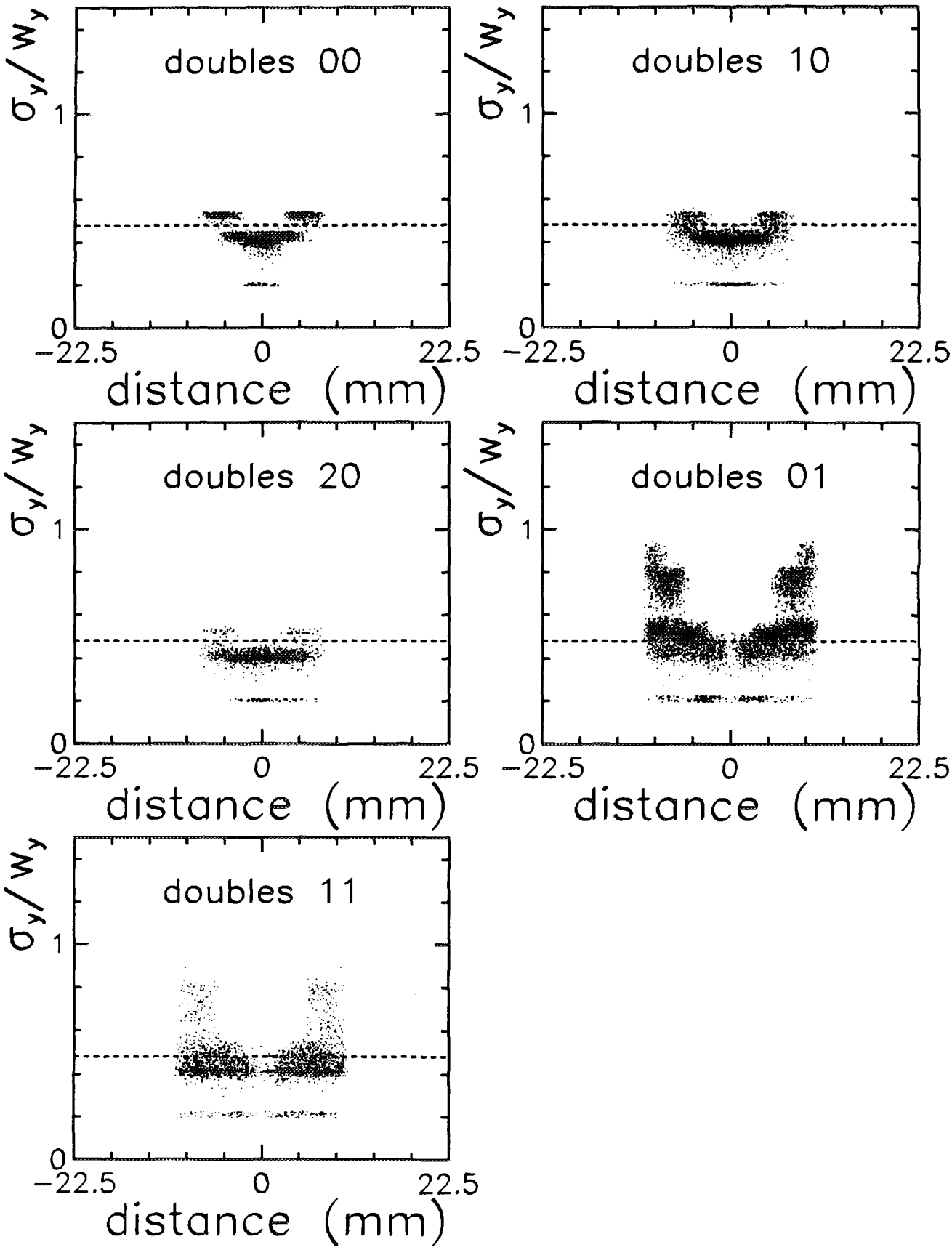

Figure 5.5: *Normalized standard deviations σ_y from the Gaussian algorithm as a function of the impact distance of double-hits in Y-direction. The dashed line marks the gate that was set on single hits. The localized structures display the discrete wire position. Double-hits can be clearly recognized when the impacts are 2 wires separated.*

which were set to avoid that single-hit get misidentified. A gate of 0.9 on the ratio 9/25 asures that 99.8% of the single-hits are above this condition (left top graph in fig. 5.7). Double-hits on the same pad are not recognized and also for double-hits on neighbouring pads the efficiency is not good. Only when the double-hits are already separated by 2 pads (20) the efficiency becomes large. For hits separated by less than 5 mm the method is not useful.

Recognition by charge ratios

The following graph corresponds to a double-hit recognition method that was already described by Yu [14]. Figure 5.8 shows the charge ratio of the right to the center Q_r/Q_c as a function for the left to the center Q_l/Q_c. This is in fact similar to the usage the the above discussed 2-pad algorithms and the charge ratio algorithm. For single-hits one sees a clear relation of the two charge ratios which depends on the position of the impact on the pad. It is very interesting to note that the width of this curve reflects the accuracy of the charge measurements and thus *directly the resolution of the detector without any external reference* like a microstrip detector. The shape of the curve depends of course on the chamber design, *i.e.* on d/w_x. Nevertheless for a given chamber lay-out the relation is fixed. Double-hits, sufficiently separated and not too different in amplitude, will destroy this relation. This can be seen on the other plots in the figure. By gating on the single-hit curve one has a possibility to separate double-hits. For hits with the same amplitude this is possible from a double-hit distance of about $0.4 * w_x$ [14], which would be in our case 2 mm. However the efficiency will suffer due to the possibility of very different amplitudes (Landau tails). The plot for double-hits on the same pad shows that this works only for a small part of the data, while for hits on neighbouring pads (10) the efficiency is much higher.

The data shown in fig. 5.8 for single hits can be fitted by

$$\frac{Q_r}{Q_c} = \frac{a}{\frac{Q_l}{Q_c} - a} + a \,, \qquad (5.1)$$

where a is found to be $a = 0.012$ in the standard lay-out. The function is shown in fig. 5.8 as a solid line. In the case of double-hits many events are clearly off the function. By projecting the events on the function it is easier to set a gate. This is shown in fig. 5.9. Hits on the right side of the dashed line are double-hits. The standard deviation from the functional behaviour is about 0.0126 in relative units (charge ratios of the side pad to the center pad) corresponding to a single-hit resolution of 43 μm achieved with the charge ratio algorithm.

In fig. 5.10 the same method is used in Y-direction. Charge ratios between the bottom and the center pad Q_b/Q_c as a function of the top and the center pad Q_t/Q_c are displayed. Now the wire structure is responsible for clean structures. For single-hits at 0° the wires show up at 3 points. The upper left point where the charge Q_b is large is from hits on the bottom wire. The opposite situation is given for the point on the right where the charge on the top wire Q_t is large. When the hit is on the middle wire then the charge on the top and bottom pad is at minumum and maximum for the center pad. This corresponds to the concentration near the origin. However the the situation where the impact is perpendicular to the chamber plane (X–Y) is a very special one. In the case an angle with the Y–Z plane appears the ionization charges may be shared by two neighbouring wires [5]. In that case the charge ratios will be inbetween the single wire points. But they will always be between neighbouring wires and not between the bottom and top wire as one can see in comparison with double-hits on the same pad (fig. 5.10). The dashed line can therefore work as a gate to separate single- from double-hits. This becomes especially efficient when the impacts are on neighbouring pads in Y-direction (01).

Efficiency

The efficiency to recognize double-hits with the standard lay-out and 0.5% noise is shown in figs. 5.11–5.13. The first graph (5.11) shows the efficiency as a function of the X-distance of the 2 impacts. Only double-hits that show up with one maximum in the cluster pattern are considered. When the two hits are on the same pad the efficiency is 50% when the 2 hits are separated by only 2 mm. When the distance is 3 mm or more the efficiency is over 98%. Double-hits identified with a distance closer than 1.5 mm

[5] We restrict ourselves to small angles and a narrow gas gap (= $2d$), therefore not more than 2 wires may be touched.

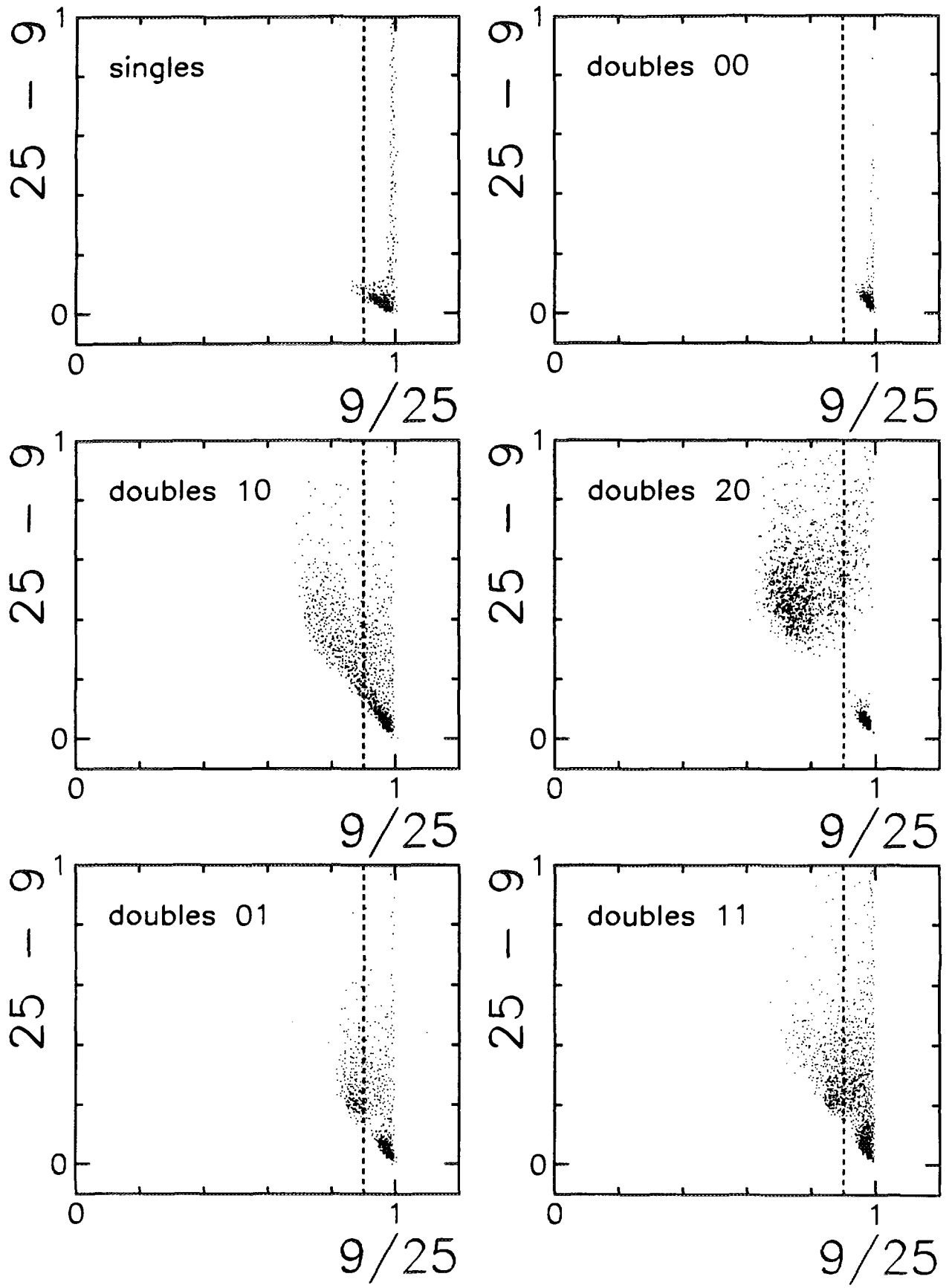

Figure 5.6: *Difference of induced charge between a cluster of 25 and 9 pads around the pad containing the charge maximum as a function of the charge ratio of the 2 clusters. For single-hits a clear structure is visible which is different for double-hits. The long vertical contribution comes from the long Landau tails. Even if the ratio is close to 1 the difference might be relatively large. The dashed line shows the actual gate which can be clearly improved to be more efficient.*

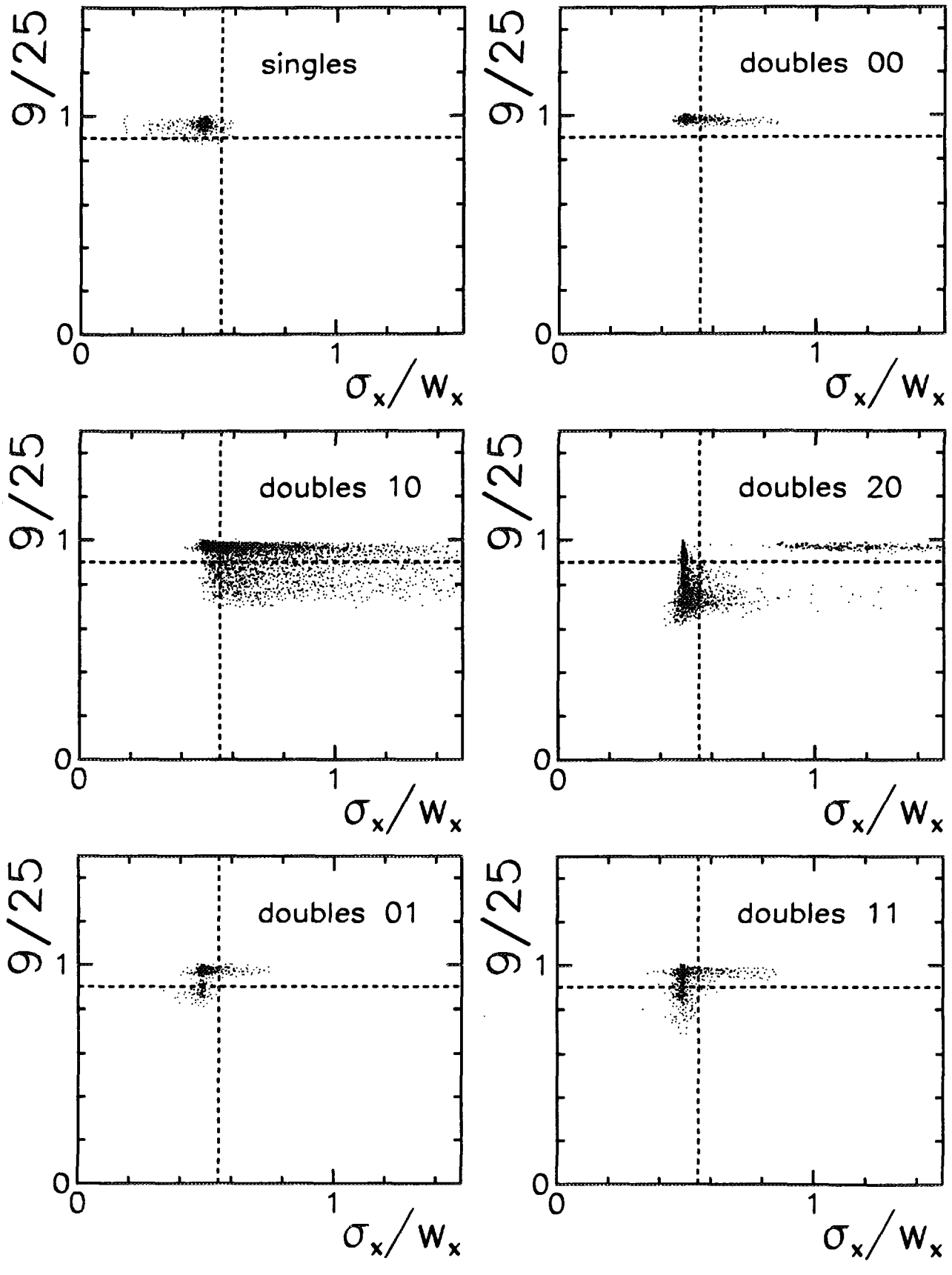

Figure 5.7: *'Cluster size' (9/25) as a function of normalized Gaussian standard deviation $\sigma_g y$. Dashed lines indicate the gates set to separate single- from double-hits. The methods becomes only efficient when the 2 impacts are at least on different pads.*

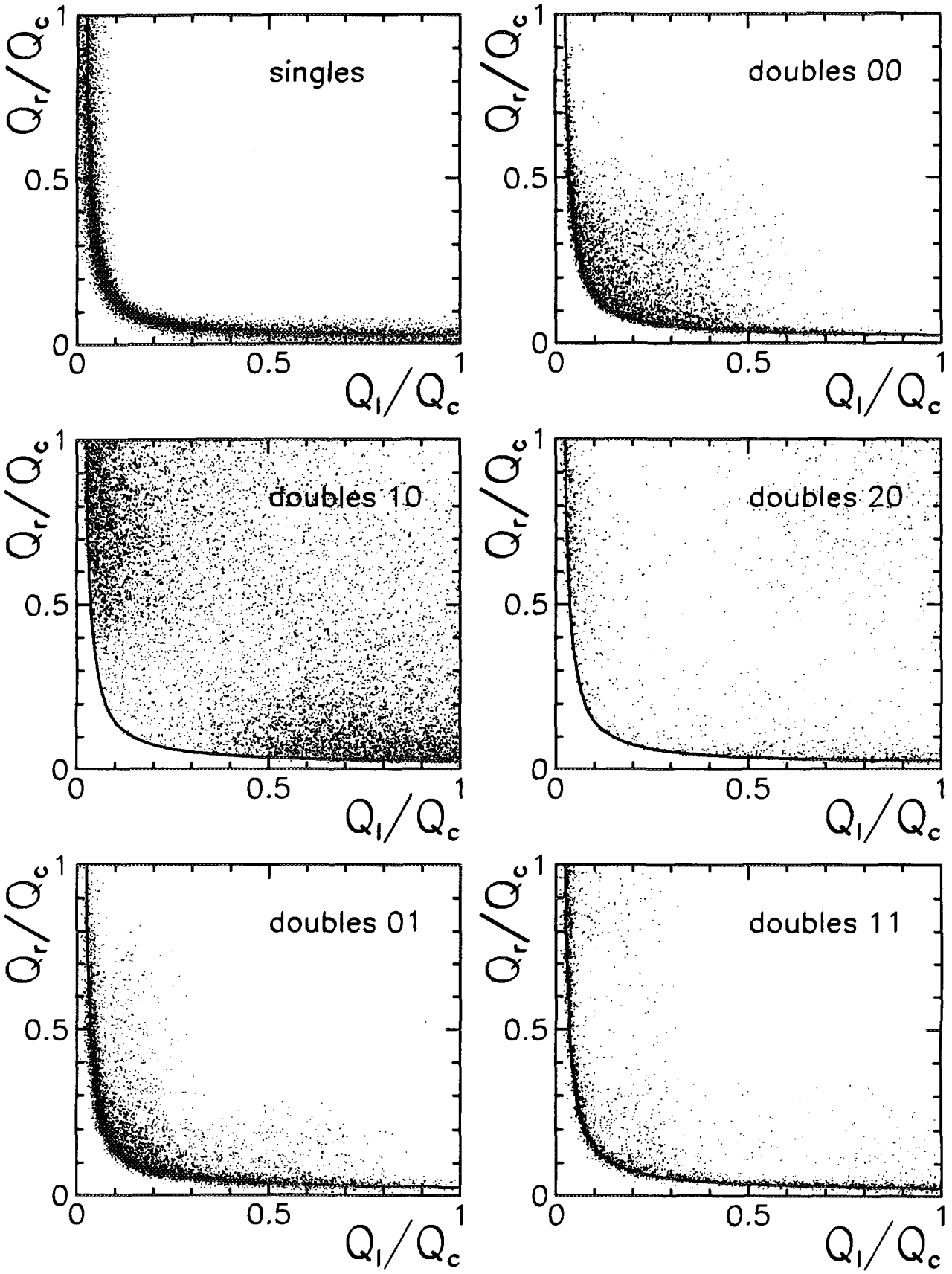

Figure 5.8: *Plot for charge ratios of right to center as a function of the left to center pad (X-coordinate). For single-hits this plot has a proper functional behaviour which is displayed in the graphs as a solid line (see eq. 5.1). The width of the particle distribution around this line is a direct measure of the single-hit resolution. All events above this band are double-hits. The separation achieved is also of the order of 2-3 mm.*

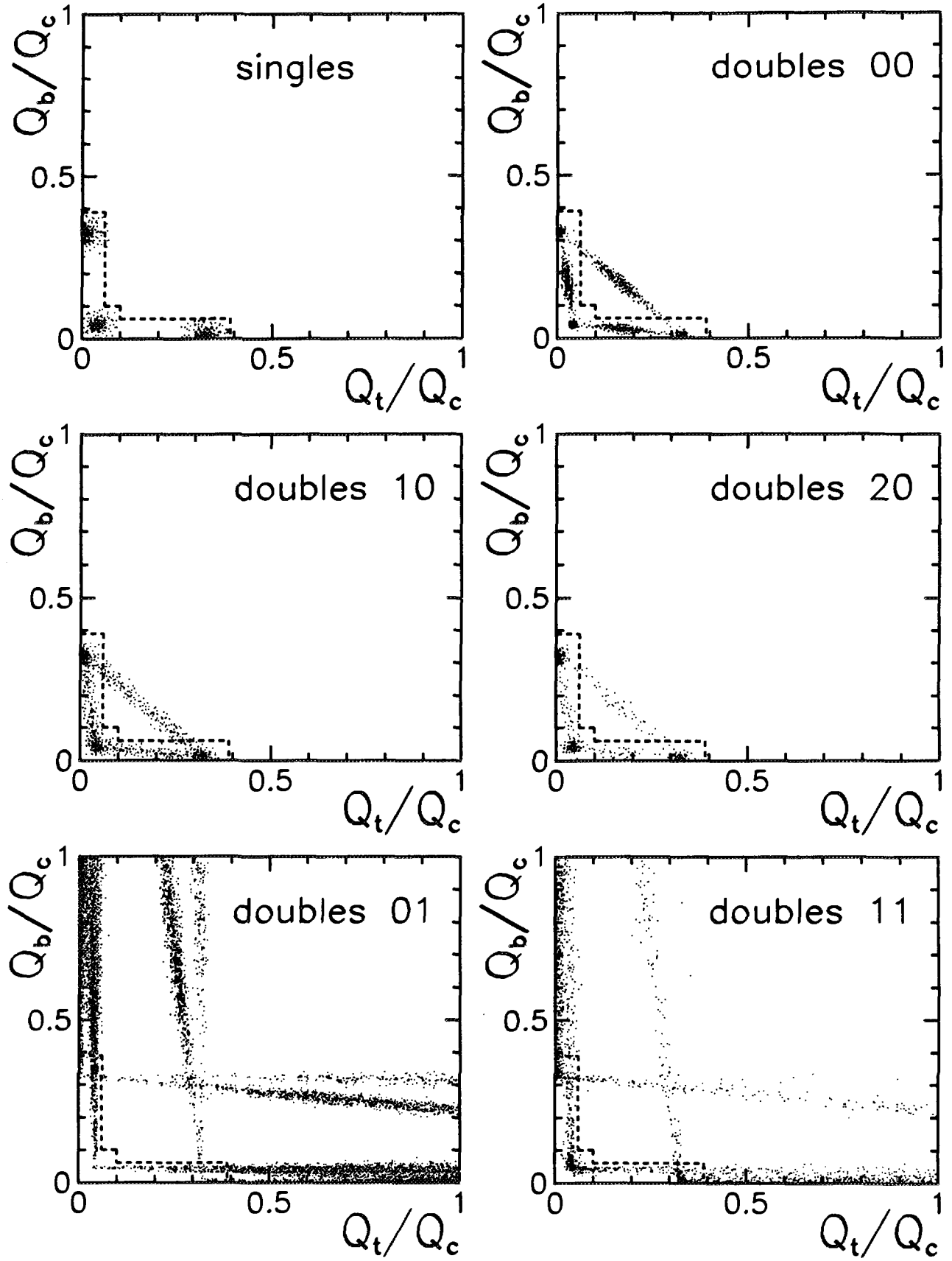

Figure 5.10: *Plot for charge ratios of the bottom to center as a function of top to center pad. The localized accumulations of events in the single-hit plot reflect the wire structure. The center wire position is near the origin. Events between the top or bottom wire and the center wire can appear if the track is inclined. But events between the top and the bottom wire can only come from double-hits (at least for angles < 30°). The dashed lines mark therefore the gate on single-hits. This method is very efficient if the vertical separation is more than one wire.*

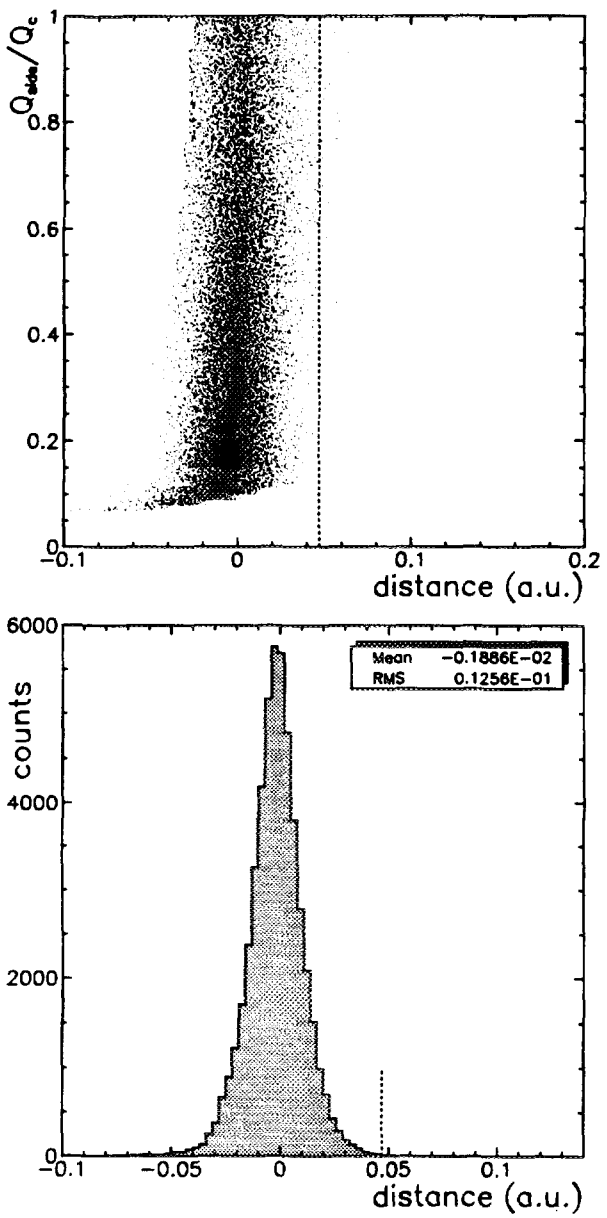

Figure 5.9: *Top: Plot of the linearized $Q_r/Q_c - Q_l/Q_c$ behaviour (see eq. 5.1). The structure for Q_{side}/Q_c near 0.15 is an effect of the gating. All events above a distance of 0.048 (dashed line) are identified as double-hits with a separation of more than $0.4 * w_x$ which is 2 mm in our case. Bottom: Projection on the X-axis. The standard deviation is about $\sigma_d = 0.0126$ corresponding to 43 μm resolution with the charge ratio algorithm.*

(about 20% efficiency) benefit of a sufficient distance in Y-direction, mainly events that are separated by 2 wires.

The situation is similar for impacts on 2 neighbouring pads (10), though the rise to over 98% efficiency is slightly lower. For double-hits separated by 2 pads in X (20) the efficiency is decreasing for larger distances. Above 10 mm distance between the impacts the statistics is very low, only very few double-hits have still only one maximum in the cluster pattern. Nevertheless there remains a problem due to the usage of algorithms for double-hits on different pads.

The efficiency to recognize double-hits on neighbouring pads in Y-direction (01) is rather high and of course almost constant for the X-coordinate. The large efficiency is due to the wire structure. For the (11) pattern the efficiency is not as good as expected from (10) and (01). Here the algorithm method has to be improved. It is surprising that the efficiency is decreasing for larger distances.

Taking finally together all efficiencies for local pad situations one gets the last graph in fig. 5.11 for the efficiencies as a function of the impact distance in X-direction. Remember that only double-hits giving one maximum are included in the graph. For distances less than 3 mm the efficiency is about 70%. For larger distances it is always more than 95%. The decreasing efficiency for large distances is statistically negligible and is due to imperfections of the algorithms. For distances of more than 10 mm only double-hits with very different amplitudes can still give only one maximum in the cluster pattern.

The efficiency as a function of the Y-coordinate is shown in fig. 5.12. It can be clearly seen that the efficiency increases to almost 100% when the distance in Y is more than 5 mm or 2 wires. The total efficiency of course very similar to the X-coordibate.

The next plot 5.13 shows the efficiency as a function of the distance $r = \sqrt{x^2 + y^2}$ of the 2 impacts. When the distance is more than 6 mm the efficiency is above 95%. It is clear that especially for the (11) pattern situation the method must be improved.

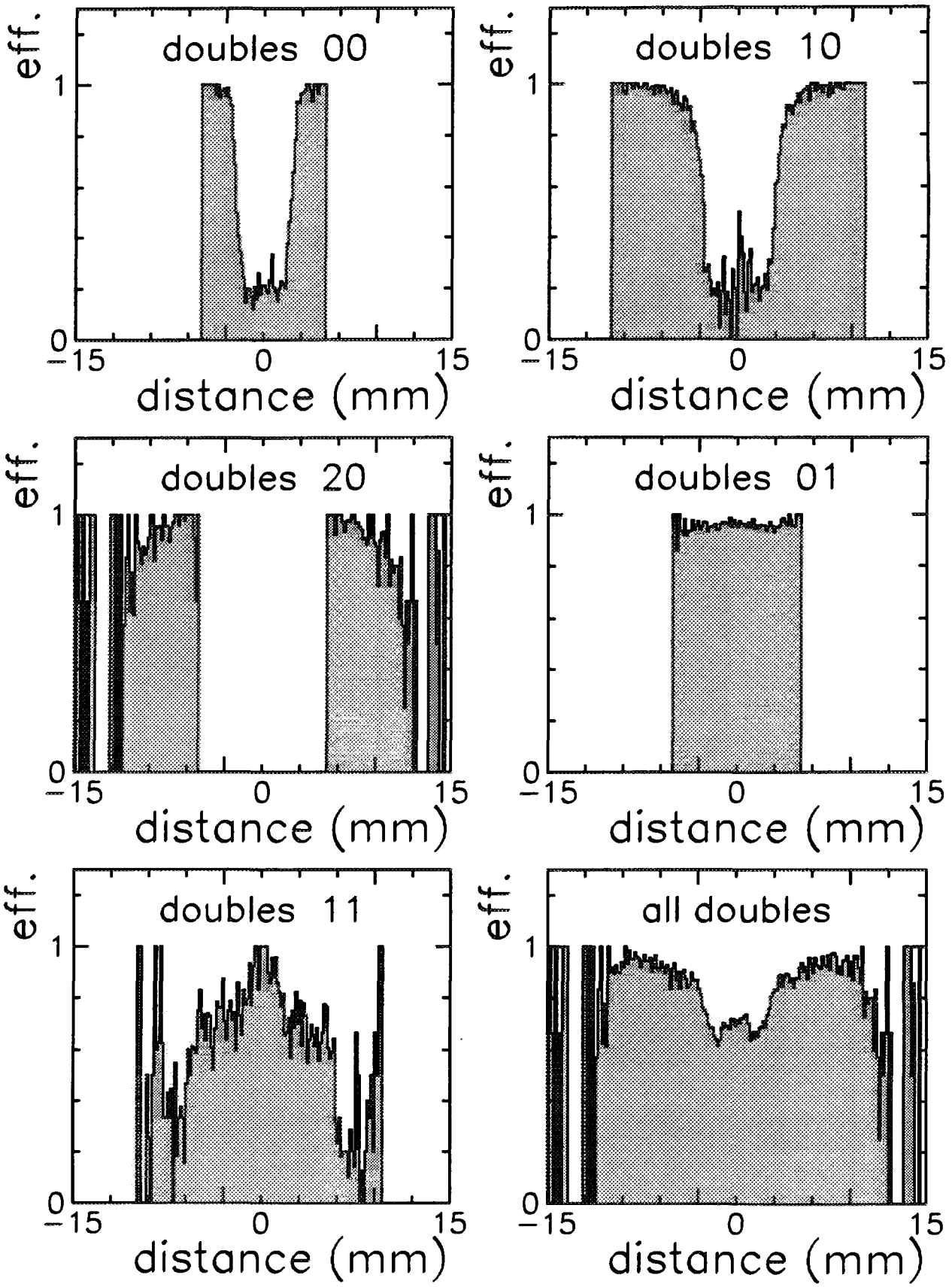

Figure 5.11: *Efficiency of double-hit recognition with algorithms as a function of the impact distance in X-direction. Only double-hits that show up with a single maximum are considered in the graphs. The different pad constellations were triggered during the event generation and would be unknown in experimental data. The last graph shows the efficiency for all double-hits. See text.*

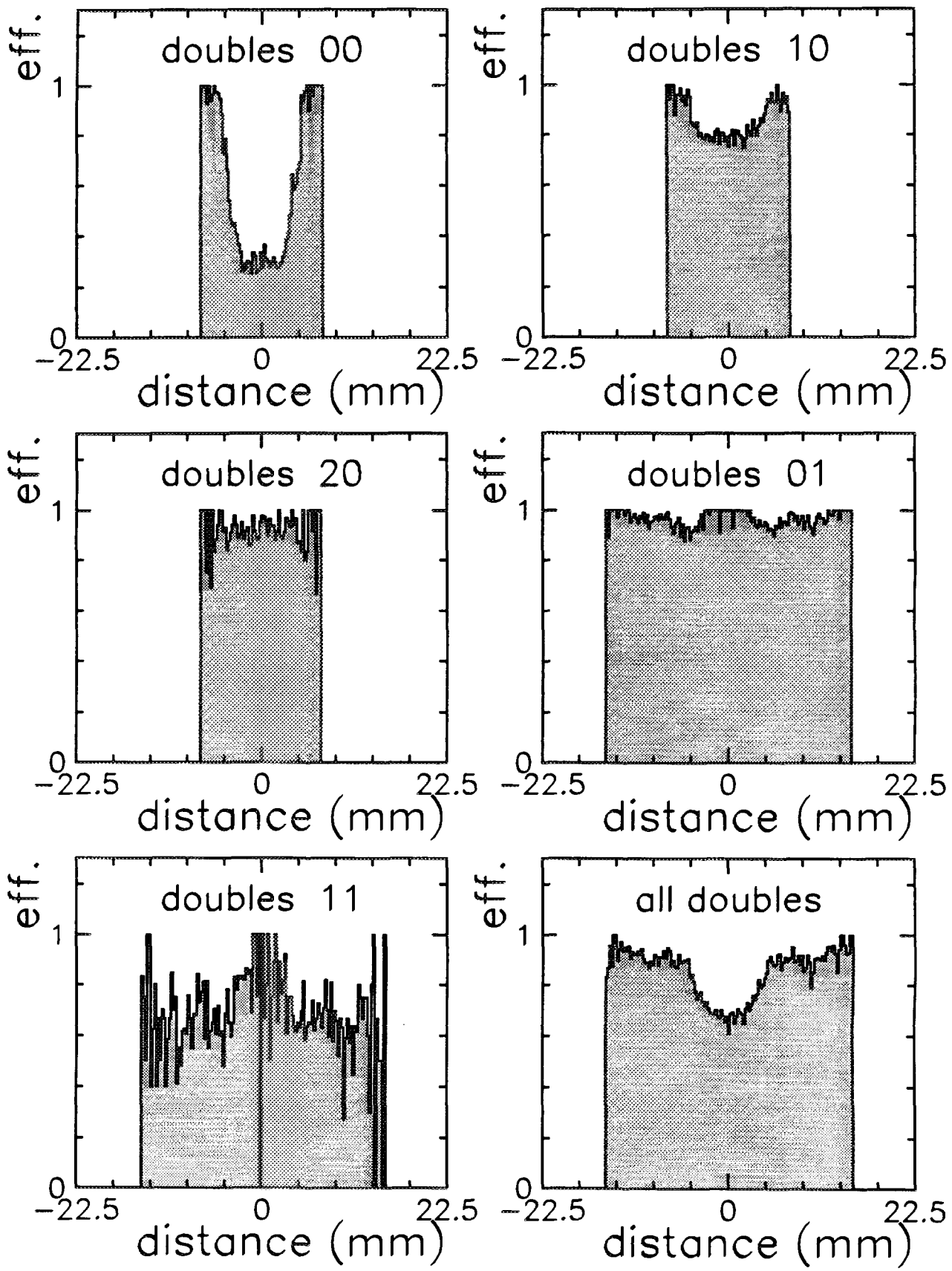

Figure 5.12: *Efficiency of double-hit recognition with algorithms as a function of the impact distance in Y-direction. Only double-hits that show up with a single maximum are considered in the graphs. The different pad constellations were triggered during the event generation and would be unknown in experimental data. The last graph shows the efficiency for all double-hits. See text.*

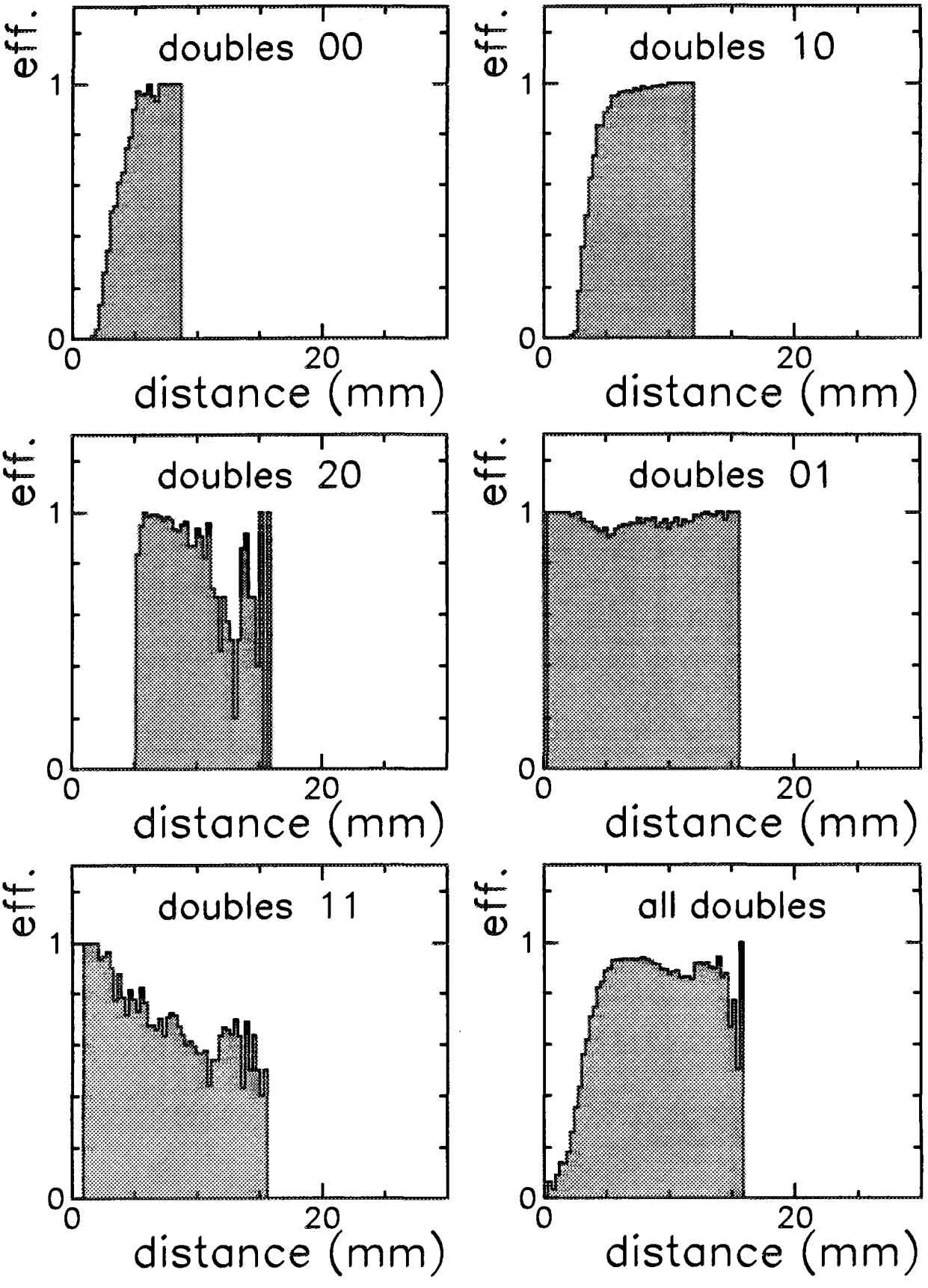

Figure 5.13: *Efficiency of double-hit recognition with algorithms as a function of the impact distance* $r = \sqrt{x^2 + y^2}$. *Only double-hits that show up with a single maximum are considered in the graphs. The different pad constellations were triggered during the event generation and would be unknown in experimental data. The last graph shows the efficiency for all double-hits. See text.*

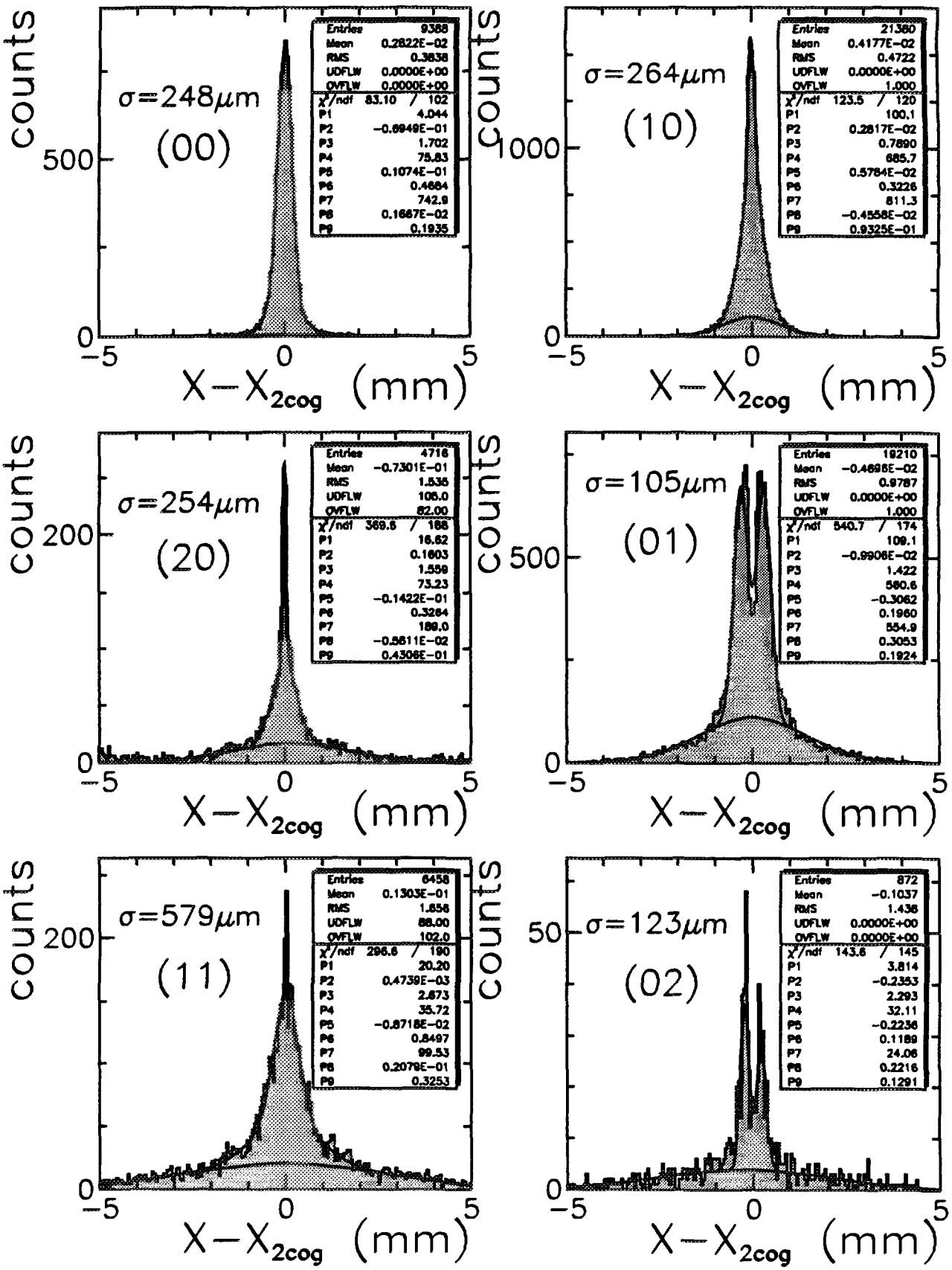

Figure 5.14: *Residuals for double-hits with one maximum in the hit pattern in dependence of the hit pattern (00, 10, etc.). The fits shown are 3 added Gaussians with parameters P1–P9 printed on the right hand side. The resolution σ quoted on the left side on each plot is the weighted mean of the to narrower Gaussians. The 3rd Gaussians is also displayed as solid line. The resolution for these events is too bad. They must by considered as lost (0 efficiency) or as background.*

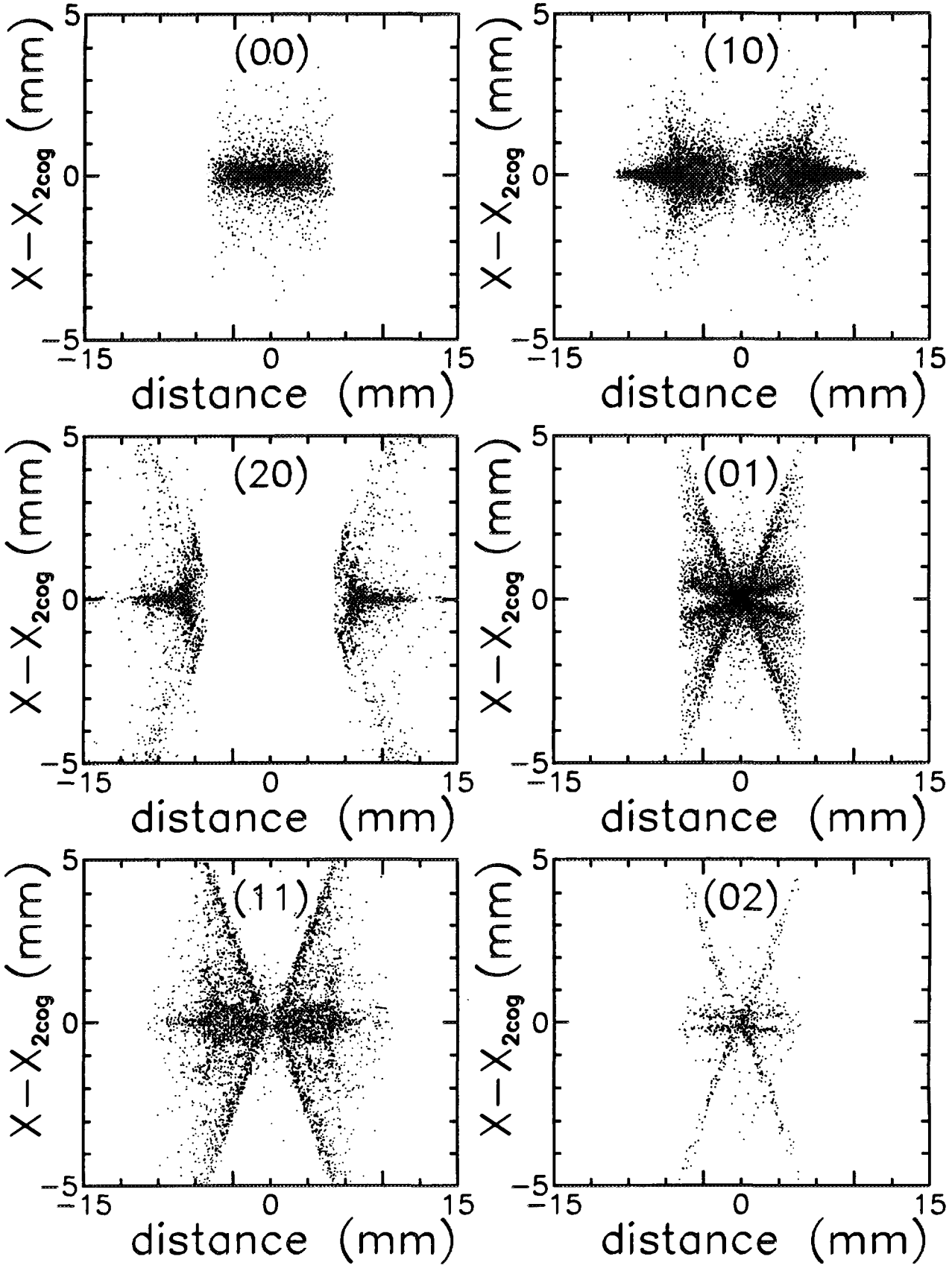

Figure 5.15: *The same data as in fig. 5.14 plotted as a function of the impact distance in X-direction. The systematic deviations are discussed in the text.*

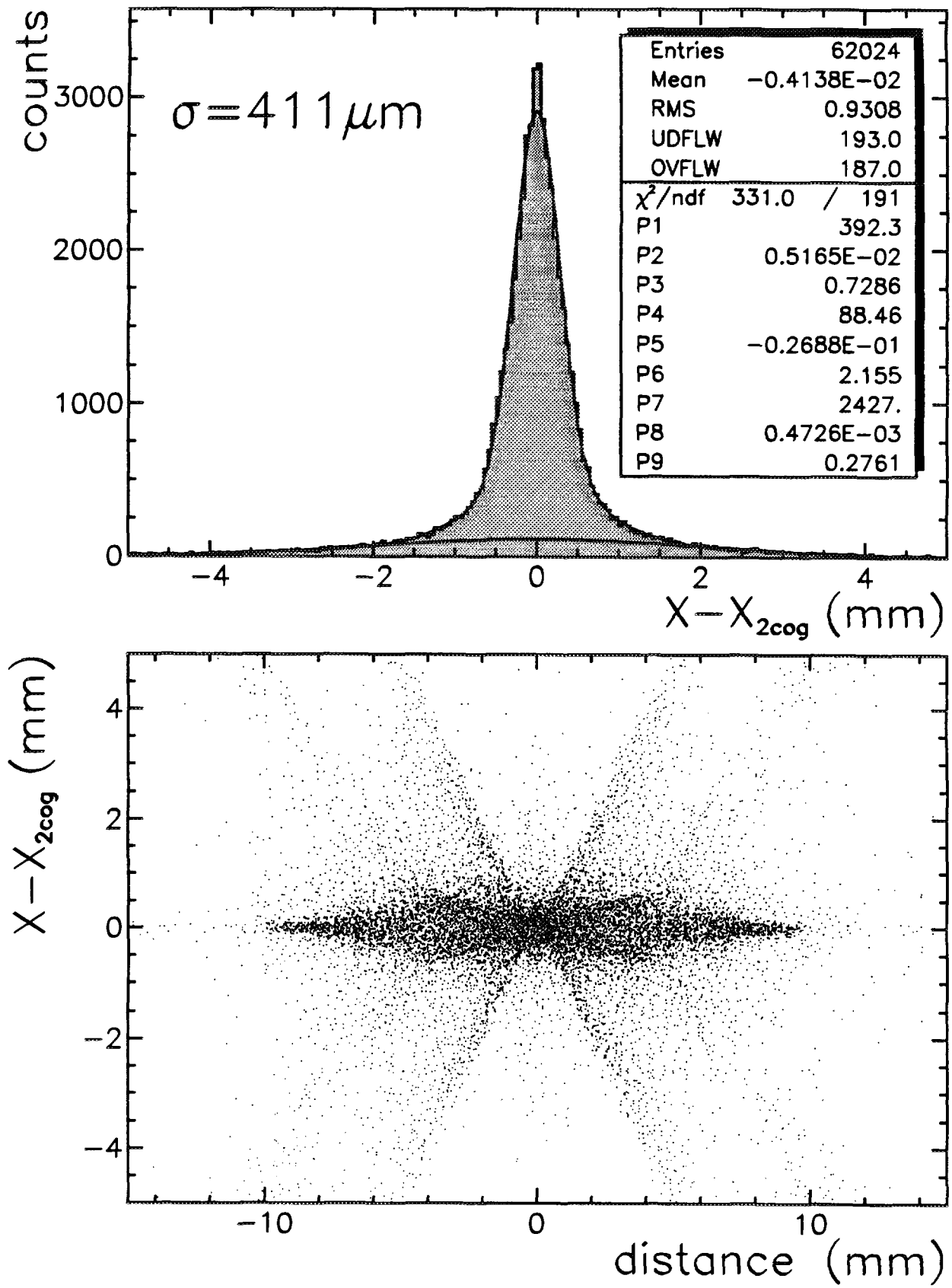

Figure 5.16: *Global resolution for all double-hits with one maximum in the hit pattern (compare with fig 5.14). The fit is as described above. The bottom graph reveals the systematic deviations as a function of the impact distance in X-direction.*

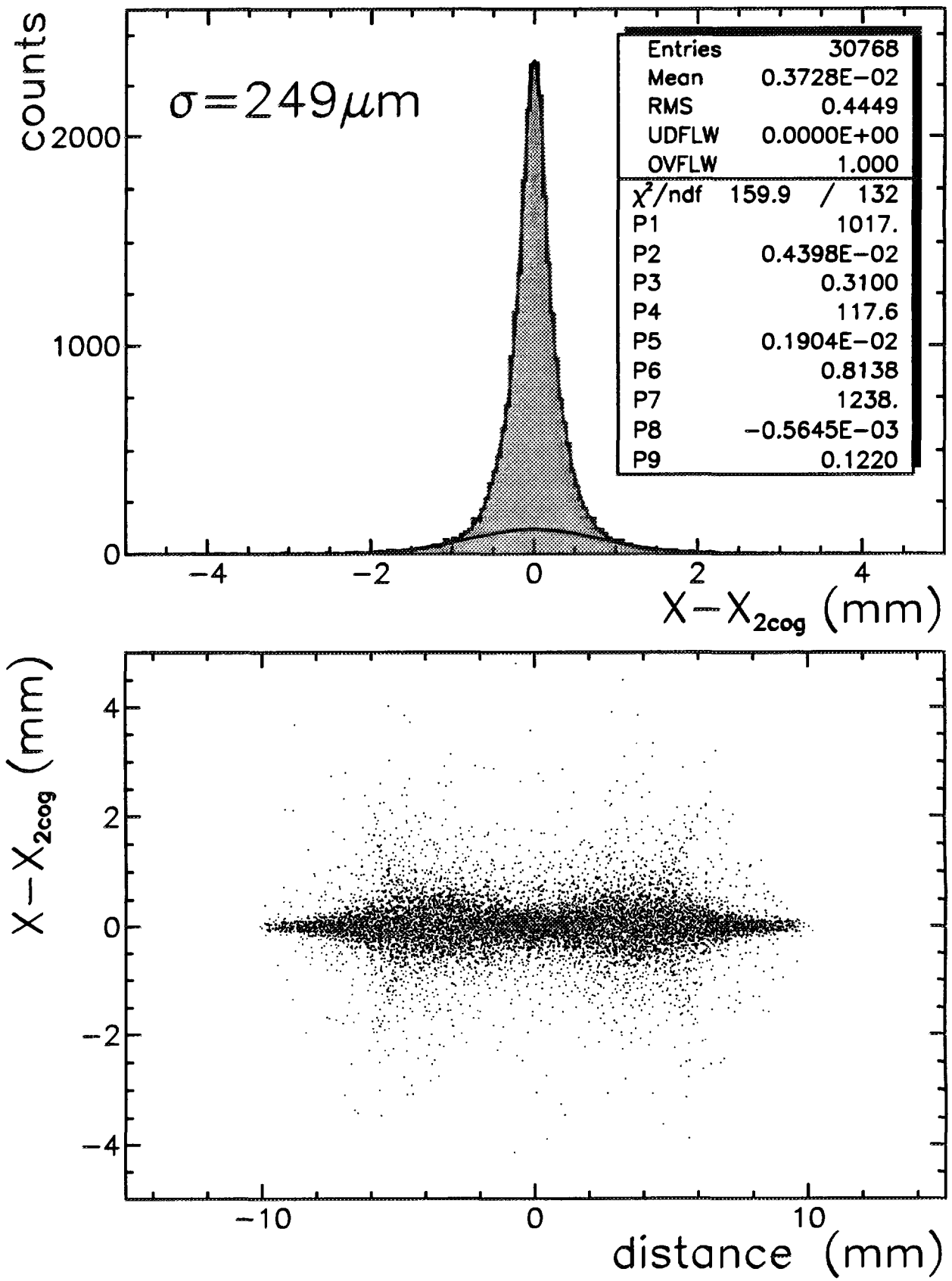

Figure 5.17: *Resolution for all double-hits with 00 and 01 hit pattern. There is much less background contribution and the resolution is reasonable. But there remain systematic deviations (see text).*

5.3 Separation by fit

Resolution

In figs. 5.14–5.17 *first* results of the resolution using the 2-pad ratio like algorithm are shown. The graphs in fig. 5.14 show the resolutions fitted by 3 Gaussians for the following pad situations: 00, 10, 20, 01, 11 and 02. The mean σ of the residuals is a weighted mean of the 2 narrower Gaussians. The 3rd Gaussian not taken into account is superimposed. These contributions are too large and must be regarded as lost.

For double-hits on the same pad the position reconstruction with the 2-pad algorithms gives a resolution $\sigma_{00} = 248\mu$m. for each hit. For hits on neighboured pads (10) the resolution is already worse, $\sigma_{10} = 264\mu$m. Comparing with the plots on fig. 5.15 reveals that there are still systematic deviations in regard on the distance between the 2 impacts especially for 10. These are due to the pattern structure in combination with the 2-pad algorithm. Further corrections are necessary. The resolution becomes even worse for the 20, 01, 11 and 02 situations. These contributions are statistically less significant, but they still will give an important background.

However for the structures like 01, 11 or 02 a much better resolution on the X-coordinate can be achieved using normal 3-pad algorithms. But to use them one has to provide the pattern structure.

The graphs on figs. 5.16 and 5.17 combine all pattern situations shown in 5.14 and 5.15. The first figure shows the combination of all double-hits giving only one maximum. The overall resolution for the peak is $\sigma_{all} = 376\mu$m with a broad background. The below graph shows the systematic deviations as a function of the impact distance in X-direction.

Most of the broad background is coming from 20, 01, 11 and 02 patterns as one can see on fig. 5.17 where only 00 and 10 are taken into account. The resolution is now $\sigma_{00+10} = 306\mu$m with a low contribution from a broad 3rd Gaussian shown as the solid curve. Nevertheless this result might be improved somewhat be correcting systematics.

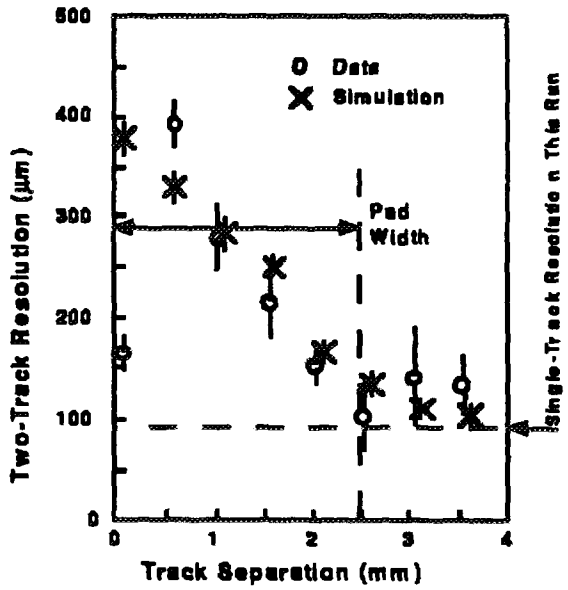

Figure 5.18: *Comparison of position resolution predicted and observed in events having two nearby tracks. The deconvolution is made by fitting the Mathieson charge distribution to the data. Single-track resolution in this particular run was 80 μm. From Fenker* et al. *[16].*

Fenker *et al.* [16] simulated and measured the resolution degradation as a function of the distance of the two impact points. Their result is shown in fig. 5.18. The resolution for single hits was 80 μm in that experiment. The resolution became about a factor of 5 times worse if the tracks were rather close together and was slowly decreasing to the single hit resolution when the distance increased to more than 1 strip width. For very close hits (less than 500 μm) the double-track resolution becomes suddenly much better (only about 160 μm), which is in fact trivial because the tracks are less separated than the double-hit resolution itself and could therefore be treated *like* a single hit. The mean value would then still give a much better σ as the 400μm before. This simple effect was not reproduced with their Monte Carlo due to some double counting of noise [6] [16]. Nevertheless the result will be strongly geometry dependent. Of course narrow charge distributions (small anode–cathode pitch) and high pad granularity will

[6] Single experimental events were superimposed instead of generated events, each having its own noise contribution. This is not true for events which are on the same pad, i.e. very close to each other.

give the best results. In [16] the anode–cathode pitch was 2 mm and the strip width 2.5 mm, far different from the standard lay-out chosen in this report. The double-hit resolution would therefore be expected to be worse.

Other work was done by Gratchev *et al.* [42] with the same CSC as reported in [24]. The readout pitch of that chamber was 5 mm wich is the same as width in X-direction in our standard design. They fitted the charges induced on the pads by the integrals of the Mathieson formula (see eqn. 2.10 and 2.11). The identification of double-hits is also done by comparing a fit with single-hit hypothesis and a fit with double-hit hypothesis. Their results as a function of the impact distance of the 2 hits are shown in fig. 5.19. At a distance of 2 mm the efficiency is still more than 80%. The resolution is degraded from 50 to 500 μm as soon as the 2 impacts are at a distance of less than one readout pitch.

5.4 Discussion

We showed that double-hits can be separated to some extend. Double-hits with a distance of less than one pad remain a problem due to unresolveable ambiguities. The necessary CPC lay-out for the ALICE experiment might finally be dominated by the double-hit separation power of the chambers. This demands reflections of what effeciency is necessary for the double-hit resolution. Detailed studies with events coming from GEANT are necessary.

Nevertheless one should keep in mind that the probability of double-hits on the same pad is *much* smaller than for partly overlapping clusters with size 3×3 pads which can be treated. So the efficiency is perhaps much better as it seems at first sight.

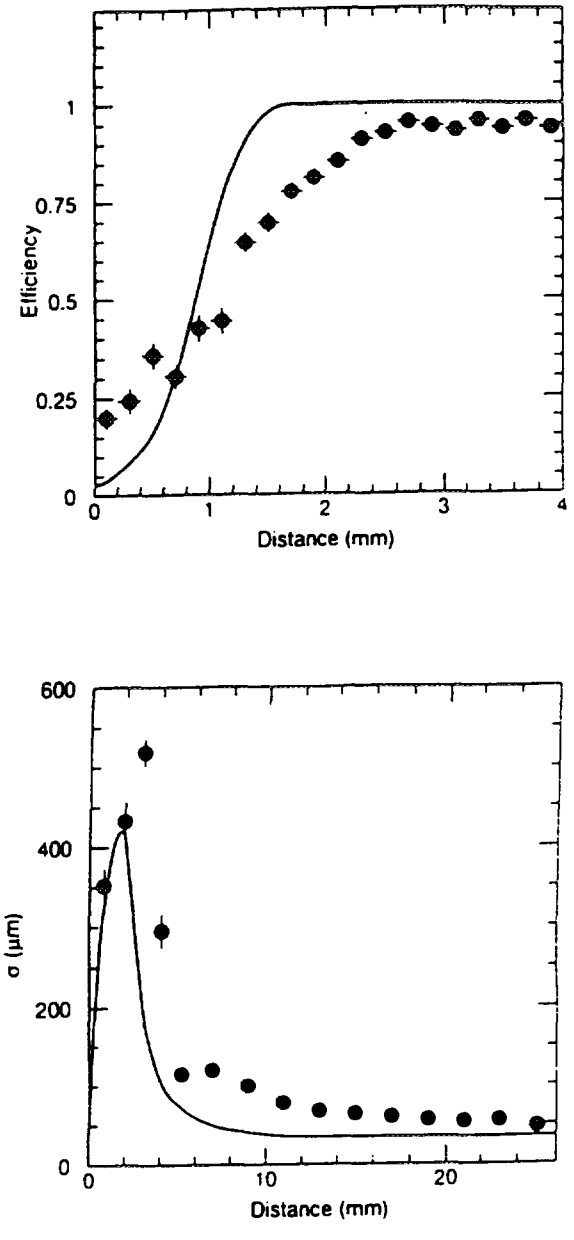

Figure 5.19: *Double-hit treatment by a fit procedure by Gratchev* et al. *in a CSC with 5 mm readout pitch. Top: Efficiency of double-hit reconstruction vs. their distance. The solid line shows simulation results and the points are experimental data. Bottom: Position resolution vs. distance.*

Chapter 6

Cathode Pad Chambers for Di-Muon tracking in the ALICE detector

6.1 Introduction

The Di-Muon Arm of the ALICE detector at LHC aims at the detection of muon pairs from the decay of J/Ψ and Υ mesons (see chapter 1). In the addendum to the ALICE letter of intent [2] the first GEANT simulations showed that about 200 charged particles are expected per central Pb–Pb collision on the first tracking chamber after the absorber (see fig. 1.1). These particles will arrive practically at the same time on the chamber plane [1] and have to be analysed in parallel. The spatial particle distribution in the chamber plane will be far from uniform. A concentration of events shows up for small angles, *i.e.* around the beam pipe. Nevertheless the simulation and optimization of the absorber is not yet finished and more refined studies show now that one should expect about 300 particles per central Pb–Pb collision. Of course GEANT can only estimate the number of charged events within a certain precision. For security one should design the tracking chambers to work still properly with a 2–3 times higher particle rate. Therefore the Di-Muon collaboration demanded to optimize the chamber design for $\approx$ 900 charged particles with $\sigma_x \leq 100\mu$m for all particles and a detection efficiency of over 95% [43]. The resolution determination must contain the treatment of double-hits. The single-hit resolution would of course be better.

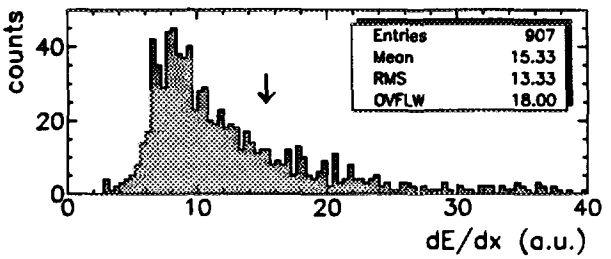

Figure 6.1: *Energy loss distribution with Landau shape generated by GEANT. The noise amplitude of 0.5% refers to the mean energy loss marked by the arrow.*

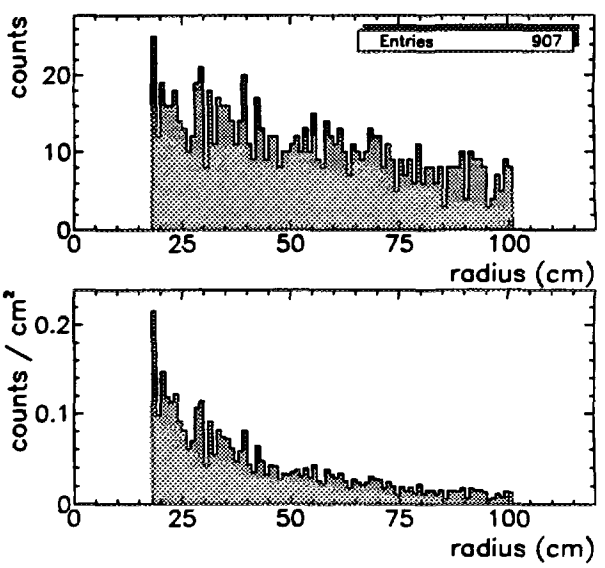

Figure 6.2: *Spatial hit distribution in the first tracking chamber plane generated by GEANT. Top: hit distribution as a function of the radius. Bottom: hit density per cm². With a pad size of* $5 * 7.5 = 3.75$ *mm² the maximum pad occupancy is about 6 %.*

[1] In the actual design the first chamber will have a surface of about 2.6 m².

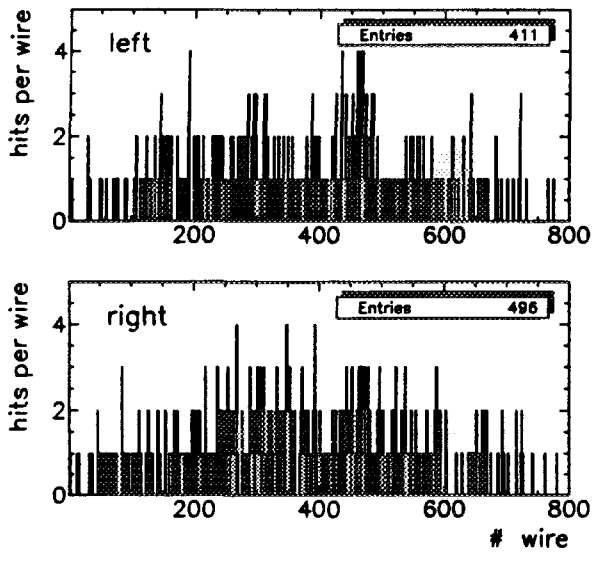

Figure 6.3: *Wire occupancy in the first tracking chamber for one central Pb–Pb collision generated by GEANT. 1 channel per wire. The chamber will be halfed in two parts (left and right) for technical reasons.*

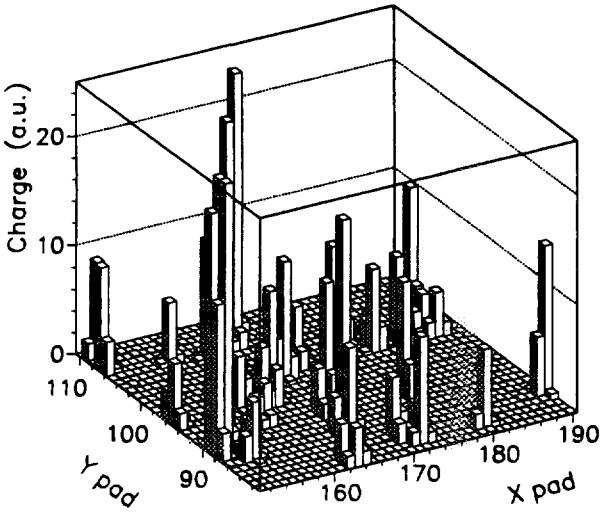

Figure 6.5: *Induced charges on the pad with noise after pedestal subtraction. Only a small part of the chamber is shown (see fig. 6.4).*

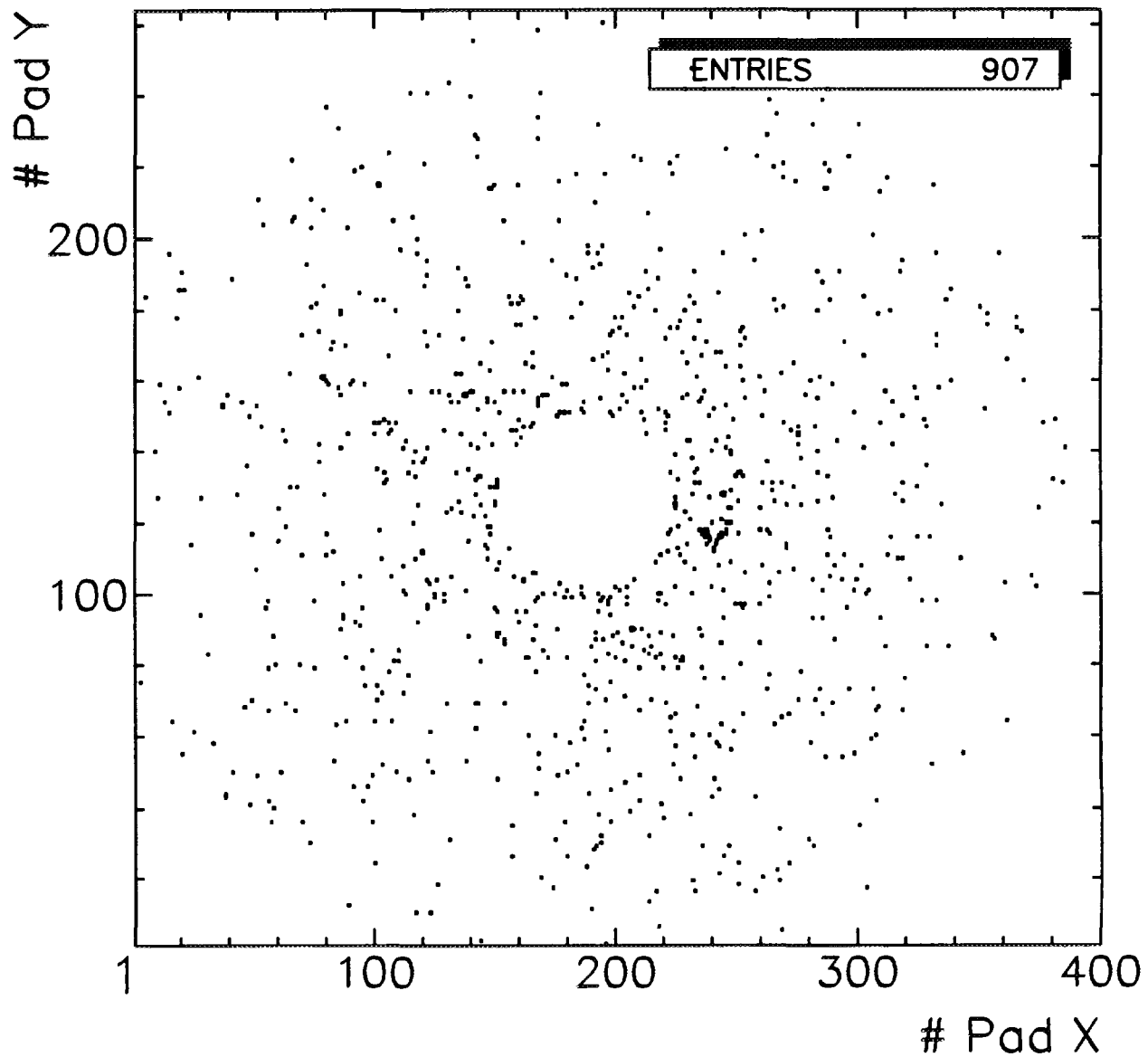

Figure 6.4: *Hit pattern (1 channel per pad) in the first tracking chamber for one central Pb–Pb collision generated by GEANT. The pad size is* $5 * 7.5\ mm^2$. *The inner empty zone is around the beam pipe.*

Chapter 7

Conclusions

We draw here conclusions on the usage of CPC's in general and for the ALICE experiment. We try to list the work which needs to be done to define the final lay-out for the Di-Muon Arm in the ALICE experiment.

7.1 Summary on Cathode Strip/Pad Chambers

7.2 Cathode Pad Chambers for ALICE

Chapter 8

Acknowledgements

Somebody is greatly acknowledged for comments on the text. M. Benayoun, A. Diazeck, H. Fenker, J. Guillot, H.-Å. Gustafsson, K. Lau, P. Leruste, J.L. Narjoux, M. Sené, R. Sené, S. Szafran, A. Volte and A. Willis are thanked for discussions and supplying us with helpful informations.

All further comments or questions on this report are greatly encouraged and welcome. Please send them to

Ralf Wurzinger
E-Mail: wurzinge@ipnosb.in2p3.fr

or

Yves Le Bornec
E-Mail: lebornec@ipnosb.in2p3.fr

Appendix A

Appendix

A.1 Gaussian algorithm for 3 strips

In references [28, 44, 30] formula are given to find the impact position by assuming the charge distribution to have the form of a Gaussian. We show here how the formula is derived. While Endo *et al.* [28] found a resolution worse than with the COG algorithm, Lau *et al.* [30] found a resolution very close to the ratio algorithm with their chamber geometry.

Q_l, Q_c and Q_r are the measured charges on 3 consecutive strips or pads. The middle pad has its center at position $X_c = 0$. The two others are at $X_l = -w_x$ and $X_r = +w_x$ with w_x the strip width. From the Gaussian

$$Q_i = ae^{-(X_i - X_0)^2/\sigma_g^2} \tag{A.1}$$

with a being the amplitude, X_0 the mean and $i = l, c, r$, one gets 3 equations from the 3 strips to find the 3 unknown parameters a, X_0 and σ_g

$$Q_l = ae^{-(w_x+X_0)^2/\sigma_g^2} \tag{A.2}$$
$$Q_c = ae^{-X_0^2/\sigma_g^2} \tag{A.3}$$
$$Q_r = ae^{-(w_x-X_0)^2/\sigma_g^2}\,. \tag{A.4}$$

Taking equation A.3 one can express a and $\ln a$

$$a = \frac{Q_c}{e^{-X_0^2/\sigma_g^2}} \tag{A.5}$$
$$\Rightarrow \quad \ln a = \ln Q_c + X_0^2/\sigma_g^2\,. \tag{A.6}$$

Equations A.2 and A.3 can be combined to eliminate σ_g.

$$\ln\frac{Q_l}{a} = -\frac{(w_x+X_0)^2}{\sigma_g^2} \tag{A.7}$$
$$\Rightarrow \quad \sigma_g^2 = \frac{(w_x+X_0)^2}{\ln\frac{a}{Q_l}} \tag{A.8}$$
$$\text{and} \quad \ln\frac{Q_r}{a} = -\frac{(w_x-X_0)^2}{\sigma_g^2} \tag{A.9}$$
$$\Rightarrow \quad \sigma_g^2 = \frac{(w_x-X_0)^2}{\ln\frac{a}{Q_r}}\,. \tag{A.10}$$

Inserting $\ln a$ from eq. A.6 one finds for eq. A.8

$$\sigma_g^2 = \frac{(w_x+X_0)^2}{\ln\frac{Q_c}{Q_l} + \frac{X_0^2}{\sigma_g^2}} \tag{A.11}$$
$$\Rightarrow \quad \sigma_g^2 \ln\frac{Q_c}{Q_l} + X_0^2 = (w_x+X_0)^2 \tag{A.12}$$
$$\Rightarrow \quad \sigma_g^2 = \frac{w_x^2 + 2w_xX_0}{\ln\frac{Q_c}{Q_l}} \tag{A.13}$$

and similar from eq. A.10 follows

$$\sigma_g^2 = \frac{w_x^2 - 2w_xX_0}{\ln\frac{Q_c}{Q_r}}\,. \tag{A.14}$$

Combining the right hand sides of eqn. A.13 and A.14 leads to

$$\frac{w_x^2 + 2w_xX_0}{\ln\frac{Q_c}{Q_l}} = \frac{w_x^2 - 2w_xX_0}{\ln\frac{Q_c}{Q_r}} \tag{A.15}$$
$$\Rightarrow \quad w_x\ln\frac{Q_c}{Q_r} + 2X_0\ln\frac{Q_c}{Q_r} = w_x\ln\frac{Q_c}{Q_l} - 2X_0\ln\frac{Q_c}{Q_l} \tag{A.16}$$
$$\Rightarrow \quad X_0(\ln\frac{Q_c}{Q_r} + \ln\frac{Q_c}{Q_l}) = \frac{w_x}{2}(\ln\frac{Q_c}{Q_r} - \ln\frac{Q_c}{Q_l})\,. \tag{A.17}$$

This gives finally the mean position X_0

$$X_0 = \frac{w_x}{2}\,\frac{\ln Q_l - \ln Q_r}{2\ln Q_c - \ln Q_r - \ln Q_l} \tag{A.18}$$

in agreement with [28, 30]. For testing clusters if they are single or double-hits the calculation of the induced charge's σ_g might be important. Inserting eq. A.18 in A.13 gives

$$\sigma_g^2 = \frac{w_x^2(1 + \frac{\ln Q_r - \ln Q_l}{2\ln Q_c - \ln Q_r - \ln Q_l})}{\ln\frac{Q_c}{Q_l}}\,, \tag{A.19}$$

which can be reduced to

$$\sigma_g = \frac{w_x}{\sqrt{\ln Q_c - (\ln Q_r - \ln Q_l)/2}} \tag{A.20}$$

A.2 Hyperbolic Secant Squared (SECHS) algorithm for 3 strips

Lau *et al.* [30] found the best resolution with their chamber geometry with the hyperbolic secant squared (SECHS) algorithm for 3 strips. It is in fact a very close approximation to the induced charge distribution used in [30]. In addition the algorithm seems to be much less sensitive to the incident angle of the track and as well on mechanical tolerances as *e.g.* the ratio algorithm. As we use the Mathieson formula for the charge distribution [11] one would even expect a somewhat better resolution using an algorithm using his formula. But anyway the two models are not very different. It is shown here how the formula is derived.

Q_l, Q_c and Q_r are the measured charges on 3 consecutive strips or pads. The middle (Q_c)pad has its center at position $X_c = 0$. The two others are at $X_l = -w_x$ and $X_r = +w_x$ with w_x the strip width. The hyperbolic secant squared function is [30]

$$Q_i = \frac{a_1}{\cosh^2(\pi(X_i - X_0)/a_2)}, \qquad (A.21)$$

with a_1 being the amplitude, X_0 the mean and $i = l, c, r$. One gets 3 equations from the 3 strips to find the 3 unknown parameters a_1, X_0 and a_2

$$Q_l = \frac{a_1}{\cosh^2(\pi(w_x + X_0)/a_2)} \qquad (A.22)$$

$$Q_c = \frac{a_1}{\cosh^2(\pi X_0/a_2)} \qquad (A.23)$$

$$Q_r = \frac{a_1}{\cosh^2(\pi(w_x - X_0)/a_2)}. \qquad (A.24)$$

Dividing equations A.22 and A.24 by the one for the central pad (A.23) one obtains

$$\frac{Q_c}{Q_l} = \frac{\cosh^2(\pi(w_x + X_0)/a_2)}{\cosh^2(\pi X_0/a_2)} \qquad (A.25)$$

and

$$\frac{Q_c}{Q_r} = \frac{\cosh^2(\pi(w_x - X_0)/a_2)}{\cosh^2(\pi X_0/a_2)}. \qquad (A.26)$$

Taking the squareroot and subtracting eq. A.26 from eq. A.25 gives

$$\sqrt{\frac{Q_c}{Q_l}} - \sqrt{\frac{Q_c}{Q_r}} = \frac{\cosh(\pi(w_x + X_0)/a_2) - \cosh(\pi(w_x - X_0)/a_2)}{\cosh(\pi X_0/a_2)}. \qquad (A.27)$$

Using $\cosh(a \pm b) = (\cosh a \cosh b \pm \sinh a \sinh b)$ one finds

$$\sqrt{\frac{Q_c}{Q_l}} - \sqrt{\frac{Q_c}{Q_r}} = \frac{2\sinh(\pi w_x/a_2)\sinh(\pi X_0/a_2)}{\cosh(\pi X_0/a_2)} \qquad (A.28)$$

$$= 2\sinh(\pi w_x/a_2)\tanh(\pi X_0/a_2) \qquad (A.29)$$

$$\Rightarrow \tanh(\pi X_0/a_2) = \frac{\sqrt{\frac{Q_c}{Q_l}} - \sqrt{\frac{Q_c}{Q_r}}}{2\sinh(\pi w_x/a_2)} \qquad (A.30)$$

and therefore

$$X_0 = \frac{a_2}{\pi}\operatorname{arctanh}\frac{\sqrt{\frac{Q_c}{Q_l}} - \sqrt{\frac{Q_c}{Q_r}}}{2\sinh(\pi w_x/a_2)}. \qquad (A.31)$$

a_2 is calculated like follows. Summing the squareroots of eq. A.25 and A.26 gives similar to eqn. A.27 and A.28

$$\sqrt{\frac{Q_c}{Q_l}} + \sqrt{\frac{Q_c}{Q_l}} = \frac{2\cosh(\pi w_x/a_2)\cosh(\pi X_0/a_2)}{\cosh(\pi X_0/a_2)} \qquad (A.32)$$

$$= 2\cosh(\pi w_x/a_2) \qquad (A.33)$$

$$\Rightarrow a_2 = \frac{\pi w_x}{\operatorname{arcosh}(\frac{1}{2}[\sqrt{\frac{Q_c}{Q_l}} + \sqrt{\frac{Q_c}{Q_r}}])}. \qquad (A.34)$$

Note that a_2 is proportional to the width. For the graph in fig. 2.2a we found $a_2 = 1.79\text{FWHM}$.

A.3 Algorithm for the Mathieson/Gatti formula for 3 strips

The parametrization of the Mathieson formula to calculate the impact position using 3 consecutive strips has not been found in the literature [1]. This is surprising as one would expect to have the smallest systematic deviations using a formula that suits best the real charge distribution. We therefore note its evaluation. As the width is fixed by the parameter K_3 (see eq. 2.5) there are only two unknown parameters. Nevertheless the relation is more complicated. First we repeat that Mathieson's charge distribution (eq.

[1] Fenker *et al.* [15] seem to use such a parametrization but do not give the formula in their paper.

2.1) can be easier written using $1-\tanh^2 = 1/\cosh^2$ and $\cosh^2 = 1+\sinh^2$

$$\frac{\rho(\lambda)}{q_a} = \frac{K_1}{1+(K_3+1)\sinh^2(K_2\lambda)} \,. \qquad (A.35)$$

q_a is the total charge, $\lambda = X/d$ and $K_{1,2,3}$ are geometry dependent constants as defined in chapter 2. Thus there is only *one* hyperbolic function in the equation which simplifies the following calculus.

The charge on the 3 strips is given by

$$Q_i = \frac{q_a K_1}{1+(K_3+1)\sinh^2(\frac{K_2}{d}X_i)} \,, \qquad (A.36)$$

with Q_i and X_i as above. One finds for the charges on the 3 strips

$$Q_l = \frac{q_a K_1}{1+(K_3+1)\sinh^2(-\frac{K_2}{d}(w_x+X_0))} \qquad (A.37)$$

$$Q_c = \frac{q_a K_1}{1+(K_3+1)\sinh^2(-\frac{K_2}{d}X_0)} \qquad (A.38)$$

$$Q_r = \frac{q_a K_1}{1+(K_3+1)\sinh^2(\frac{K_2}{d}(w_x-X_0))} \,. \qquad (A.39)$$

The second equation (A.38) is used again to express the total charge

$$q_a = \frac{Q_c}{K_1}(1+(K_3+1)\sinh^2(\frac{K_2}{d}X_0)) \,, \qquad (A.40)$$

with $\sinh(-x) = -\sinh(x)$. Using the theorems $\sinh(x\pm y) = \sinh x\cosh y \pm \cosh x\sinh y$ one gets from eqn. A.37 and A.39

$$\begin{aligned}\frac{q_a K_1}{Q_l} &= 1+(K_3+1)\,* \\ &\quad (\sinh\frac{K_2}{d}w_x\cosh\frac{K_2}{d}X_0 \\ &\quad + \cosh\frac{K_2}{d}w_x\sinh\frac{K_2}{d}X_0)^2 \qquad (A.41)\\ \frac{q_a K_1}{Q_r} &= 1+(K_3+1)\,* \\ &\quad (\sinh\frac{K_2}{d}w_x\cosh\frac{K_2}{d}X_0 \\ &\quad - \cosh\frac{K_2}{d}w_x\sinh\frac{K_2}{d}X_0)^2 \qquad (A.42)\end{aligned}$$

Inserting eq. A.40 in eqn. A.41 and A.42 yields

$$\begin{aligned}&\left(\frac{Q_c}{Q_l}-1\right)/(K_3+1)+\frac{Q_c}{Q_l}\sinh^2\frac{K_2}{d}X_0 \\ &\quad = (\sinh\frac{K_2}{d}w_x\cosh\frac{K_2}{d}X_0 \\ &\quad + \cosh\frac{K_2}{d}w_x\sinh\frac{K_2}{d}X_0)^2 \qquad (A.43)\\ &\left(\frac{Q_c}{Q_r}-1\right)/(K_3+1)+\frac{Q_c}{Q_r}\sinh^2\frac{K_2}{d}X_0 \\ &\quad = (\sinh\frac{K_2}{d}w_x\cosh\frac{K_2}{d}X_0 \\ &\quad - \cosh\frac{K_2}{d}w_x\sinh\frac{K_2}{d}X_0)^2 \,. \qquad (A.44)\end{aligned}$$

To keep the equations clear the following abbreviations are introduced for known terms:

$$\begin{aligned}a_1 &= \left(\frac{Q_c}{Q_l}-1\right)/(K_3+1) && (A.45)\\ a_2 &= \frac{Q_c}{Q_l} && (A.46)\\ a_3 &= K_2/d && (A.47)\\ a_4 &= \sinh\frac{K_2}{d}w_x && (A.48)\\ a_5 &= \cosh\frac{K_2}{d}w_x && (A.49)\\ b_1 &= \left(\frac{Q_c}{Q_l}-1\right)/(K_3+1) && (A.50)\\ b_2 &= \frac{Q_c}{Q_l} \,. && (A.51)\end{aligned}$$

Eqn. A.43 and A.44 become much simpler:

$$\begin{aligned}&a_1+a_2\sinh^2 a_3X_0 = \\ &\quad (a_4\cosh a_3X_0 + a_5\sinh a_3X_0)^2 \qquad (A.52)\\ &b_1+b_2\sinh^2 a_3X_0 = \\ &\quad (a_4\cosh a_3X_0 - a_5\sinh a_3X_0)^2 \,. \qquad (A.53)\end{aligned}$$

Calculating the right sides and adding eqn. A.52 and A.53 gives

$$\begin{aligned}&a_1+b_1+(a_2+b_2)\sinh^2 a_3X_0 = \\ &\quad 2(a_4^2\cosh^2 a_3X_0 + a_5^2\sinh^2 a_3X_0) \,. \qquad (A.54)\end{aligned}$$

With $\cosh^2 = \sinh^2+1$ one finds

$$\begin{aligned}&(a_2+b_2-2a_4^2-2a_5^2)\sinh^2 a_3X_0 = \\ &\quad 2a_4^2-a_1-b_1 \,. \qquad (A.55)\end{aligned}$$

$$\Rightarrow X_0 = \frac{d}{K_2}\operatorname{arcsinh}\sqrt{\frac{2a_4^2-a_1-b_1}{a_2+b_2-2(a_4^2+a_5^2)}} \,. \qquad (A.56)$$

A.4 Lorentzian algorithm for 3 strips

Attempts with a Lorentzian shaped function were made by [27, 28, 30]. The function is a rather poor approximation of the charge distribution (see fig. 2.2). Especially the tails of the function are much wider and therefore overestimate the induced charge on the side strips. Systematic deviations are consequently very large and the resolution poor. Nevertheless we show how the center of gravity is calculated from this function.

The Lorentzian or Breit-Wigner function describes the charge profile as follows

$$Q_i = \frac{a^2}{(X_i - X_0)^2 + (\Gamma/2)^2}\ , \tag{A.57}$$

with parameters as above except Γ being the FWHM. For the mean positions X_i of 3 consecutive strips we have

$$Q_l = \frac{a^2}{(w_x + X_0)^2 + (\Gamma/2)^2} \tag{A.58}$$

$$Q_c = \frac{a^2}{X_0^2 + (\Gamma/2)^2} \tag{A.59}$$

$$Q_r = \frac{a^2}{(w_x - X_0)^2 + (\Gamma/2)^2}\ . \tag{A.60}$$

Dividing eq. A.58 and A.60 by eq. A.59 eliminates a

$$\frac{Q_l}{Q_c} = \frac{X_0^2 + (\Gamma/2)^2}{(w_x + X_0)^2 + (\Gamma/2)^2} \tag{A.61}$$

$$\frac{Q_r}{Q_c} = \frac{X_0^2 + (\Gamma/2)^2}{(w_x - X_0)^2 + (\Gamma/2)^2}\ . \tag{A.62}$$

Solving both equations for $(\Gamma/2)^2$ gives

$$(\Gamma/2)^2 = \frac{Q_l(w_x + X_0)^2 - X_0^2 Q_c}{Q_c - Q_l} \tag{A.63}$$

$$(\Gamma/2)^2 = \frac{Q_r(w_x - X_0)^2 - X_0^2 Q_c}{Q_c - Q_r}\ . \tag{A.64}$$

Combining eqn. A.63 and A.64 yields after few steps

$$\frac{Q_l(w_x + 2X_0)}{Q_c - Q_l} = \frac{Q_r(w_x - 2X_0)}{Q_c - Q_r}\ . \tag{A.65}$$

After multiplication one finds for X_0

$$X_0 = \frac{w_x}{2}\frac{Q_r - Q_l}{Q_l + Q_r - \frac{2Q_lQ_r}{Q_c}}\ . \tag{A.66}$$

A.5 Determination of the spatial resolution from the residuals by 2 or 3 Gauss-fits

In the literature one finds usually that the resolution is determined from a single Gaussian fit to the residuals. But even for the simplest case (without double-hits or delta electrons) nonlinearities lead to a nonuniform resolution over the pad (see fig. 4.15). Therefore the residuals can not be well described by a simple Gaussian. Nevertheless one gets much better fit by combining 2 or 3 Gaussians. This is shown in the fig. A.1 for the single-hit results from the ratio algorithm (see section 4.3). The fit with two Gaussians has a 10 times better χ^2. A weighted mean is calculated for the resolution

$$\bar{\sigma} = \frac{\sum_i^{2,3} a_i\sigma_i^2}{\sum_i^{2,3} a_i\sigma_i}\ , \tag{A.67}$$

where a_i is the ith amplitude.

Though in fig. A.1 the difference for the 2 σ's is only 7% there are more important cases where contributions from very different σ's are added. The method will then become meaningfull. Note that the RMS calculated by PAW more than 10% larger than the mean σ from the fit. This is due to 0.2% of events outside the defined spectrum range. Nevertheless one sould also give the percentage of events which lies inside 3σ of the largest Gaussian to know with what efficiency the resolution was obtained.

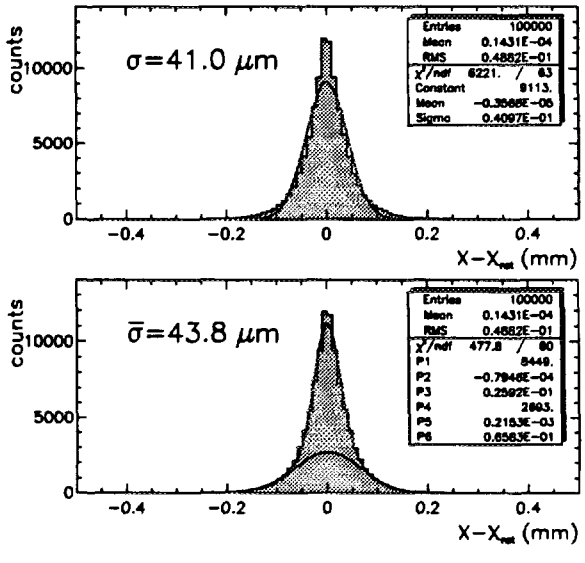

Figure A.1: *Resolution determination using 1 or 2 Gauss-fits.*

A.6 List of subroutines

Bibliography

[1] The ALICE collaboration,
Letter of Intent for A Large Ion Collider Experiment,
CERN/LHCC/93-16, LHCC/I 4, 1 March 1993.

[2] The ALICE collaboration,
Debye Screening in Heavy-Ion Collisions with the ALICE Detector,
CERN/LHCC/95-24.

[3] The ALICE collaboration,
Technical Proposal for A Large Ion Collider Experiment at the CERN LHC,
CERN/LHCC/95-71, LHCC/P3, 15 December 1995.

[4] H.R. Schmidt and J. Schukraft,
The physics of ultra-relativistic heavy-ion collisions,
J. Phys. G19(1993)1705-1795.

[5] T. Matsui and H. Satz,
Phys. Lett. B178 (1986)416.

[6] G. Chapark and F. Sauli,
High-Accuracy, Two-Dimensional Read-Out In Multiwire Proportional Chambers,
Nucl. Inst. and Meth. 113 (1973) 381-385.

[7] N. Khovansky, V. Malyshev, V. Tokmenin, Yu. Sedykh, A. Korytov, L.S. Osborne, G.D. Ross, R. Verdier, Yu. Bonushkin, G. Mitselmakher,
Spatial resolution of profile-based detectors with external pick-up strips,
Nucl. Inst. and Meth. A 351 (1994) 317-329.

[8] K. Lau, B. Mayes, J. Pyrlik,
Test results of a high precision cathode strip chamber based on plastic streamer tubes,
Nucl. Inst. and Meth. A 354 (1995) 376-388.

[9] E. Gatti, A. Longoni, H. Okuno and P. Semenza,
Optimum Geometry For Strip Cathodes Or Grids in MWPC For Avalanche Localisation Along The Anode Wires,
Nucl. Inst. and Meth. 163 (1979) 83-92.

[10] E. Mathieson and J.S. Gordon,
Cathode Charge Distributions In Multiwire Chambers: 2. Approximate and empirical formulae,
Nucl. Inst. and Meth. 227 (1984) 277-282.

[11] E. Mathieson,
Cathode Charge Distributions In Multiwire Chambers: 4. Empirical formula for small anode-cathode separation,
Nucl. Inst. and Meth. A 270 (1988) 602-603.

[12] J.S. Gordon And E. Mathieson,
Cathode Charge Distributions In Multiwire Chambers: 1. Measurement and theory,
Nucl. Inst. and Meth. 227 (1984) 267-276.

[13] F. Piuz, R. Roosen and J. Timmermans,
Evaluation Of Systematic Errors In The Avalanche Localization Along The Wire With Cathode Strips Read-Out MWPC,
Nucl. Inst. and Meth. A 196 (1982) 451-462.

[14] B. Yu,
Gas Proportional Detectors With Interpolating Cathode Pad Readout For High Track Multiplicities,
Ph. D. Thesis, Brookhaven National Laboratory, 1991.

[15] H. Fenker, K. Morgan, R. Shypit, J. Thomas, C.R. Bower, J. Musser, M. Brooks, D. Lee, R. Martin, G. Mills, J. Romero, S. Alam, B. Nematti, J.J. O'Neill, H. Severini, C. Baltay, B. Brakat, W. Emmet, J. Sinnott, E. Wolin, G. Smith, B. Yu,
Resolution measurement of an interpolating pad chamber in the 9 GeV/c π^- beam At BNL,
Nucl. Inst. and Meth. A 346 (1994) 75-94.

[16] H. Fenker, J. Thomas, M. Brooks, D. Lee, and G. Mills,
Precision Interpolating Pad Chambers,

Proceedings of the 1995 Vienna Wire Chamber Conference,
Nucl. Inst. and Meth. A 367 (1995) 285-289.

[17] G. Chapark, G. Melchart, G. Petersen and F. Sauli,
High-Accuracy Localisation Of Minimum Ionizing Particles Using The Cathode-Induced Charge Centre-Of-Gravity Read-Out,
Nucl. Inst. and Meth. 167 (1979) 455-464.

[18] L.S. Barabash *et al.*,
A Study Of The Detection Accuracy Of Proportional Chambers With Cathode Read-Out,
Nucl. Inst. and Meth. A 236 (1985) 271-273.

[19] A.L.S. Angelis, H. Beker, J.C. Berset, G. Ti Tore, C.W. Fabjan, U. Goerlach, C. Leroy, M. Price, V. Radeka, B. Sellden, V. Tcherniatine and W.J. Willis,
Test Results With A Novel High-Resolution Wire Chamber With Interpolative Pad Readout,
Nucl. Inst. and Meth. A 283 (1989) 762-766.

[20] R. Debbe, J. Fischer, D. Lissauer, T. Ludlam, D. Makowiecki, V. Radeka, S. Rescia, G.C. Smith, D. Stephani and B. Yu,
A MWPC With Highly Segmented Cathode Pad Readout,
Nucl. Inst. and Meth. A 283 (1989) 772-777.

[21] R. Debbe, J. Fischer, D. Lissauer, T. Ludlam, D. Makowiecki, E. O'Brien, V. Radeka, S. Rescia, L. Rogers, G.C. Smith, D. Stephani, B. Yu, S.V. Greene, T.K. Hemmick, J.T. Mitchell, B. Shivakumar,
A Study Of Wire Chambers With Highly Segmented Cathode Pad Readout For High Multiplicity Charged Particle Detection,
IEEE Trans. Nucl. Sci., NS-37 (1990) 88-94.

[22] H. van der Graaf, J. Buskens, G. Faber, A. König, P. Rewiesma and T. Wijnen,
The honeycomb strip chamber: the application in LHC/SSC experiments and the test results of a prototype,
Nucl. Inst. and Meth. A 307 (1991) 220-230.

[23] M. Benayoun, M. Crassson, A. Diaczek, P. Leruste, M. Pairat, M. Sené, R. Sené, S. Szafran, A. Volte,
Impact reconstruction in pad chambers, Part II: Test with pad chamber data,
Nucl. Inst. and Meth. A 345 (1994) 72-89.

[24] G. Bencze *et al.*,
Position and timing resolution of interpolating cathode strip chambers in a test beam,
Nucl. Inst. and Meth. A 357 (1995) 40-54.

[25] J. Guilliot, A. Willis,
private communication, test results at IPN Orsay (1995).

[26] G. Fischer and J. Plch,
The High Voltage Read-Out For Multiwire Proportional Chambers,
Nucl. Inst. and Meth. 100 (1972) 515-523.

[27] D.M. Lee, S.E. Sobottka and H.A. Thiessen,
A Bifilar Helical Multiwire Proportional Chamber For Position Sensitive Detection Of Minimum Ionizing Particles,
Nucl. Inst. and Meth. A 104 (1972) 179-188.

[28] I. Endo, T. Kawamoto, Y. Mizuno, T. Ohsugi, T. Taniguchi and T. Takeshita,
Systematic Shifts Of Evaluated Charge Centroid For The Cathode Read-Out Multiwire Proportinal Chamber,
Nucl. Inst. and Meth. 188 (1981) 51-58.

[29] M. Benayoun, P. Leruste, J.L. Narjoux, M. Sené, R. Sené, A. Volte,
Impact reconstruction in pad chambers, Part I: Simulation studies,
Nucl. Inst. and Meth. A 342 (1994) 483-494.

[30] K. Lau, J. Pyrlik,
Optimization of centroid-finding algoritms for cathode strip chambers,
Nucl. Inst. and Meth. A 366 (1995) 298-309.

[31] B. Yu, G.C. Smith, V. Radeka and E. Mathieson,
Investigation Of Chevron Cathode Pads For Position Encoding In Very High Rate, Gas Proportional Chambers,
IEEE Trans. Nucl. Sci., NS-38 (1991) 454-460.

[32] B. Yu, V. Radeka, G.C. Smith and E. O'Brien,
Interpolating cathode pad readout in gas proportional detectors for high multiplicity particle tracks,
Nucl. Inst. and Meth. A 323 (1992) 413-418.

[33] H.-Å. Gustafsson (Lund University), private communication.

[34] A. Rybicki,
The PAD Response Function Of The ALICE TPC, ALICE/95-29, Internal Note/TPC, 28 September 1995.

[35] J. Chiba, H. Iwasaki, T. Kageyama, S. Kuribayashi, K. Nakamura, T. Sumiyoshi, and T. Takeda,
Study Of Position Resolution For Cathode Readout MWPC With Measurement Of Induced Charge Distribution,
Nucl. Inst. and Meth. A 206 (1983) 451-463.

[36] E. Beuville, K. Borer, E. Chesi, E.H.M. Heijne, P. Jarron, B. Lisowski and S. Singh,
Amplex, A Low-Noise, Low-Power Analog CMOS Signal Processor For Multielement Silicon Particle Detectors,
Nucl. Inst. and Meth. A 288 (1990) 157-167.

[37] V. Armijo, L. Atencio, M.L. Brooks, D.M. Lee, J.B. McClelland, C.L. Morris, P.L. McGaughey, M. Rawool-Sullivan, W.E. Sondheim,
LANL Report on the R&D Program for Cathode Strip Readout Chambers for the PHENIX Muon Tracking System,
PHENIX Note 125 (PN125), 1995.

[38] A. Breskin, G. Chapark, C. Demierre, S. Majewski, A. Policarpo, F. Sauli and J.C. Santiard,
High-Accuracy, Bidimensional Read-Out Of Proportional Chambers With Short Resolution Times,
Nucl. Inst. and Meth. 143 (1977) 29-39.

[39] M. Brooks,
Simulation of PHENIX Muon CSC's,
PHENIX report, 29 february 1996.

[40] B. Yu, G.C. Smith and V. Radeka,
Developments in interpolationg cathode structures for high precision gas proportional detctors,
in preparation.

[41] H. Fenker, private communication.

[42] V. Gratchev, M. Mohammadi-Baarmand, V. Polychronakos, J. Shank, V. Tcherniatine, A. Vaniachine,
Double Track Resolution of Cathode Strip Chambers,
submitted to Nucl. Inst. and Meth. A.

[43] ALICE Di-Muon colaboration meeting, Orsay, February 1996.

[44] G. Bauer, A. Bettini, G. Busetto, S. Centro, M. De Giorgi, R.Frühwirth, T. Markiewicz, A. Meneguzzo, M. Mohammadi, D. Pascoli, A. Placci, P. Rossi, K. Sumorok, L. Zanello and P. Zotto,
Resolution Of Plastic Streamer Tubes With Analog Readout,
Nucl. Inst. and Meth. A 260 (1987) 101-113.